Demonstration of a Basis for Tall Wind Turbine Design, EUDP Project Final Report

Natarajan, Anand; Dimitrov, Nikolay Krasimirov; Madsen, Peter Hauge; Berg, Jacob; Kelly, Mark C.; Larsen, Gunner Chr.; Mann, Jakob; Verelst, David Robert; Dalsgaard Sørensen, John; Toft, Henrik

Total number of authors:
18

Publication date:
2016

Document Version
Publisher's PDF, also known as Version of record

Demonstration of a Basis for Tall Wind Turbine Design, EUDP Project Final Report

DTU Vindenergi
E Rapport 2016

Anand Natarajan, Nikolay Dimitrov, Peter Hauge Madsen, Jacob Berg, Mark Kelly, Gunner Larsen, Jakob Mann, David Verelst, **Technical University of Denmark**

John D. Sørensen, Henrik Toft, **Ålborg University**
Imad Abdallah, **Mita Teknik**
Niels-Jacob Tarp Johansen, Thomas Krogh, **DONG Energy**
Jesper Stærdahl, **Siemens Wind Power**
Christer Eriksson, Erik Jørgensen, **DNV – GL**
Frank Klintø, **Suzlon Energy**
Leo Thesbjerg, **Vestas Wind Systems**

DTU Wind Energy E-0108

Jan 2016

DTU Vindenergi
Institut for Vindenergi

Authors: Anand Natarajan Nikolay Dimitrov, Peter Hauge Madsen, Jacob Berg, Mark Kelly, Gunner Larsen, Jakob Mann, David Verelst, John D. Sørensen, Henrik Toft, Imad Abdallah, Niels-Jacob Tarp Johansen, Thomas Krogh, Jesper Stærdahl, Christer Eriksson, Erik Jørgensen, Frank Klintø, Leo Thesbjerg

Title: Demonstration of a Basis for Tall Wind Turbine Design

Institute: DTU Wind Energy

Resume:

Wind turbine design using calibrated wind models have been proposed to be used in conjunction with load cases which lead to reduced uncertainties in the design of wind turbines with hub heights above 60m. These recommended wind profiles have been made for shear, wind directional change and turbulence. The wind turbulence models used in the loads simulations have been calibrated so that their model parameters reflect the atmospheric stability conditions and the quantile of turbulence intensity considered. Consequently large multi megawatt turbines being designed today can benefit from these more advanced wind inflow models. A revision of the IEC 61400-1 standard is being developed and has incorporated some of the recommendations made from this project.

This project demonstrated the impact of wind models by simulating wind turbine loads based on high frequency wind measurements taken between 100m and 200m altitude performed at Høvsøre in Denmark. The project also demonstrated the impact of the new wind models on load cases and the certification envelope of turbines. Further the project provided a detailed assessment of safety factors for IEC 61400-1 load cases using reliability-based procedures incorporating the new models and this has been made as an Annex to the new standard that is due to be issued.

DTU Wind Energy E-0108
Jan 2016

Contract number:
EUDP 11-II 64011 -0352

Project number:
64011 -0352

Sponsorship:
EUDP

ISBN : 978-87-93278-65-3

Pages: 101
Tables: 20
References: 40

Danmarks Tekniske Universitet
DTU Vindenergi
Nils Koppels Allé
Bygning 403
2800 Kgs. Lyngby

www.vindenergi.dtu.dk

Preface

This report details all the findings of the EUDP project Demonstration of a Basis for Tall Wind Turbine Design and is the final report of project as submitted to EUDP.

Roskilde, Apr 2015

Anand Natarajan

Table of Contents

Abstract

The project's key objective was to demonstrate the impact of wind inflow in the range between 100m and 200m altitude on wind turbine loads through measurement of relevant atmospheric characteristics. This was achieved using high frequency sonic anemometer measurements at several heights in the sites located at Høvsøre in Denmark and Cabauw in Netherlands, as well as wind farm sites in North America with Suzlon wind turbines. The project demonstrated the impact of the new wind models on load cases and design loads on the DTU 10 MW conceptual wind turbine and the models developed were also tested on existing commercial turbines. Based on wind measurements at these sites, complete analysis and recommendations to the IEC 61400-1[1] and -3 [2] standards was made for 1) wind shear, 2) extreme turbulence, 3) effect of de-trending turbulence, 4) Gaussian versus non Gaussian turbulence and 5) Partial safety factors. The project developed more detailed wind field descriptions based on which the uncertainty in load simulations on tall wind turbines is reduced and the optimal definition of wind velocity definitions achievable using current measurement technology was also addressed. Partial load safety factors for the loads and materials were better delineated and thereby were able to be linked to the degree of uncertainty in wind models, blade aerodynamics and turbine controls all of which interact simultaneous to produce the design loads. This analysis led to a better assessment of the reliability of the structure under different operational conditions.

1. Introduction

Large wind turbines are highly flexible and its rotor spans a large region of the atmosphere greater than 200m in height, which implies that the wind models input to loads simulations require higher resolution based on high frequency site measurements. Current load cases, as specified by the IEC 61400-1 [1] standard used to simulate wind turbine component loads, were developed using short term wind inflow measurements on wind farms at wind turbine hub heights of 60m and below. These entirely coherent wind profiles for operational gust, shear, wind directional change are simplistic and were made more than a decade ago. The wind turbulence model used in the loads simulations also does not account for atmospheric stability effects and other phenomena commonly encountered at higher altitudes. Consequently all large multi megawatt turbines being designed today are subject to large uncertainties due to simplistic wind inflow models. A revision of the IEC 61400-1[1] standard is being developed. The key objectives of the present project were therefore to:

1) Measure the wind velocity at suitable sites in Europe at different altitudes using high frequency sonic anemometers
2) Develop wind models applicable for loads simulations
3) Propose recommendations to the IEC standards committee based on new wind models validated by measurements.

In order to perform the aero-elastic simulations needed for analyses of loads on 'tall' wind turbines, whose rotors typically reside above the atmospheric surface layer, it is necessary to have representative datasets of relevant meteorological fields. More specifically, we need wind measurements at heights spanning the rotor of tall turbines, including both longer-term (multi-year) data as well as turbulence (e.g. 10 Hz) data at numerous sites—to optimally characterize the atmospheric forcing and conditions, which drive both fatigue and extreme loads. Further, since atmospheric stability (buoyancy) and the depth of boundary-layer affect tall turbine loads as well as power production, it is optimal to also have measures of these in addition to the wind measurements.

The characterization of the atmospheric forcing on tall turbines involves finding representative values of turbulence intensity, wind shear, and wind veer around hub height, from rotor-top to rotor-bottom; expected tall turbine hub heights span from ~100-200 m, with rotor sizes on the order of 100 m.

2. Atmospheric Measurements

2.1 Tall-wind observations

Analytical and boundary-layer meteorology theory for wind, turbulence, and stability has been validated only within the atmospheric surface layer (up to ~20 m for winter/night and ~100 m in summer). Thus to investigate the relevant wind parameters for tall turbines, and develop a formulation for characteristic atmospheric forcing above the surface layer, it is necessary to gather as many wind observations as possible in the 'tall wind' regime, i.e. above 100 m.

2.1.1 Data sets

The project included a number of industrial partners in wind energy, among them DNV (Den Norske Veritas, now part of GL-DNV), Vestas, Siemens, Suzlon, and DONG Energy; they offered to share relevant wind data for the project, and thus a request for wind data meeting certain criteria was issued said participants in the project. The criteria for wind data was relatively simple, requiring: one pair of wind measurements (each including both speed and direction) at two different heights, where the upper height was to be 100 m above the surface or higher (preferably above 120 m); the data was to be recorded over at least one year, without significant gaps; and a description (e.g. map) for the observation site. The data request asked for (but did not explicitly require) high-frequency turbulence data, which was requested to be in the 'tall' regime and preferably from sonic anemometers; there was also a request for stability data to be added, where possible. These requirements were to ensure that both shear and veer could be measured over heights representative of tall wind turbines, because the behavior and statistics of the wind above the surface layer tends to be different than within the ASL. Emphasis was also added later to obtain turbulence data at different sites. The length requirement (i.e. needing an integer number of years) eliminates seasonal effects.

Unfortunately very little useful data was shared by the partners, due to a relative lack of sufficiently tall observation masts as well as a scarcity of reliable LIDAR data extending beyond one year. However, Suzlon offered several data sets, one of which was of suitable duration and with one height above 100 m. Suzlon additionally offered a 1-year SODAR dataset from a Swedish site, but due to SODAR's stability-dependent impact on sampling at increasing heights as well as effects of the local forest/terrain, this dataset was not sufficiently gap-free nor reliable. Dong Energy supplied two LIDAR datasets as well (Horns Rev and SIRI), both of which extended well above the surface layer but which unfortunately did not contain one full year of reliable data (due e.g. to one of them being moved, without recalibration).

Also, a number of suitable 'tall' wind datasets had previously been identified and preliminarily analyzed by Kelly *et al*. and DTU [3]; these include data from the National Turbine Test Center at Høvsøre on the western Danish coast, Cabauw in the Netherlands, and the forested Østerild site in northern Denmark. These three datasets, along with Suzlon's "good" dataset which we label '*MR*', comprise the bulk of our wind data which was analyzed; Table 1 summarizes the datasets.

Table 2.1. Sites used, with upper, mid-rotor, and lower heights for analysis; wind direction ranges; terrain types; and instrumentation.

Site	z_{upper} (m)	z_{mid} (m)	z_{lower} (m)	Dir. range	terrain type	Obs. type	Series length (y)
Cabauw	200	140	80	120–240°	farmland	sonic	2
Høvsøre	160	100	60	60–120°	farmland	sonic	6
Østerild	200/140	140/80	80/45	all	forest-mixed	LIDAR	1
'MR'	136	80	40	all	mixed + trees	cup	1

The Cabauw data was limited to the well-studied less-disturbed sectors [4], such that representative analysis could be done. Analogously, the Høvsøre data was limited to the eastern (land) sectors, avoiding the effects of the coastline and large dune to the west. Several LIDARs exist at the Østerild site, but only one gave at least 1 year of data, while not suffering from significant distortion effects induced by inhomogeneity of the surrounding forest and terrain. Due to the availability at many heights via LIDAR, Østerild has been split into two cases, one "low" and one "high", to highlight differences between the statistics at different heights; this is reflected in Table 1. The Østerild site is located in forest, with treetops less than 20m above ground, and the lowest LIDAR observation level (45m) is chosen to be above the subsequent roughness sub-layer and above the effects of tree-induced flow-distortion for valid LIDAR use; the terrain beyond several kilometers upwind also includes mixed grassland/agricultural and scattered forest. The site 'MR' has similar characteristics, including forest with clearings for several km surrounding the mast, and mixed forest and farm/grassland farther away; both Østerild and 'MR' sites have winds prevailing from the west, though data were not filtered for direction. All the sites vary in character, but are essentially in flat terrain.

While all 4 sites (5 cases) in Table 1 provided data (10-minute averages) for shear and veer calculations, only the anemometer measurements at Cabauw, Høvsøre, and 'MR' provided turbulence measurements for the project, since LIDAR cannot (yet) produce reliable turbulence statistics (Sathe & Mann); thus there were no turbulence measurements from Østerild.

2.1.2 Atmospheric quantities of interest; observed statistics

The primary atmospheric quantities which are most directly connected to turbine loads are turbulence intensity, wind shear (i.e. change in wind speed with height), and wind veer (change in wind direction with height). Atmospheric stability can affect these quantities, via both heating/cooling of the ground as well as the increase in temperature ("inversion") found at the top of the atmospheric boundary layer (which can be as shallow as ~100 m), but it does not affect the turbine directly.

2.1.2.1 Shear

The shear was measured over multiple heights, at the four sites used, as shown in Table 2.1. Specifically, the *shear exponent*, defined by $\alpha = \left(dU/dz\right)\Big/\left(U/z\right)$ and used in the IEC standard 61400-1, was calculated by $dU/dz = \left(U_{upper} - U_{lower}\right)\Big/\left(z_{upper} - z_{lower}\right)$ via the wind speed at upper and lower heights, with speed *U* also taken at the center

height; this corresponded to a turbine rotor diameter $(z_{upper} - z_{lower})$ of 95-120 m the sites. Note that the effective hub height varied from site to site, as indicated in the table, with the rotor size ranging from 85-110% of hub height; further, the forested cases (Østerild, MR) have rotor size to hub-height ratios ranging from ~95-125%.

Over the wind speed range 4-25 m/s (i.e. those encountered by an operating turbine), the distribution of shear exponent is shown in Figure 2.1 for all sites/cases.

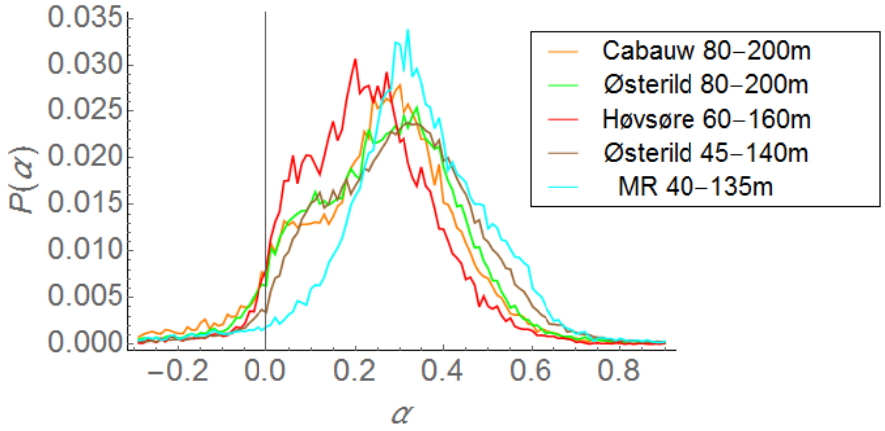

Figure 2.1: Distribution of shear exponent for all cases, for winds between 4-25 m/s.

The shear distributions overlap quite substantially and do not appear markedly different, though the lower effective roughness at Høvsøre is indicated by the peak at smaller α for that site.

However, one expects a wind-speed dependence in the probability of finding a given shear exponent; the joint-distribution $P(\alpha,U)$ is nontrivial. This is indeed the case, as shown in Figure 2.2. For higher wind speed U, a narrowing of the conditional distribution $P(\alpha|U)$ around progressively smaller α-peaks is seen; this is consistent with stability having less influence in high winds, and more turbulent transport effect over forests. One can also see more differences between the sites, with the peak of $P(\alpha,U)$ occurring at lower U for lower z/z_0 (where z_0 is the roughness).

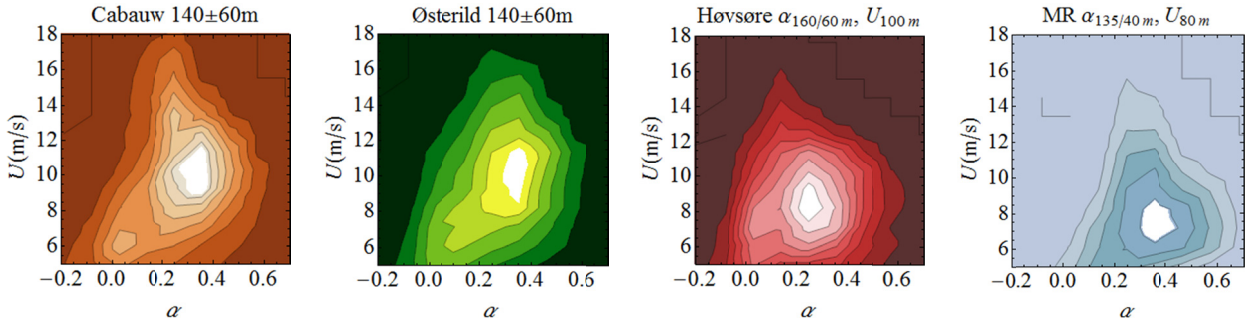

Figure 2.2: Joint distributions of wind speed $U(z_{mid})$ and shear exponent α for Cabauw (orange, z_{mid}=140m), Østerild-high (green, z_{mid}=140m), Høvsøre (red, z_{mid}=100m), and 'MR' (blue, z_{mid}=80m). Heights used per site are listed in Table 1.

The shear exponent distribution was shown to be analytically mapable to the distribution of stabilities [3], but only within the surface layer; since there were also no observations of

ABL-top (inversion) temperature profiles, the stability was not considered further in this project. The shear (affected by stability) dictates the mean vertical variation of loading across a turbine rotor.

A significant finding in the project was the analytical and observational confirmation that the width of the conditional shear exponent distribution $P(\alpha|U)$ is inversely proportional to wind speed, as shown in Figure 2.3.

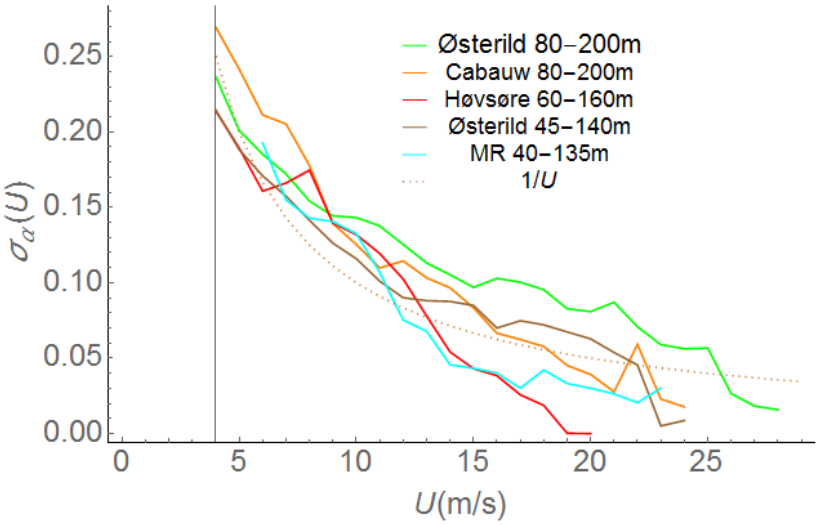

Figure 2.3: RMS variation of shear exponent with wind speed ('width' of shear exponent distribution).

The behavior noted in and above Figure 2.3, along with analytical derivations for mean shear including the effect of stability and turbulence, led to a probabilistic wind shear model, which is elucidated in Section 3 of this report.

2.1.2.2 Veer

The veer is defined as the change in wind direction with height, calculated here in an analogous way as the shear: from rotor top to rotor bottom. Following from classic Ekman-layer theory, the veer depends upon the height above ground, the distance over which the veer is calculated (e.g. the turbine rotor size), the turbulence diffusivity (thus intensity), and (to a lesser extent) the atmospheric boundary layer depth. However, the assumptions involved in Ekman theory are not valid around hub height under most conditions in the atmosphere, even over relatively homogeneous land; in reality the amount of turbulent vertical mixing varies with height from the surface, and this is also related to the surface roughness. Most simply, the veer depends upon the shear exponent. This can be seen in Figure 2.4, which displays the measured joint distribution of veer ($\Delta\phi$) and shear exponent (α) for the five cases analyzed. An analytical relation for the mean relation between shear and veer was developed (shown by the blue lines in the figure), given in the next subsection.

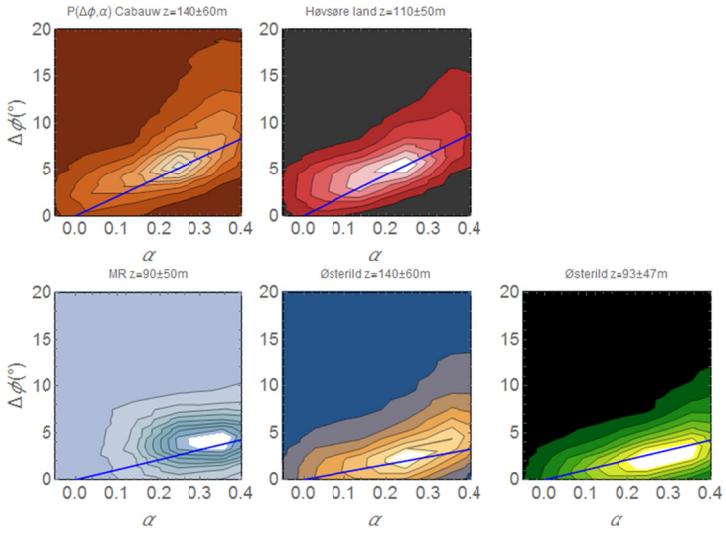

Figure 2.4: Joint distribution of shear exponent (α) and wind veer ($\Delta\phi$) for Cabauw (orange), Høvsøre (red), 'MR' (blue), Østerild-high (tan/blue), and Østerild-low (green). Blue lines are reduced mean veer model.

Joint shear-veer histograms were produced and served as input to the HAWC2 aeroelastic tool, for loads calculation and verification of using modeled shear distribution with a simplified form relating shear and veer.

2.1.2.3 Turbulence intensity

In the measurements work package (WP-1), turbulence intensity was investigated predominantly with regards to shear. However, analytical derivations including the effect of stability and turbulence led to relation between turbulence intensity and mean shear exponent, shown by the blue lines in Figure 2.5.

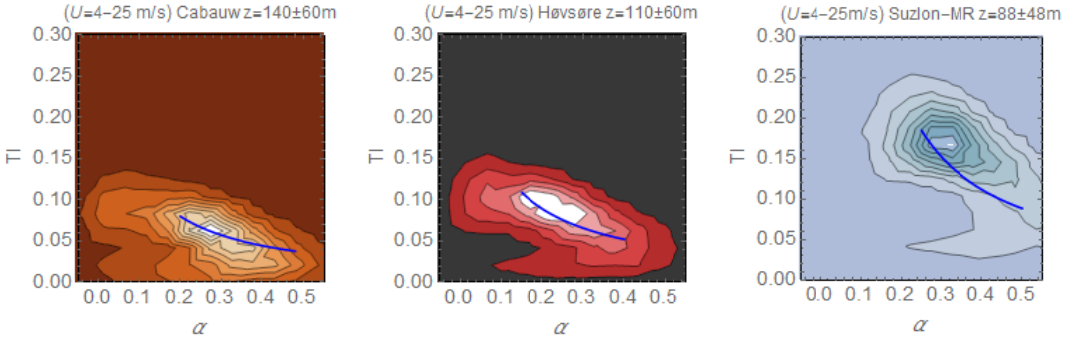

Figure 2.5: Joint distribution of turbulence intensity and shear exponent, with analytical engineering model overlaid as blue line. Left (orange) is Cabauw; center (red) is Høvsøre; right (blue) is site 'MR'.

The joint distributions of turbulence intensity and veer were also investigated but are not shown, since they do not provide significant additional information beyond the shear-veer and turbulence intensity-shear joint distributions.

2.1.3 RANS 'aggregation'

Because there are not (yet) a substantial number of sufficient measurements available above the atmospheric surface layer (as seen in this project)—i.e. typical measurements are still at or below 100m due to cost, and LIDAR is not typically running for more than one year at a site—it becomes reasonable to investigate the use of models as a proxy for measurements. While mesoscale models can reasonably replicate wind distributions at some sites, they generally do not produce realistic shear statistics. Thus microscale models become attractive; because large-eddy simulation is very resource intensive, then Reynolds-averaged Navier-Stokes (RANS) solvers are more reasonable to use. Here we have investigated the use of the unsteady RANS model ScaDis to replicate 'tall wind' statistics for a simple site. In particular, ScaDis was driven given a limited number of forcings (geostrophic winds) and radiation situations (zero, half, and full cloud cover) over a corresponding diurnal cycle, for an ideal flat site having characteristics similar to Cabauw. The results were inspected for a 100 m rotor size at hub heights of 100, 150, and 200 m, respectively; when convolved, using realistic representative probabilities of occurrence for each of the situations (forcing and radiation), then convergence towards a distribution similar to measurements can be seen. This can be seen in Figure 2.6, which displays the resulting distribution of shear exponent.

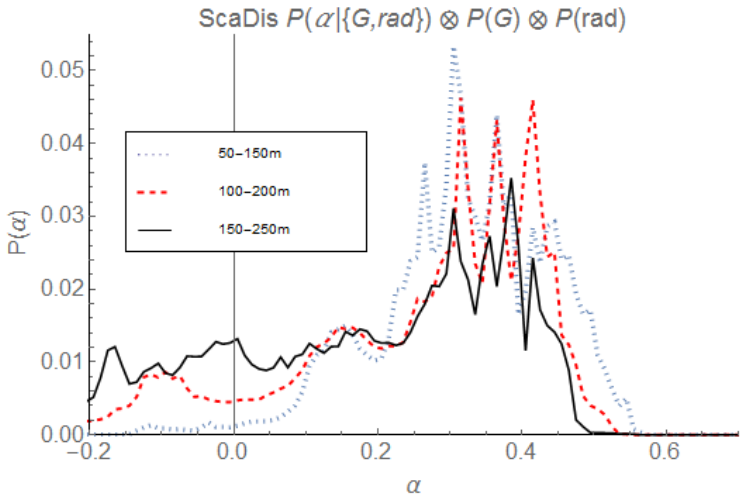

Figure 2.6: Shear-exponent distribution for rotor at 3 different heights, from convolution of representative RANS simulations over a range of geostrophic winds (forcings, G) and sky conditions (radiation, 'rad').

The aggregated ScaDis results displayed in Figure 2.6 show results approaching the Cabauw observations, in the sense that a peak in simulated $P(\alpha)$ can be seen around α~0.3; however there are noticeable peaks at higher α due to the relatively small number of simulations stability situations, and ABL depths represented. The results are otherwise encouraging, given the main peak and further the ability to produce cases with negative shear—unlike theoretical models—with increasing frequency for taller turbines, as observed, due to the rotor's extension beyond the ABL. More investigation needs to be done on such use, however, including driving uRANS with mesoscale models; such is beyond the scope of the present project.

2.2 Representative atmospheric formulations

Based on boundary-layer meteorology and atmospheric turbulence theory, the observed distributions of shear, stability, turbulence (intensity), and veer led to a number of simplifying formulations. We attempted to create forms which are universally representative, in the sense that they can be applied at many places, with a minimum of site-specific influence or parameters.

2.2.1 Most likely Shear and Turbulence Intensity

As indicated by the blue lines superposed in Figure 2.5, a reduced 'engineering' formulation compatible with the IEC 61400-1 standard was developed, relating the most likely values of turbulence intensity and shear exponent. This was done via extension of classic Monin-Obukhov theory [3,4] beyond the surface layer, giving the semi-empirical generalized form

$$I_U = \frac{I_{U0}}{1 + c_\alpha(\alpha - \alpha_0)} \tag{1}$$

where $I_{U0} \equiv a_u \kappa \alpha_0$ is the reference turbulence intensity, a_u is a constant typically taken to be 2.5 and the constant c_α is empirically found to be roughly 4. Dimitrov *et al.* [5] extended this and further developed a relation for more direct implementation in the IEC 61400-1, e.g. accounting for the top quantile of turbulence intensity.

2.2.2 Shear Variability

Through analytical derivation, confirmed by observations as shown in Figure 2.3 above, another useful relation was found involving the shear exponent. Namely, the variation of shear as a function of wind speed is approximately

$$\sigma_\alpha \propto U^{-1}. \tag{2}$$

2.2.3 2.2.3 Most likely/mean shear and veer

A series of derivations to relate veer and sheer were also accomplished, which will be a subject of a forthcoming article. One formulation includes extension of Ekman theory to include the basic variation of turbulent stress with height as observed in the atmospheric surface layer. This formulation gives the most likely veer for a given shear exponent, approximately relating the mean shear and veer (over all wind speeds), as shown in Figure 2.4. Such a formulation can be simplified to

$$\Delta\varphi = \varphi(z) - \varphi(z_{hub}) \approx a_\varphi e^{-\sqrt{z_{hub}/h_{ME}}} \frac{(z - z_{hub})}{\sqrt{z_{hub} h_{ME}}} \left[1 - \frac{(z - z_{hub})}{2\sqrt{z_{hub} h_{ME}}} - \frac{(z - z_{hub})}{4 z_{hub}} \right], \tag{3}$$

where a_φ is a constant of order 1 and h_{ME} is the modified-Ekman ABL depth, as are a number of alternate formulations which include relation to shear, turbulence intensity and surface properties.

3. Prioritized wind Shear And Turbulence models that drive design loads

Aeroelastic simulations use a random turbulence field based on several parametric descriptors of the wind. In this project, several of the most important parameters were studied. This included the wind shear exponent, turbulence intensity under normal and extreme turbulence conditions, and turbulence spectral model parameters.

3.1 Wind shear model

The mast measurement data available for the project from flat terrain showed that the wind shear exponent is typically less than the value recommended by the IEC61400-1 standard ($\alpha = 0.2$), but it is characterized with a large scatter and changing behavior at different wind speeds.

A probabilistic model for wind shear conditional on turbulence was derived and defined based on theoretical considerations and by stochastic fit to measurements from Høvsøre and Cabauw (Figure 3.1). The work has been published [3], [5] with details describing the theoretical basis, and compares the proposed wind shear model prediction with the obtained measurements, with studies on the effect of using the model for design load calculations. The main conclusions regarding wind shear are:

- The wind shear exponent has no visible effect on loads on the support structure of tall wind turbines, and relatively small effect on extreme and fatigue loads acting on the hub and blades (Figure 3.2). Under low-turbulence conditions such as IEC turbulence class C the effect of wind shear becomes significant and it is recommended to use the proposed probabilistic wind shear model. For high-turbulence conditions, the turbulence dominates the loads and the effect of wind shear becomes insignificant.
- Under all conditions the wind shear has a strong effect on the maximum blade deflection towards the tower (Figure 3.3). The current practice of using a constant exponent $\alpha = 0.2$ results in non-conservative estimations of the maximum deflection towards the tower.

A proposal for updating the Normal Wind Shear (NWS) model in the IEC61400-1 standard was submitted (the proposed model shown on Figure 3.4), and the new edition of the standard will recommend using the model for low-turbulence turbine classes.

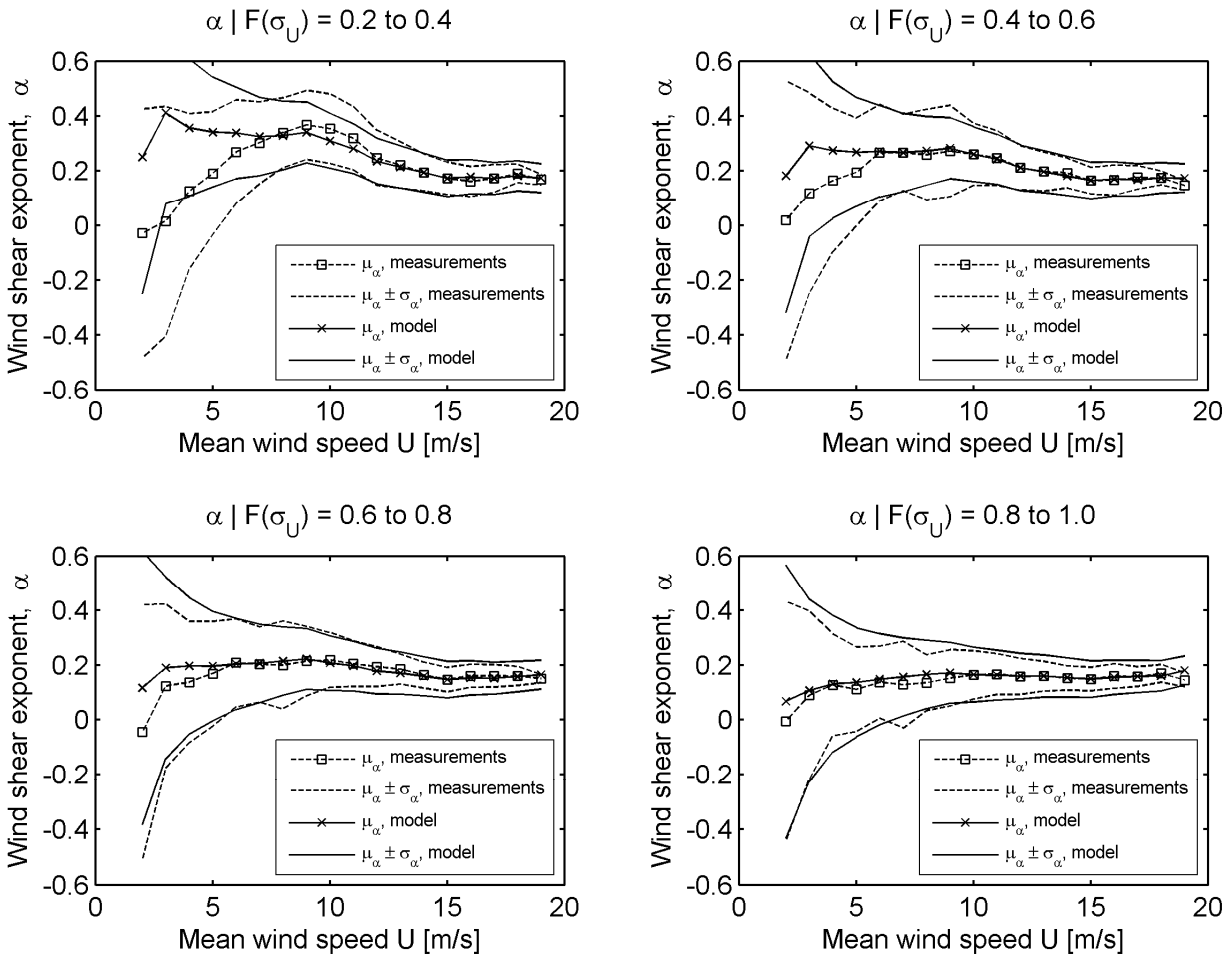

Figure 3.1 Wind shear measurements at Høvsøre compared to empirical model, conditional on turbulence intensity.

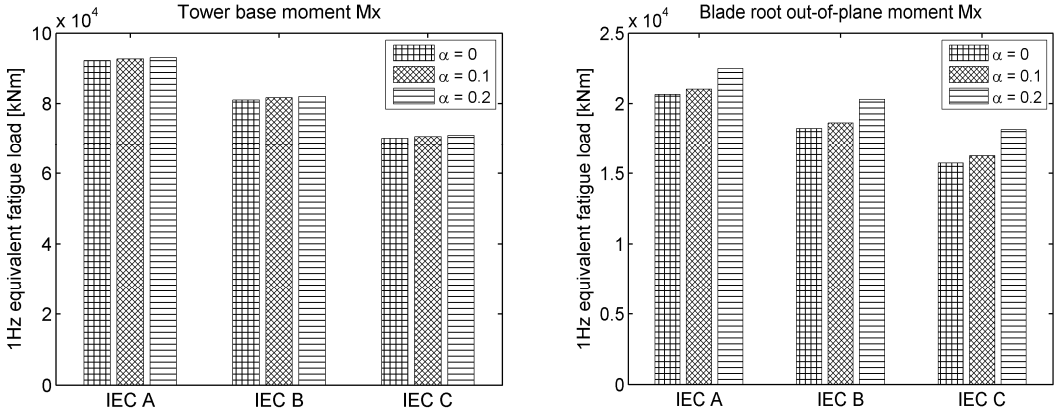

Figure 3.2 Influence of turbulence and wind shear on tower base equivalent fatigue moment and blade root out of plane moment

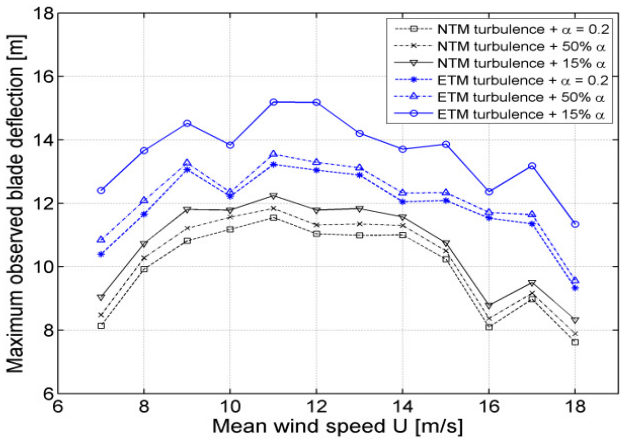

Figure 3.3 Effect of wind shear on the 99th percentile of extreme blade deflection during blade-tower passage events.

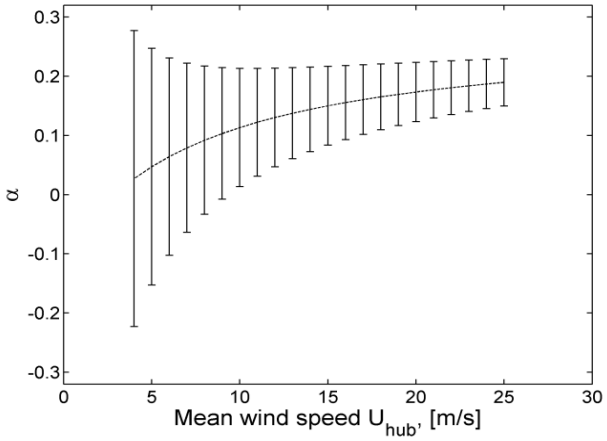

Figure 3.4 Proposed wind shear exponents for IEC specific design load calculations.

3.2 Turbulence intensity

Measurement of turbulence requires high frequency sonic anemometers (at least 20 Hz) and each obtained 10 minute time series needs to be de-trended, that is the mean wind speed must be a constant over the 10 minute period. The effect of de-trending on wind time series and its corresponding effect on the turbulence intensity assessment is shown in Fig. 3.5.

The IEC 61400-1 defines two models for turbulence intensity - the Normal Turbulence Model (NTM) and the Extreme Turbulence Model (ETM). Both models are based on the same assumption of the turbulence following a Lognormal distribution with mean conditionally dependent on wind speed, and with constant standard deviation. Observations from Høvsøre using high frequency sonic anemometers at different heights over a period of 9 years with de-trended wind time series show that:

- The assumption that the mean turbulence is linearly dependent on mean wind speed, and that the standard deviation of turbulence is a constant, can in general be used to describe the distribution of turbulence (Figure 3.6), although the standard deviation of turbulence also has close to linear dependency on wind speed and an improved description should take that into account;
-
- However, the expression $\sigma_{\sigma_U} = 1.4I_{ref}$ given in IEC61400-1 significantly underestimates the value of the standard deviation of turbulence. Measurements show that the correct expression should be approximately $\sigma_{\sigma_U} \approx 3.0I_{ref}$. The effect of this disagreement is visible when comparing the ETM model which should correspond to events with 50-year return period to measurements – Figure 3.7 shows an example from Høvsøre where the site-specific ETM contour is exceeded numerous times during 3 years of observations.

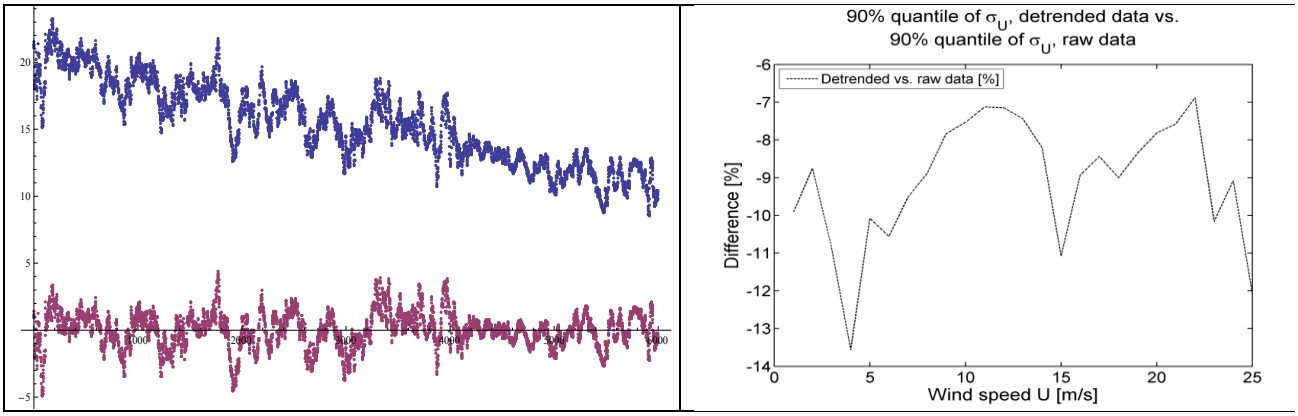

Figure 3.5 Example of linearly de-trending measured wind time series and its corresponding impact on the turbulence intensity

An update of the NTM and ETM models in the IEC61400-1 was suggested based on the observations above, where the turbulence is defined as Weibull-distributed, with the mean and variance as linear functions of wind speed, and resulting in preserved NTM-model values and wider contours for the ETM model.

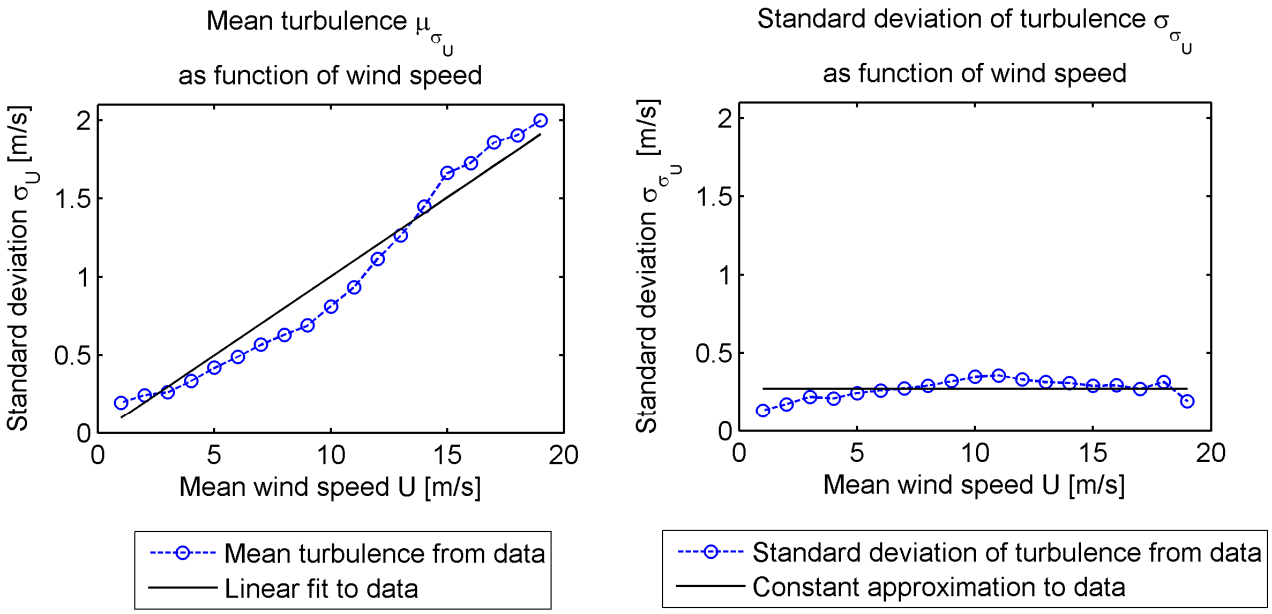

Figure 3.6 Turbulence as function of average wind speed, data from Høvsøre.

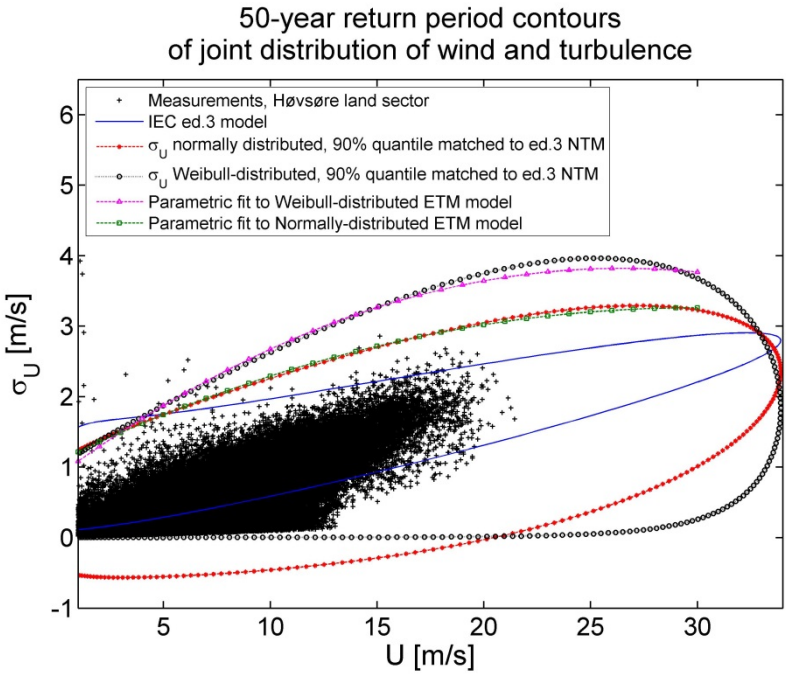

Figure 3.7: Turbulence observations covering a 3-year period vs. turbulence with estimated 50-year return period based on the ETM model from the IEC 61400-1, ed.3 standard, and two possibilities for an updated ETM model.

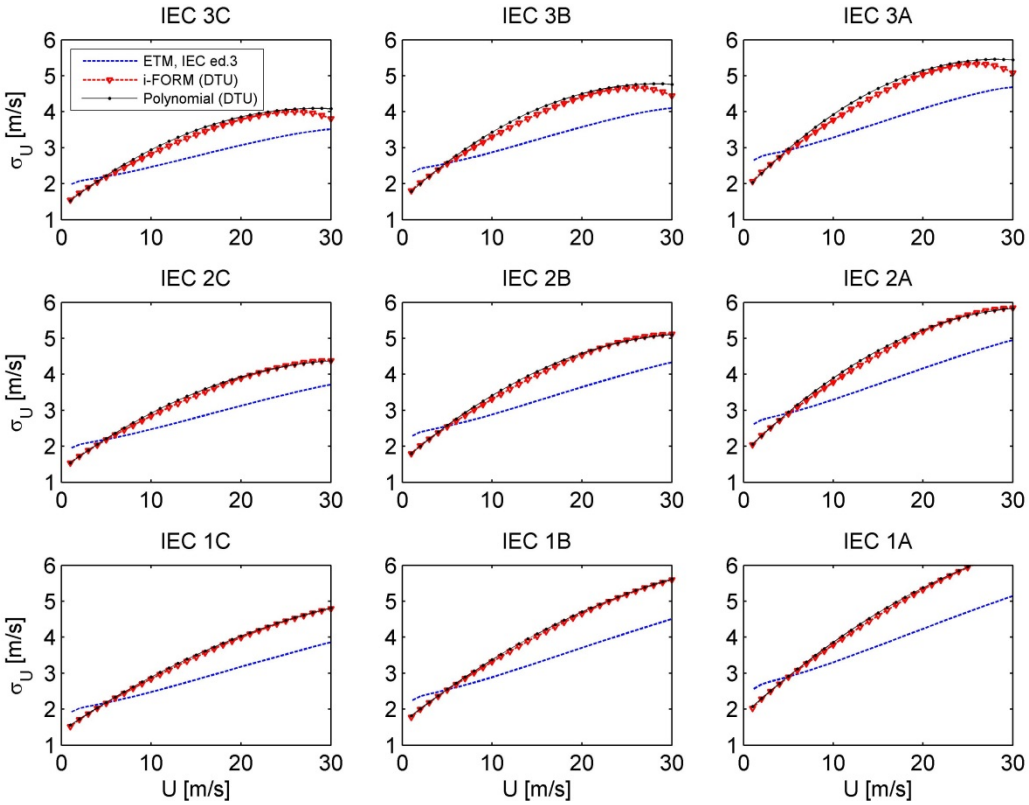

Figure 3.8 Comparison between the proposed ETM model and the reference model in IEC 61400-1, ed.3.

3.3 Turbulence spectral model

Turbulence boxes used in aeroelastic load simulations are generated using a parameterized spectral definition such as the Kaimal or the Mann spectral models. The spectral parameters recommended by IEC 61400-1 result in almost identical spectra of the Mann and Kaimal models, however the wind conditions corresponding to these spectral characteristics rarely occur in practice. During the Tallwind project, the mast measurement data at Høvsøre was used to identify typical spectral parameters for the wind at heights relevant for tall wind turbines. A software program was created for fitting Mann model parameters to measured wind time series, which was used for estimating Mann model spectral parameters under different turbulence conditions (Figure 3.9). The findings were used in a study (submitted as a journal paper, Dimitrov et al. 2014-2), which demonstrated the effect of varying the spectral parameters of the Mann turbulence model on the fatigue and extreme loads of 5MW and 10MW wind turbine models. It was observed that:

- The Mann parameters for representing normal turbulence and extreme turbulence in loads simulations are different.
- The tower top tilt and yaw moments were the most affected by the alteration in the Mann turbulence parameters.
- Increasing the turbulence length scale can decrease the tower base fatigue moments, but decreasing the anisotropy parameter, Γ, increases the tower base fatigue moments. The combination of these parameter changes on the tower base fatigue cannot be predicted without simulations, but in general the combined effect tends to

increase tower base fatigue marginally, and to reduce tower top tilt and yaw moments.

- The blade root edgewise fatigue and extreme moments decrease with increased length scales.
- The effect of turbulence seeds on the extreme loads are sometimes more pronounced than the effect of Mann parameter variations, but the overall trend of extreme loads is altered when the Mann parameters are changed (Figure 3.9).

As the spectral parameters vary for different design situations, it is recommended that, in future versions of the IEC standard, model-specific spectral parameter sets are defined for using with the Normal Turbulence Model and the Extreme Turbulence Model. For turbine load calculations in general it may be beneficial to use site-specific turbulence spectral parameters as this will reduce the uncertainties in the design.

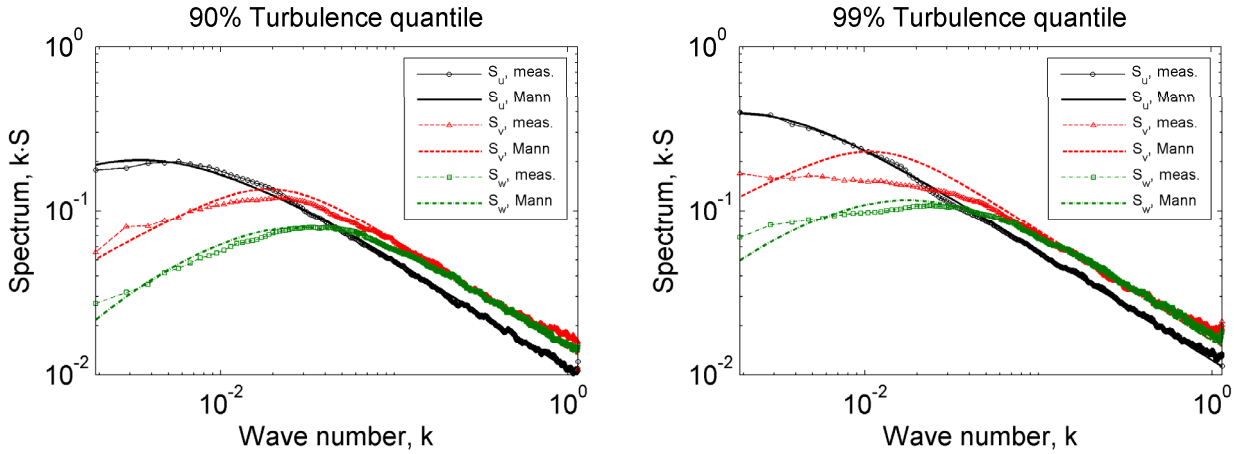

Figure 3.9: Mann spectra fitted to measurements at Høvsøre: a) at 11m/s and 90% turbulence quantile, and b) at 11 m/s and 99% turbulence quantile

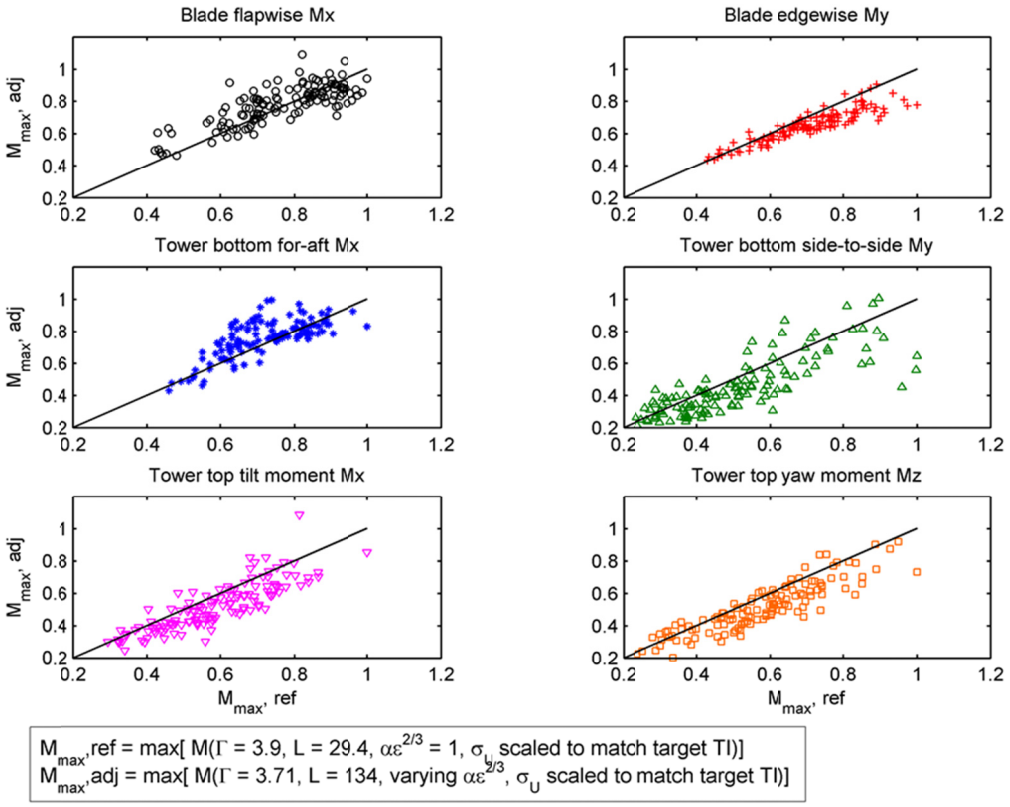

Figure 3.10: The effect of Mann model parameters variation from the standard IEC base as compared with variation in mean wind speed and turbulence seed, DTU 10MW reference turbine

4. Software to Simulate Tall wind time series

Objective

The objective is to develop a software that can transform a single Large-Eddy Simulation (LES) of the Atmospheric Boundary Layer (ABL) into wind time series for input to aeroelastic software such as HAWC2. The wind input is made as a grid centered at the hub height. Since the focus is on tall wind turbines, LES is ideal since it realistically captures shear and veer profiles throughout the entire ABL.

Two options are made:

1. A non-Gaussian turbulent inflow (the originally LES data).

2. A Gaussian turbulent inflow (exact same second statistics as the originally LES data).

In the following we will present the transformations and introduce the software to automatically obtain the HAWC2 wind input files from temporal snapshots of 3-dimensional turbulent data files.

The software (C++ routines) can be obtained for free by writing an email to Jacob Berg on jbej@dtu.dk.

Introduction to Gaussian vs non-Gaussian turbulence

In homogeneous isotropic turbulence, the probability density functions (pdf's) of the velocity components are Gaussian. This has been shown to be a good approximation both experimentally [8] and with direct numerical simulation [9]. Because of these results and numerical convenience many researchers studying wind loads on turbines from the naturally occurring atmospheric turbulence have used the assumption that the entire turbulent inflow field is Gaussian. Based on the work of Shinozuka [10, 11] Veers introduced an inflow turbulence generator based on spectra, such as the Kaimal spectrum [12], and two-point cross-spectra [13], while Mann proposed a model based on a three-dimensional spectra velocity tensor [14]. These models are now extensively used and are included in the International Electro-technical Commission on wind turbine loads.

However, turbulent fields are not Gaussian. Especially the smaller scales, characterized in terms of the statistics of velocity differences between points with some distance apart, exhibit large departures from a Gaussian distribution. Infinitesimal velocity differences such a vorticity and energy dissipation are very far from being Gaussian [15]. In the atmosphere the turbulence is also non-Gaussian at larger scales. This is for example seen in the large positive skewness of the vertical wind component under unstable atmospheric conditions over flat terrain whereas it is almost zero for neutral stratification. These deviations from normality are used routinely in dispersion modeling in the convective boundary layer, where the non-Gaussian pdf is modeled as a sum of several Gaussian functions. Large departures from Gaussian velocity fields are also expected in complex terrain. For example, highly positively skewed distributions of the along-

wind horizontal velocity component close to a canopy edge were observed [16,17]. Furthermore we might suspect intermittency in the recirculation zones surrounding complex terrain, although clear indications of this remains to be observed.
In order to clarify the role of non-Gaussianity on wind turbine loads investigators have deployed various simplified models that modify the statistics of the velocity field. Gong et al [18] used a Hermite polynomial transformation of a Gaussian field to produce fields with any given kurtosis, see also [19, 20]. This method requires some iterations to both match the (cross-)spectral densities and prescribed one-point pdf of the velocities. The method provides no guarantee that the pdf's of the velocity differences are realistic. Also, some physical properties of the fields, such as incompressibility and fluxes of momentum, may not be realistically obeyed.

Mücke et al [21] generated non-Gaussian time series with excess kurtosis by the method of continuous time random walks. The statistics of the generated velocity increments was Gaussian at large time scales but had large kurtosis at small scales. That was partly in contrast to their measurements which showed intermediate excess kurtosis at all-time scales. Their simulation model does not produce skewness of the velocity increments, which is a fundamental property of small scale turbulence. Nevertheless, they successfully reproduced the excess kurtosis of simulated rotor torque increments calculated from their Growian measurements of wind speeds from an array of anemometers where the corresponding Gaussian simulation had close to zero excess kurtosis. However, their rain flow load cycle counts from the Gaussian and non-Gaussian simulations were more or less identical, so it is not proven that non-Gaussianity in this case has influence on the loads. Methodologically, the continuous time random-walks does not easily match a prescribed spectrum hampering direct comparison with standard methods.

For the fields presented and tested in this report we use high resolution data generated with the pseudo-spectral LES code by [22]. The code simulates the ABL over a flat, homogeneous terrain with high temporal and spatial resolution. It should be highlighted that in principle any kind of LES generated data can be used, for example data from a different model.
In the current example we use 20 three-dimensional snapshots of the full velocity field, ui(x), between 50 m and 150 m (approximately the rotor size of a medium to large sized wind turbine) in the vertical and with horizontal dimensions (2.4 km × 2.4 km). The number of points in the snapshot is given by nx = 600, ny = 600 and nz = 41, while the spacial resolutions is Δx =4 m, Δy =4 m, and Δz =2.5 m. The snapshots are separated by approximately 10 min. The simulation is forced with a height independent geostrophic velocity of 5 ms−1 . The surface roughness is 0.3 m while the surface heat flux, (θ/w/)0, is zero. Above the boundary layer the lapse rate is slightly stable, dθ/dz =0.003 Km−1, allowing for entrainment of heat into the boundary layer, i.e. (θ/w/)z < 0, thus rendering the stratification conditional neutral. The height of the boundary layer is estimated to approximately 616 m.

Methodology and Program Calls

A number of steps are necessary in order to transform LES data to HAWC2 input. In the following list numbers in parentheses are only necessary for producing Gaussian inflow turbulence:

(1.) Preparing **ncarlesdb (2) SpectralTensor** (3.) **Representation HawcFiles**

The three steps (1-3) refer to C++ program executables, which are all build upon the same C++ Class, lescustom, containing information about file formats, structure and functions to manipulate these.

Preparing ncarlesdb

Information about the LES data is written in the .run file:

<inputdir> /Volumes/DISK2/Data/ned/3d/orig
<inputlabel> ned
<nx> 600
<ny> 600
<nz> 41
<nvar> 5
<x_l> 2400
<y_l> 2400
<z_{min}> 50
<z_{max}> 150
<u_{Gal}> 2.5
<t_{Ref}> 300

nx, ny and *nz* are the numerical dimensions of the data and *nvar* is the number of variables. In this case addition two variables are present (besides the three velocity components, *u, v* and *w*). The physical dimensions are x_l, y_l and $z_{min} : z_{max}$ (units in meters). The resolution in the giving example is then 4 m × 4 m × 2.5 m

Data should be oriented in Row-Major format (from slowest to fastest varying index): (i_z=*0*,*nz-1*); (i_y=*0,ny-1*); (i_x=*0,nx-1*); (*ivar=0,nvar-1*) and stored in binary format with 8 bytes reals (double-precision floating-point format).
In the case that the LES includes a Coriolis force and hence wind turning with height (veer), the coordinate system often reflect the direction of the forcing wind (a geostrophic wind aloft). In our example this is the x-direction. The coordinate system is right-handed.
Often (in order to achieve higher accuracy during computations) data are subtracted mean values in the main wind direction (x) (the coordinate system moves with a constant speed) and temperature. These are given as u_{Gal} and t_{Ref} with units of ms^{-1} and K, respectively.
Prefixes and suffixes of filenames are hard coded in the class constructor of lescustom.
Whereas the data dimensions and locations are written in the .run file, we write the information of the precise application usage in the .task file:

<l_{Zlevel}> 0
<u_{Zlevel}> 40
<d_{Zlevel}> 1
<nFiles> 20
<dFile> 5
<startFile> 0
<outputdir> /Volumes/DISK2/Data/ned/tmp

<outputlabel> ned20

l_{Zlevel}, u_{Zlevel} *and* d_{Zlevel} determine the lower level, upper level and level spacing, respectively, of levels to include. Remember that C++ starts counting from 0. Since nz=41 in this example, all levels are included. lnFiles, dFile and startFile determine the number of, and which snapshots to included. In this example files with number-id 0, 5,10,...,95 are used.

Information regarding the HAWC2 input files are given in .hawc file:

<nsnapshot> 20
<Ulower> 6
<Uupper> 24
<geofrac> 1.26
<nT> 4096
<T> 600
<ysize> 32
<zsize> 32

where nsnapshot is the number of realizations of every wind speed ranging from Ulower to Uupper in steps of 2 ms^{-1} (hard coded in **HawcFiles**). NT and T is the numerical and physical (in seconds) dimensions, respectively, of temporal length of the turbulence box with spatial dimensions, ysize and zsize. geofrac is a length stretching factor which determines the physical size of the turbulence box. With a height of zmax-zmin= 100 m, the turbulence box is 126 m wide and tall and also centered at 126 m, thus fitting a rotor with similar physical dimensions.

SpectralTensor

In horizontally homogeneous turbulence with horizontal wave numbers, k_x and k_y, the second order statistics is described by the spectral tensor given by

$$\Phi_{ij}(k_x,k_y, z, z') = \frac{1}{(2\pi)^2} \iint R_{ij}(\Delta x, \Delta y, z, z') e^{i(k_x \Delta x + k_y \Delta y)} \, dr_x dr_y \quad (1)$$

where

$$R_{ij}(\Delta x, \Delta y, z, z') = \langle u_i(x, y, z) \, u_j(x + \Delta x, y + \Delta y, z') \rangle \quad (2)$$

is the spatial covariance tensor. The discrete version of $\Phi_{ij}(k_x,k_y, z, z')$ is calculated by the Convolution Theorem in SpectralTensor. The spectral tensor is a very large numerical object. In our example in single precision it amounts to 41 × 41 × 600 × 600 four byte reals equivalent to 2.4 Gigabytes. Therefore take advantage of the symmetry (for a given set of wave numbers, k_x and k_y)

$$\Phi ij(z, z') = \Phi (z', z) \quad (3)$$

This mean that we only need to calculate $\Phi ij(z, z')$ for $z \geq z'$, which almost halves the amount of computations needed.

In our pseudo-spectral LES, the spatial filtering is done in Fourier space. In order to avoid dialiasing the upper 1/3 wave number in each horizontal direction is eliminated. This means that

only a factor of 4/9 of the individual wave numbers are actually non-zero and we can thus reduce the size of $\Phi_{ij}(k_x,k_y, z, z')$ even more.

Unix/MacOS Run command: SpectralTensor "yourlabel".run "yourlabel".task

Representation

In Representation we construct Gaussian turbulence fields. The new Gaussian fields have the exact same second order statistics, as described by the spectral tensor, as the original LES data (and calculated with **SpectralTensor**). The fields are also incompressible.

We will generate the Gaussian fields using 3nz basis functions, $\varphi^{(n)}$, which are eigenfunctions of the Karhunen-Loève integral [8]

$$\int_{z_{min}}^{z_{max}} \Phi_{ij}(k_x, k_y, z, z') \varphi_j(k_x, k_y, z')dz' = \lambda(k_x,k_y)\varphi_i(k_x,k_y,z) \quad \text{- (4)}$$

This procedure is performed for every pair of kx and ky. Using the the trapezoidal rule one can easily expand the left hand side for a given kx and ky (which may be omitted in the notation for clarity) and obtain the discrete eigenvalue problem

$$\mathbf{A}v = \lambda v, \quad \text{- (5)}$$

where *A* is a 3nz × 3nz matrix with complex eigenvectors given by

$$v = \{\varphi_1(z_{min}), \ldots, \varphi_1(z_{max}),\varphi_2(z_{min}), \ldots, \varphi_2(z_{max}),\varphi_3(z_{min}), \ldots, \varphi_3(z_{max})\}, \text{-(6)}$$

with normalization

$$\int \varphi(z)^{(m)}\varphi(z)^{(n)*}dz = \delta_{mn} \quad \text{- (7)}$$

where δ denotes the Dirac Delta function and * denotes conjugation.

3. A representation of the velocity field, $u_i(x, y, z)$ can then be constructed from (here given in Fourier space)

$$u_i(k_x,k_y,z) = \sum_n^{\infty} a^{(n)}(kx, ky)\varphi_i^{(n)}(kx, ky, z) \quad \text{- (8)}$$

where $a^{(n)}$ are uncorrelated coefficients. Solving eq. 8 we get

$$a^{(n)}(k_x,k_y) = \int u_i(kx, ky, z)\varphi_i(n)(kx, ky, z)dz \quad \text{- (9)}$$

From the above equations it can easily be verified that the the coefficients a(n) are

$$\langle a^{(n)}(k_x,k_y)\, a^{(m)*}(k_x,k_y)\rangle = \lambda(n)(k_x,k_y)\delta_{nm} \quad \text{- (10)}$$

For the Gaussian turbulence we want to leave all second order statistics unchanged. This is fulfilled by the following expression:

$$u_i^g(k_x, k_y, z) = \sum_n^N \gamma(n)\sqrt{\lambda(n)(k_x, k_y)}\varphi_i^{(n)}(k_x, k_y, z) \quad \text{- (11)}$$

where γ(n) is a complex Gaussian stochastic variable with zero mean and unit variance (equally distributed on the real and imaginary part). Inserting eq. 11 into eq. 9 we recover eq. 10

Unix/MacOS Run command**: Representation "yourlabel".run "yourlabel".task**

A horizontal plane of a constructed Gaussian velocity field, u_i^g at z = 100 m is presented in Figure 4.1. The top panels show the x-component, which is aligned with the geostropic wind, not the local mean wind direction. Since the LES field is a snapshot in time and the Gaussian field is a time-independent construct it is difficult to compare actually magnitudes of velocity components. It does, however, look like the maximum values are slightly reduced. The spatial structures in the Gaussian field are smaller and looks more erratic compared to more fluid-like structures, viz a Michelangelo sketch, in the original LES. The bottom panels show the vertical z-component. The picture is now even more pronounced: the swirling-like fluid structures in the original LES (left) is completely gone in the Gaussian field.

HAWC2 Fields

HAWC2 input consists of time series of 10 min of spatial varying turbulence covering the rotor area. In this example we use a turbine with a rotor diameter of 126 m and a similar hub height at 126 m. In order to meet these dimensions from the given LES fields and taking into consideration the fact that a full load simulation needs many different inputs with varying mean wind speed at hub height, the following steps are carried out inside HawcFiles:

- All physical dimensions are stretched a factor of 1.26 (geofrac) in order to meet the rotor dimensions of the wind turbine in question.
- All wind speeds are rescaled to match the desired hub height wind speed in question.
- The coordinate system is rotated so that the mean wind vector is along the x-axis at hub height.

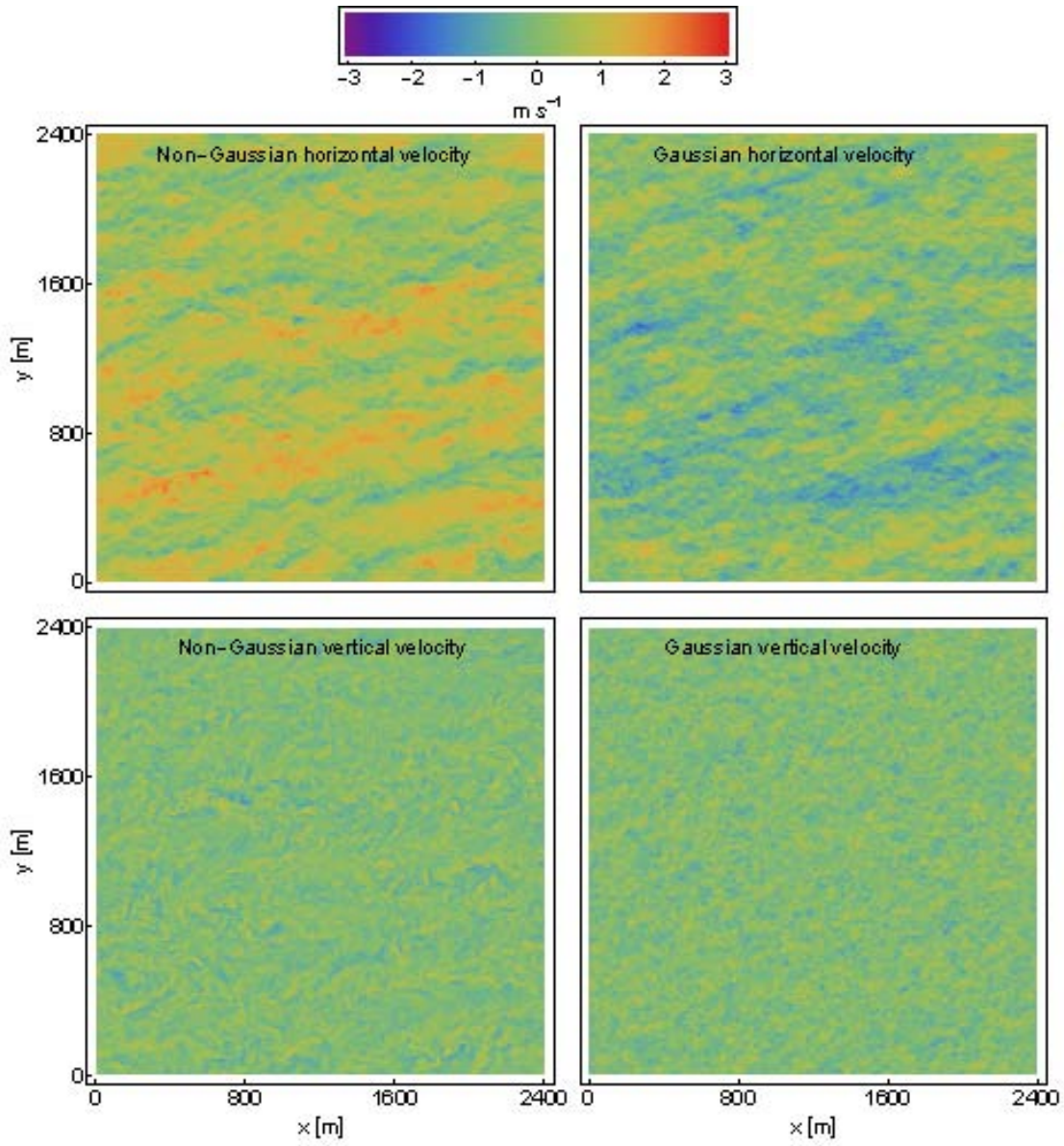

Figure 4.1: Horizontal plane at z = 100 m of u (top) and w (bottom) from the full LES field (left) and t Gaussian fields (right).

The final time series are created by advecting y − z planes past a virtual plane-sensor. We thus rely in Taylor's frozen turbulence hypothesis. Different realisations of each flow configuration (constant mean wind speed at hub height) are generated by using different seeding of the Gaussian random numbers in eq. 11.

In the optimal situation levels of velocities are saved covering the whole rotor plane, and thus geofrac can be set equal to one. The aforementioned multiplication of all velocities with a constant factor has some consequences: In physical terms it means that all terms in the governing equations are scaled (the LES equations -i.e. the spatial filtered Navier-Stokes equations). With no viscous dissipation in the LES governing equations the only terms which do not scale accordingly is the Coriolis force and the subgrid-scale (SGS) term. Since the SGS term is very small at the heights of interest (50-150 m) only the Coriolis term is important: multiplying all velocities with a constant factor larger than one thus has the consequence that the Earth spins faster or the latitude is increased. I.e. the turbine is in practice positioned further to the north. We do not expect this effect to impact the difference between the loads obtained from of the HAWC2 simulations of the original LES time series and the Gaussian counterpart, respectively, since the non-Gaussian part is not expected to change significant due to a change in the Coriolis force. As an example, we show (Figure 4.2) the pdf of the vertical velocity increments, $\delta w(\tau) = w(t) - w(t+\tau)$, of different time lags, τ =1, 7 and 30 seconds. The pdf for U =6 ms−1 (blue curves) is clearly non-Gaussian at τ =1 s, i.e. at the smallest scales while it becomes Gaussian at τ = 30 s. For the higher mean wind speeds depicted, U = 14 ms−1 (yellow curves) and U = 22 ms−1 (green curves), the temporal scales at which the pdf turns Gaussian decreases. This is a consequence of the scaling of velocities performed. The inset presents the normalised fourth order structure function, the kurtosis, of the pdfs for U =6 , 14 and 22 ms−1 as a function of Uτ. The collapse and the expected convergence towards the Gaussian kurtosis value of 3 are evident.

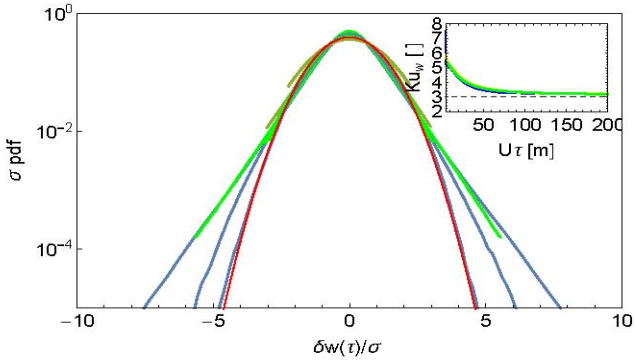

Figure 4.2: Pdf of vertical velocity increments, δw(τ). The three curves for each wind speed, U = 6 ms−1 (blue curves), U = 14 ms−1 (yellow curves) and U = 22 ms−1 (green curves), represent time lags, τ, of 1 s, 7 s and 30 s, respectively. The red curve i

Unix/MacOS Run command:

HawcFiles "yourlabel".run "yourlabel".task "yourlabel".hawc

The final output is a number of output files named:
<outputlabel>_"j"_U"U"_
<nT>x
<ysize>x
<zsize>T
<T> s_"snapshot".bin

In the filename "j" denotes the velocity component, U, V or W, and "snapshot" is an id. In our example "snapshot" runs from 0 to 19 since outputlabel= 20. "U" is the mean wind speed at hub height and is running from Ulower=6 toUupper= 24 in steps of 2 ms^{-1}. This results in 10 different mean wind speeds. Upon executing HawcFiles we thus create 3*20*10=600 files. The first would be named:
ned20_U_U6_4096x32x32T600s_0.bin

while the last one would be named:

ned20_W_U24_4096x32x32T600s_19.bin

4. Data in the output files are saved in Row-Major format (from slowest to fastest varying index): (it=0,nT-1);(iy=0, ysize-1);(iz=0,nsize-1) and stored in binary format 4 bytes reals (single-precision floating-point format).

It is important to emphasise that even though the three velocity components are saved in different files they are not independent of each other. By reading all three files one can reconstruct the cross-correlations found in the LES, which in this context is of utmost importance when calculating wind turbine loads.

Examples and Verification of HAWC2 wind input

In order to verify the Gaussian fields generated through eq. 11 we compare them with similar ones constructed from the original LES velocity field snapshots.

1. First we compare statistical moments. These are presented in Figure 4.3. The original LES and Gaussian profiles for co-variances (panel a) and variances (panel b) show very similar values: the vertical structure is reproduced within the error bars (standard deviations of the mean).

2. Moving to the skewness, the normalised centralised third order moment (panel

c), and the kurtosis the normalised centralised fourth order moment (panel d), the Gaussian transformation becomes very clear: Whereas the original LES data display the pronounced positive skewness for the w component (green curve in panel c) and slightly negative values for the horizontal components, u and v, all three components approach zero skewness in the Gaussian case as expected. For the kurtosis the picture is similar: In the Gaussian case all three components approach the value 3.

We have also compared the spectral properties; one point spectra, horizontal and vertical spectral coherences and phases, directly important for the wind loads on turbines, between the non-Gaussian and Gaussian fields. We found a similar agreement (not shown) as presented in Fig. 3.

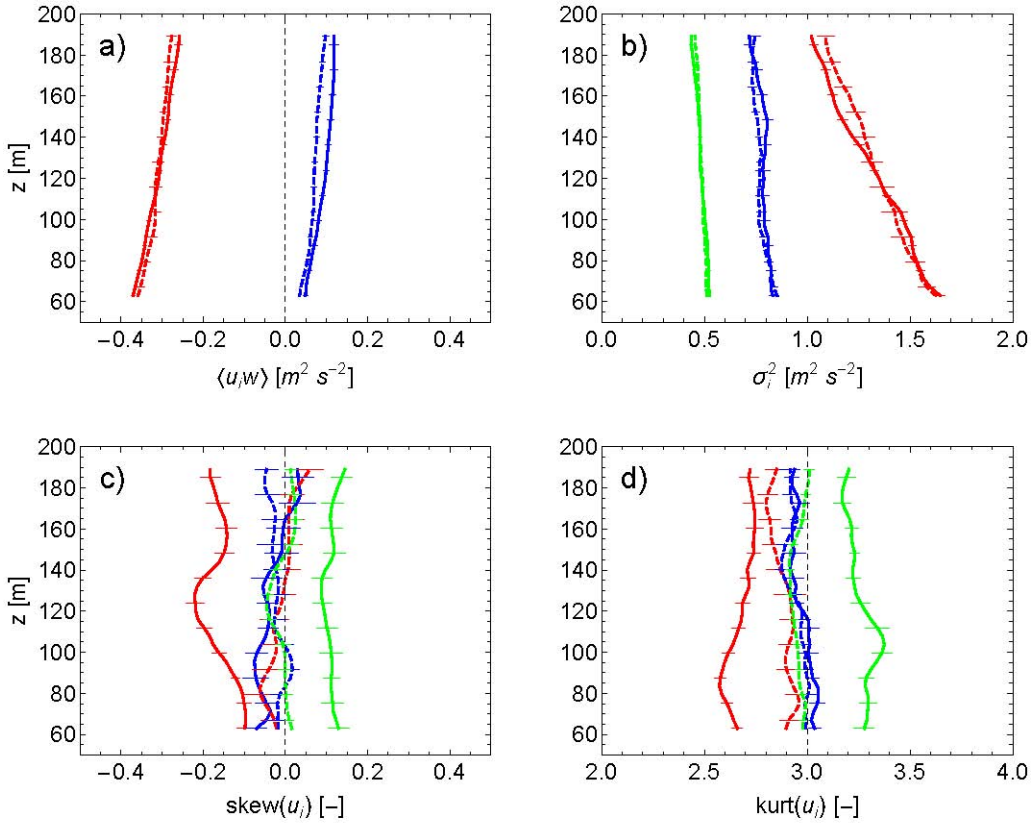

Figure 4.3: Moments remeshed time series based on the original LES (solid lines) and the Gaussian (dashed lines), respectivily. a) Co-variances: (uw) (red) and (vw) (blue). b) Variances: σu (red), σv (blue) and σw (green). c) Skewness: skew(u) (red), skew(v) (blue) and skew(w) (green). d) Kurtosis: kurt(u) (red), kurt(v) (blue) and kurt(w) (green). Error bars are the standard error of the mean and N = 20.

External Libraries

Besides standard C++ libraries we make use of the following:

- Fourier transforms: FFTW version 3.3.3 (www.fftw3.org).
- Linear Algebra: Eigen version 3.2.2 (http://eigen.tuxfamily.org).

Both libraries are statically linked to the executables.

5. Component load distributions for combined shear and veer distributions

Introduction

The flow field in the atmospheric boundary layer is basically non-stationary, in the sense that the flow characteristics changes with/over time. However, mostly for mathematical convenience, the non-stationary physical nature of a turbine exposed to atmospheric boundary layer flow is often approximated as a stationary problem. This is a considerably simplification. As a consequence, the external wind turbine loading is in design simulations traditionally split in a (periodic) deterministic part and a purely stochastic part. The deterministic part includes horizontal/vertical wind shear, wind veer, gravity, tower shadow etc., whereas the stochastic part is caused by wind field turbulence.

Although *wind shear* and *wind veer* driven loading in a short term perspective (i.e. within a traditional 10-minute reference period) traditionally is characterized as pure deterministic loading, the site specific characteristics of these external load types will in practice typically vary from reference period to reference period, and consequently such characteristics should be considered as stochastic variables in a larger time frame.

In the above perspective, the goal of the present investigation is to define *recommended design values* for shear and veer, respectively, for a flat and homogeneous terrain on a rational basis. In the present context, recommended values will mean shear/veer specifications that ensure the structural integrity of a wind turbine structure up to the 98% quantile in the fatigue load response probability density function (pdf) or, in other words, limit the probability of the shear/veer driven turbine fatigue loading exceeding the design value to 2%. For fatigue driven load cases, this is believed to be consistent with the philosophy behind the IEC-61400-1 code for wind turbine design [1], and the results should therefore be of potential interest future code revisions.

The investigation will take advantage of a newly developed “pseudo” Monte Carlo approach which, among other advantages, facilitates “inverse engineering” in the sense that a specific quantile in the load response pdf, for a given load sensor at a given wind turbine component, can be consistently tracked back to the input pdf’s of shear/veer, although this problem not necessarily is unique in a pure mathematical context neither for the individual load sensor, nor for the turbine as a whole.

5.1 Shear- and veer input

In agreement with the results presented in Chapter 2 of this report, we will consider *flat terrain* only with vegetation being representative for conventional farm land vegetation as well as mixed forest and grassland. Further, the *explicit* effect of atmospheric stability (i.e. buoyancy) on shear and veer is disregarded in the first place, but the effect of buoyancy is, however, *implicitly* included in the available shear and veer pdf’s. Referring to Table 1 in Chapter 2, it should be mentioned that the “true” stability climatology are not necessarily well represented in the part of present analysis based on the Østerild and the ‘MR’ data. This is due to the limited amount of data available for those analyses (i.e. 1 year), which affects the statistical significance of the results.

The detailed load analysis is to be based on a large number of aeroelastic simulations. As input for these we need to define mean wind shear and veer profiles as well as the stochastic variables quantifying the magnitudes of such profiles.

5.2 Shear

For the mean wind speed variation with height above ground, we will adopt the power law formulation suggested in the IEC-61400-1 code [1]. The shear profile is thus given by

$$U(z) = U(z_r)\left(\frac{z}{z_r}\right)^{\alpha}$$

where $U(z)$ is the mean wind speed at height z above terrain, and z_r is a reference height (here taken to be the turbine hub height). α is the mean wind shear exponent, which in the present context also serves as the stochastic variable describing the mean wind shear stochastic variability.

The statistics of α will be based on the results from Chapter 2 of this report. Due to differences in instrumentation for the investigated sites, these results refer to imaginary hub heights, which vary moderately between the sites (cf. Table 1 of Chapter 2). We will disregard this variation, and assume that the derived shear statistics are applicable for the hub height of the intended NREL 5MW model turbine (cf. Section 4 of this Chapter). We will, in other words, assume that the mean wind speed gradient estimate, $dU/dz = (U_{upper} - U_{lower})/(z_{upper} - z_{lower})$, does not depends significantly on the variability between the imaginary hub heights.

The analysis in this chapter will be based on *marginal shear distributions*, although the results of Chapter 2 shows that shear and veer are correlated, and the load analysis therefore ultimately should be based on joint their statistics. This issue will be addressed in a forthcoming publication by Larsen *et al.*.

Consistent with the fact that part of the shear exponent variability is caused by buoyancy effects, the derived statistics show dependence with the mean wind speed, and the load analysis will therefore be based on shear statistics conditioned on mean wind speed (at hub height z_H). The estimated conditional distributions refer to mean wind speeds at heights $z_{mid} = ½(z_{upper} + z_{lower})$ which, as mentioned, differ from the hub height of the model wind turbine but, however, is of the same order of magnitude. No attempt will be done to “transform” the shear exponent distributions conditioned on the individual site z_{mid} mean values to shear exponent distributions conditioned on the model turbine hub height mean wind speed. This is motivated by the inherent mutual variability among estimated site distributions, as well as by the final result of the analysis being based on an arbitrary choice of model turbine. Examples of marginal conditional shear distributions from the Østerild site are shown in Figure 5.1.

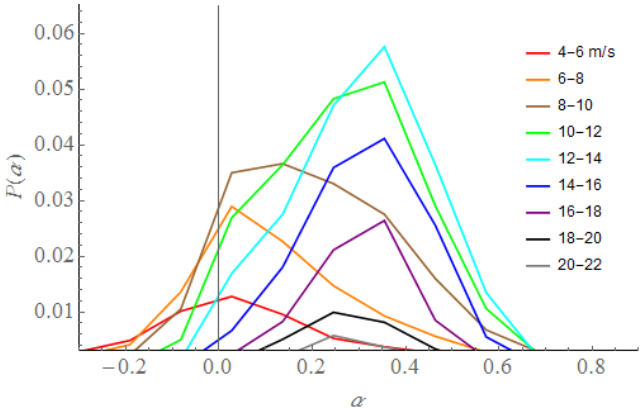

Figure 5.1: Marginal conditional shear distributions estimated for the Østerild site.

5.3 Veer

In analogy with the shear analysis, we need a generic shape of the mean wind direction variation with height above ground (i.e. a veer profile). For this purpose we take advantage of a result derived in a forthcoming paper by Kelly *et al.*, which, to second order in (z-z_H), can be Taylor expanded to give

$$\varphi(z) - \varphi(z_H) \approx a_\varphi e^{-\sqrt{z_H/h_{ME}}} \frac{(z - z_H)}{\sqrt{z_H h_{ME}}} \left[1 - \frac{(z - z_H)}{2\sqrt{z_H h_{ME}}} - \frac{(z - z_H)}{4z_H}\right]$$

where φ denotes the wind veer, h_{ME} is the modified-Ekman atmospheric boundary layer (ABL) depth, and a_φ is the stochastic variable quantifying the variability of wind veer over the wind turbine rotor. For the present investigation we take the modified-Ekman ABL depth to equal h_{ME} = 500m.

For $|z - z_H| \ll 2\sqrt{z_H h_{ME}}$, we see that the veer profile is effectively linear. However, since $|z - z_H|$ might be as big as perhaps ¾ of z_H, then we might expect some significant deviations from linearity not only for very stable (shallow) ABL's, but also for very large blades. For the present case, the deviation from a strictly linear behaviour clearly appears from Figure 5.2.

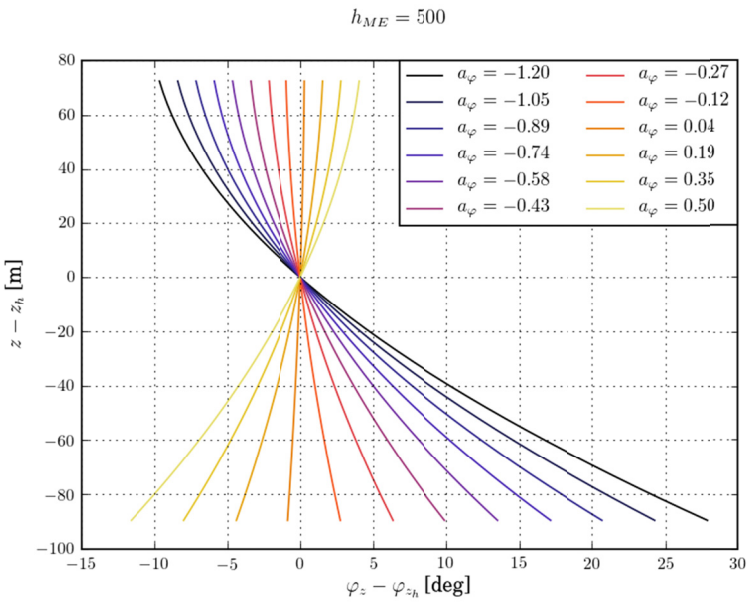

Figure 5.2: Veer profiles covering the investigated range of the a_φ parameter.

From Chapter 2 of this report, it appears that shear and mean wind speed is correlated, and further that shear and veer are correlated. Veer and mean wind speed is therefore also correlated, and in analogy with the approach for the shear investigation, we will base the present veer analysis on *marginal veer distributions* conditioned on the mean wind speed. Also in analogy with the shear investigation, we will assume that the estimated veer statistics, associated with the various investigated sites, are directly applicable for the conditions at hub height of the intended NREL 5MW model turbine. As an illustration, examples of conditional marginal veer distributions from the Østerild site are shown in Figure 5.3.

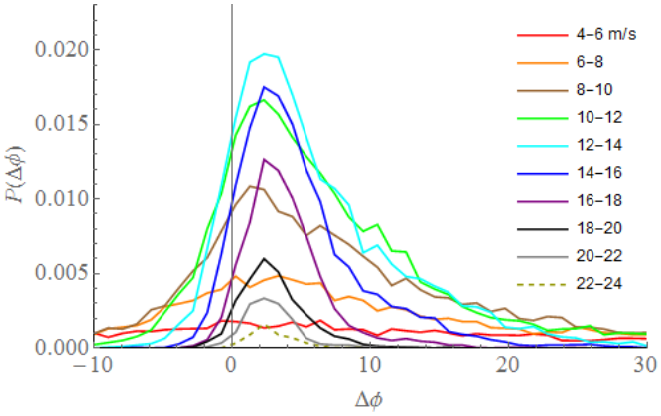

Figure 5.3: Marginal conditional veer distributions estimated for the Østerild site.

5.4 Pseudo Monte Carlo approach

The mail goal of the present analysis is to map (individually) the *marginal* conditional shear and veer distributions on selected pdf's associated with predefined load sensors on turbine main components (cf. Section 4 of this chapter); and moreover to be able to consistently track back

arbitrary load (sensor) quantiles to quantiles of the driving stochastic forcing under consideration (i.e. shear and veer) for definition of design shear and veer profiles on a rational basis.

For treating these singe-input multiple-output systems we will take advantage of classical theorems for transformation of stochastic variables. The approach is briefly summarized in the following and described in more detail in a forthcoming paper by Larsen *et al.* Apart from paving the way for solving the inverse problem (i.e. determination of shear/veer profiles leading to a particular component fatigue loading), the approach has the additional advantage to classical Monte Carlo simulations that it leads to a straight forward decomposition of the input marginal distributions on the one side and the requested transformation, formulated in terms of aeroelastic computations and suitable/arbitrary post processing of the results of such, on the other side. This in turns means that once the requested transformation is established, which may involve a substantial amount of aeroelastic computations, then determination of load/output pdf's, as based on arbitrary input pdf's, are obtained using a minimum of CPU requirement. For investigation of numerous input pdf's, like in the present analysis, this type versatility is very convenient.

Let a stochastic variable, ξ, characterize some type of external inflow conditions (e.g. mean wind shear or mean directional veer), and l be a stochastic variable characterizing some resulting wind turbine structural response (e.g. fatigue equivalent moment associated with a main component cross section or extreme blade tip deflection for investigation of tower clearance). Thus

$$l = L(\xi|\boldsymbol{u})$$

where $L(\bullet)$ is a transformation function which, in this case, relates external wind loading with the structural response signal in question, conditioned on the *turbulent inflow conditions* characterized by $\boldsymbol{u}$. The reason for also including the turbulent inflow conditions in the transformation, L, is that the relationship connecting the overall inflow field with the structural response in general is strongly non-linear due to wind turbine control actions, in-stationary aerodynamic effects and/or large structural deflections.

The relationship between the pdf of ξ, f_ξ, and the requested pdf of l, f_l, is given as [23]

$$f_l(l) = \sum_{i=1}^{N} \frac{f_\xi(\xi_i)}{|L'(\xi_i|\boldsymbol{u})|}$$

where $(\bullet)'$ denotes differentiation with respect to ξ, and N is the number of ξ_i-roots satisfying the equation

$$l = L(\xi_i|\boldsymbol{u})$$

for a specific choice of l. It is straight forward to generalize this simple single-input/single-output system to a single-input/multiple-output system [23] and also possible to generalize to a multiple-input/multiple-output system [23].

Once the load transformation is defined, the "inverse tracking", relating an arbitrarily selected load quantile to quantiles of the driving stochastic forcing in a rational manner, is straight forward. This tracking is, however, *only unique* if the number of roots, N, in the above equation equals one. In this case, the inverse tracking is given by

$$\xi = L^{-1}(l|\boldsymbol{u})$$

The case where N is larger than one thus poses a "selection problem", which in the end will rely on a motivated definition. Two logical definitions/choices among the countable number of possible candidates, ξ_i, ξ_l, or, alternatively, the particular ξ_i contributing the most to the load quantile in question, ξ_m. In mathematical terms these are expressed as respectively

$$\xi_l = \left\{ \xi_l \middle| f_\xi(\xi_l) = \max_i f_\xi(\xi_i) \right\}$$

$$\xi_m = \left\{ \xi_m \middle| \frac{f_\xi(\xi_m)}{|L'(\xi_m|\boldsymbol{u})|} = \max_i \frac{f_\xi(\xi_i)}{|L'(\xi_i|\boldsymbol{u})|} \right\}$$

To the extent that a selection, as described above, becomes relevant for the present analysis of design load definitions, we will rely on the latter definition and thus relate the "inverse tracking" to ξ_m.

Numerical setup

As mentioned, the transformation, L, is determined *numerically* using the state-of-the-art aeroelastic code HAWC2 [24]. The structural part of HAWC2 is based on a multi-body formulation using the floating frame of reference method. Each body includes its own coordinate system with calculation of internal inertia loads, when this coordinate system is moved in space, and hence large rotation and translation of the body motion are accounted for.

The model turbine is the NREL 5MW turbine [25]. This turbine platform is chosen because it is a representative modern utility-scale multi-megawatt turbine, but also because all design parameters – ranging from aerodynamic and structural properties to control-system properties – are freely available; therefore this turbine has developed to a de facto reference turbine for research teams throughout the world.

The NREL 5MW wind turbine is a conventional three-bladed turbine. The main features of this turbine appear from Table 5.1 below.

Table 5.1: Gross properties of NREL 5MW turbine.

Rated power	5MW
Rated wind speed	11.4 m/s
Rotor orientation	Upwind
Control	Variable pitch; Collective pitch
Rotor diameter/Hub diameter	126m/3m
Hub height	90m
Maximum Rotor/Generator speed	12.1rpm/1173.7rpm
Maximum tip speed	80m/s
Overhang/Shaft tilt/Coning	5m/5°/2.5°

This study focus on turbine *fatigue loads* as driven by Design Load Case 1.2 of the IEC 61400-1 code (normal operation). Turbulence class A is assumed, and the Mann spectral tensor is used for turbulence generation with parameters as specified in the code. As we aim at mean wind speed dependent design shear/veer, selection of a specific wind turbine class is irrelevant for this investigation.

The investigated load signals/sensors are in this context fatigue equivalent moment associated with turbine main component cross sections associated with a blade root cross section (flap wise and edge wise) and with tower top/tower bottom cross sections (tilt and sideways). Torsion related fatigue equivalent moments for both blade and tower have been excluded from this analysis, because the gradient of these loads with respect to the stochastic variable in question (i.e. shear parameter or veer parameter) are an order of magnitude less than the analog gradient of the fatigue bending moments, thus indicating an insignificant dependence of torsion fatigue loading on the shear/veer parameters.

For the fatigue life time, it is assumed the turbine will operate 97.5% of the time during 20 years (which is the fatigue damage contribution for DLC 1.2 of the IEC 61400-1 code). Further, the turbine is assumed to operate under yaw error for 50% of time (equally divided between +10 degrees and -10 degrees).

The load response is discretized according to computational scheme defined in Table 5.2.

Table 5.2: Computational scheme.

Parameter	***Range***	Bin size
Mean wind speed [m/s]	[4; 26]	2m/s (12 steps)
Yaw error	[-10;0;10]	(3 steps)
Shear exponent α	[-0.3; 0.9]	0.15 (12 steps)
Veer parameter a_φ	[-1.2; 0.5]	0.11 (12 steps)

To reduce variability in load response originating from an arbitrary realization of the turbulence field, ***u***, we will associate a sensor with the *arithmetic mean* of the particular fatigue response over 6 different ***u***-realizations. Additionally, for each mean wind speed the corresponding ***u***-realizations are unique (i.e. using 6×12=72 different turbulence seeds). Thus, with the computational scheme defined in Table 2 combined with 6 turbulence realizations, a total of 12×3×6×12×12=31104 independent 10 minute aeroelastic computations are conducted.

5.5 Shear results

Although shear and veer basically are correlated, we will as previously mentioned focus only on the *marginal shear distributions* in the present reporting. Because current state-of-the-art aeroelastic design computations assume zero veer, the results to follow are also conditioned on no veer (i.e. $a_\varphi = 0$).

Because of the discrete character of the directly obtained response pdf's, we must adopt a suitable interpolation scheme in order to resolve relevant quantiles with sufficient accuracy. For this purpose we use a dedicated spline-like approach developed in [26], which assures that the probability mass, associated with a particular bin, is preserved for the continuous C^3-interpolation.

Examples of (seed-averaged) response curves and their derivatives are shown in Figures 5.4-5.6 for mean wind speed equal to 12m/s. The derivatives are determined using a second order central difference scheme except for the "end points", where second order forward and backward approaches are used.

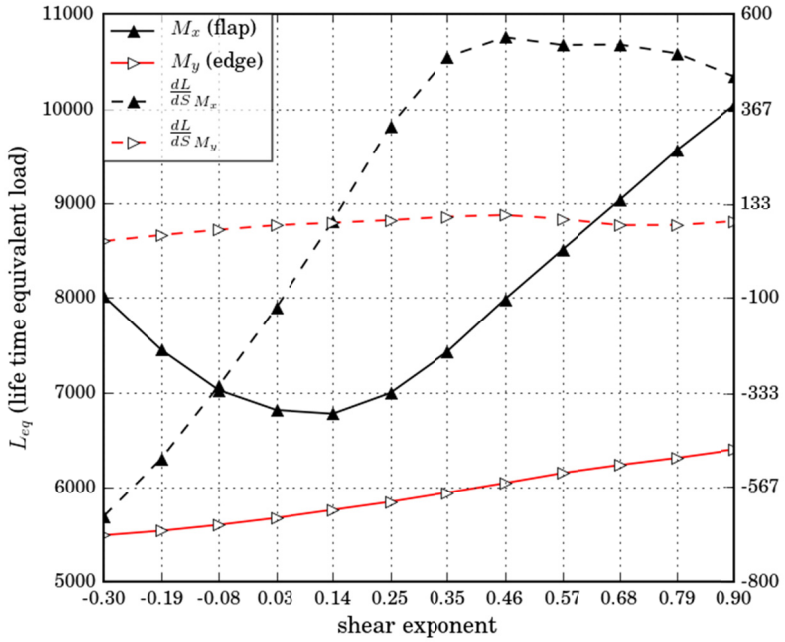

Figure 5.4: Load response function and its derivative for the blade root moments (flap and edge) as function of the shear exponent.

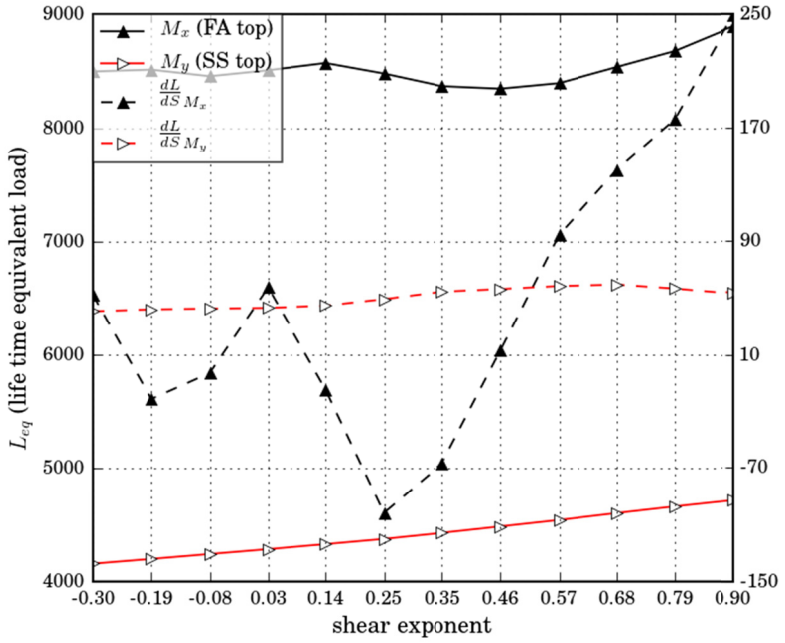

Figure 5.5: Load response function and its derivative for the tower top moments (tilt and sideways) as function of the shear exponent. In the plot tilt is abbreviated as FA, and tilt is abbreviated as SS.

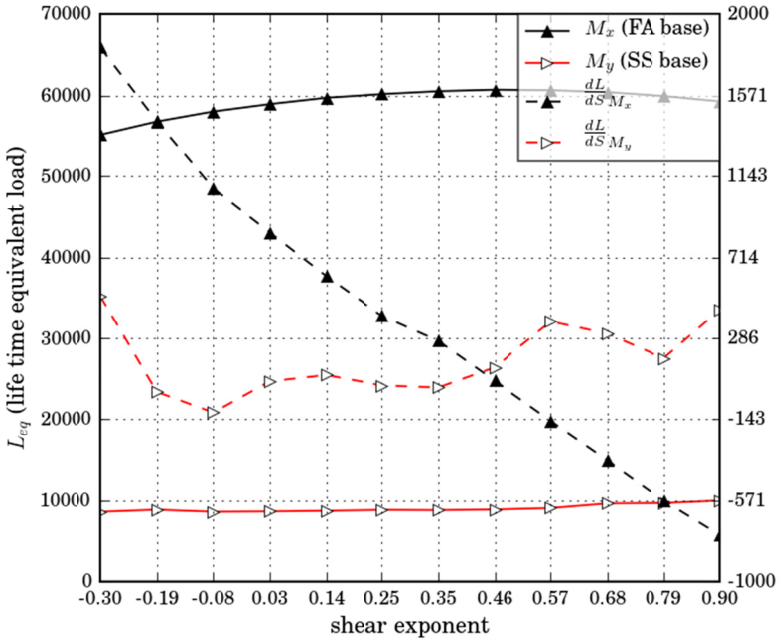

Figure 5.6: Load response function and its derivative for the tower bottom moments (tilt and sideways) as function of the shear exponent. In the plot tilt is abbreviated as FA, and tilt is abbreviated as SS.

The corresponding fatigue load pdf's and cumulative distribution functions (cdf's) are shown in Figures 5.7-5.12 as based on the Østerild marginal shear distribution. The vertical lines with an associated load magnitude specification identify the 98% quantiles in the response pdf's.

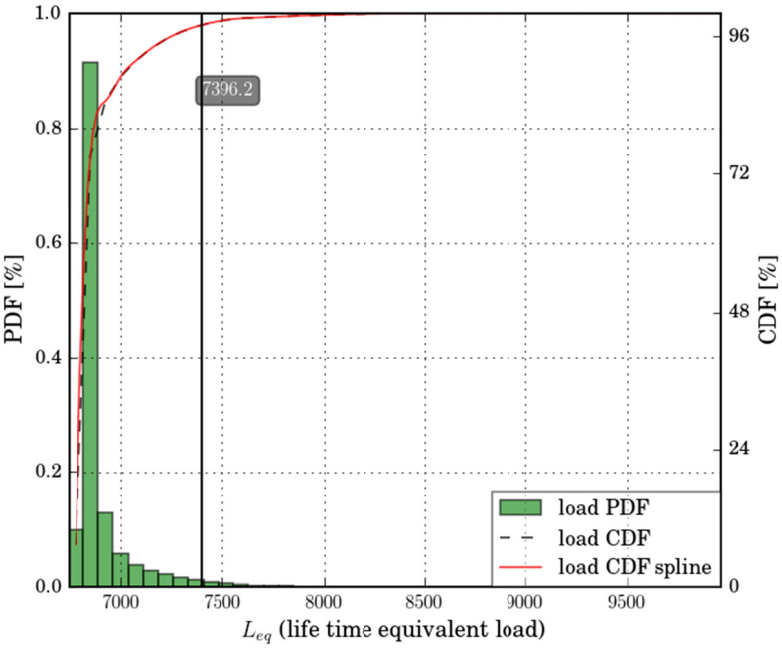

Figure 5.7: Load response pdf and cdf for the blade root flap moment.

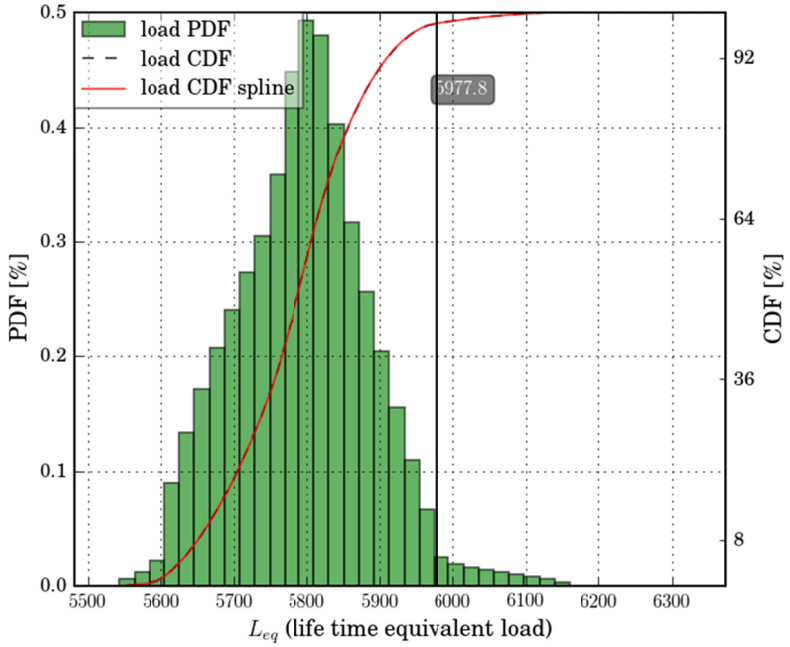

Figure 5.8: Load response pdf and cdf for the blade root edgewise moment.

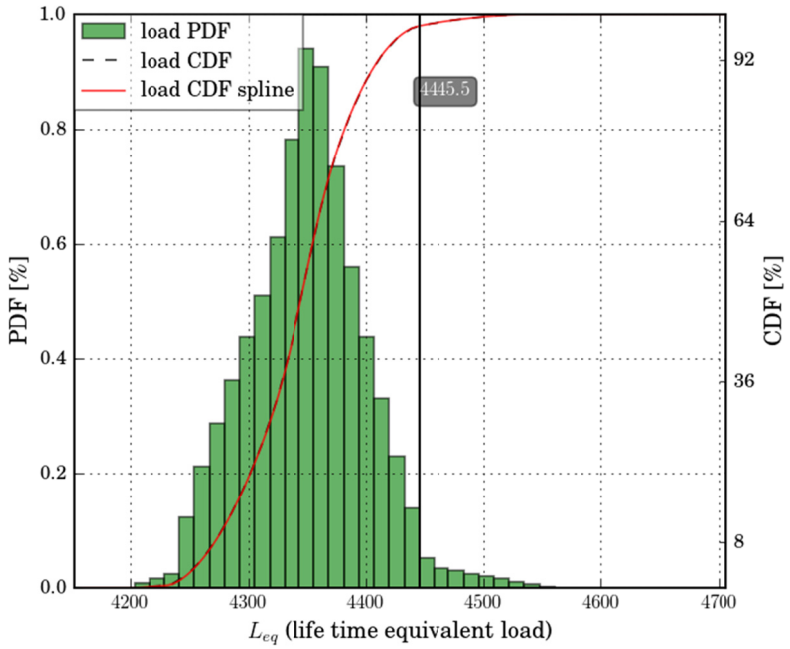

Figure 5.9: Load response pdf and cdf for the tower top sideways moment.

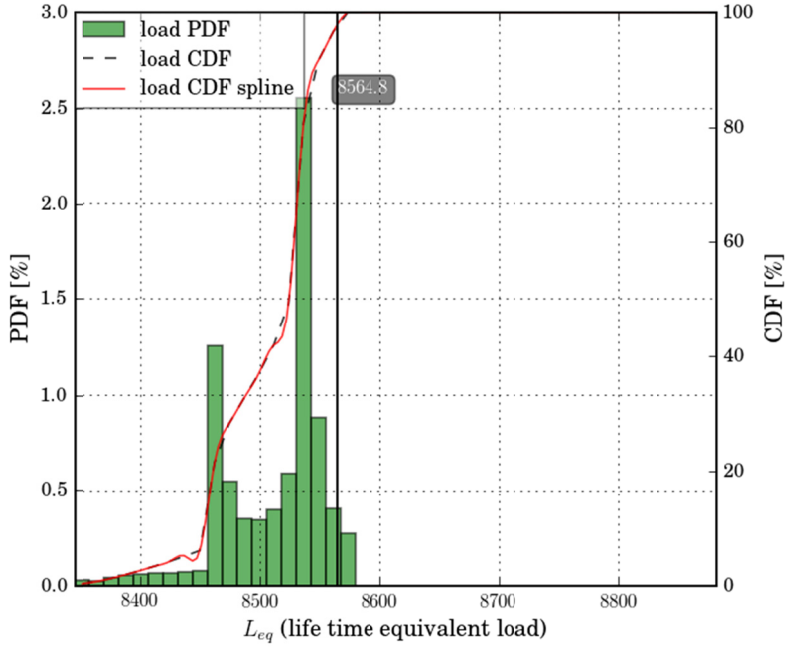

Figure 5.10: Load response pdf and cdf for the tower top tilt moment.

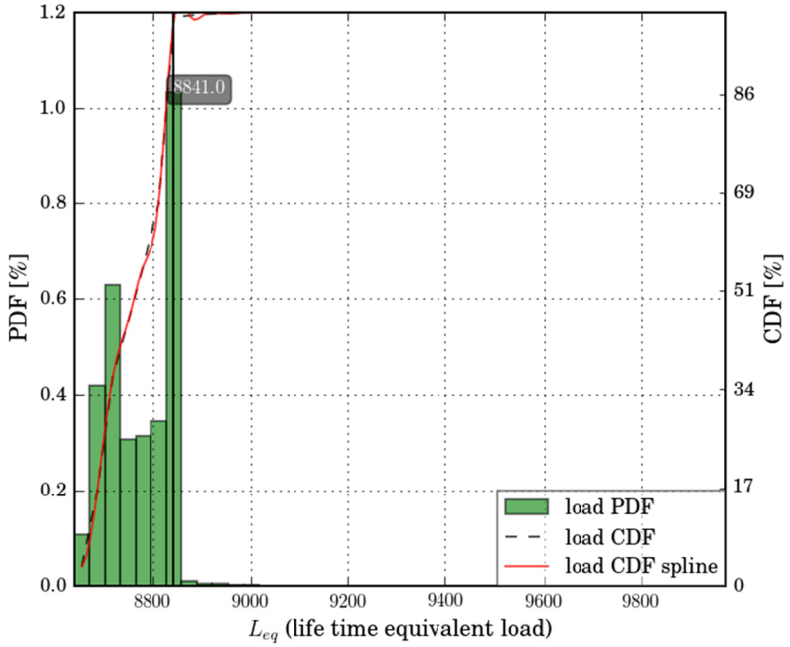

Figure 5.11: Load response pdf and cdf for the tower bottom sideways moment.

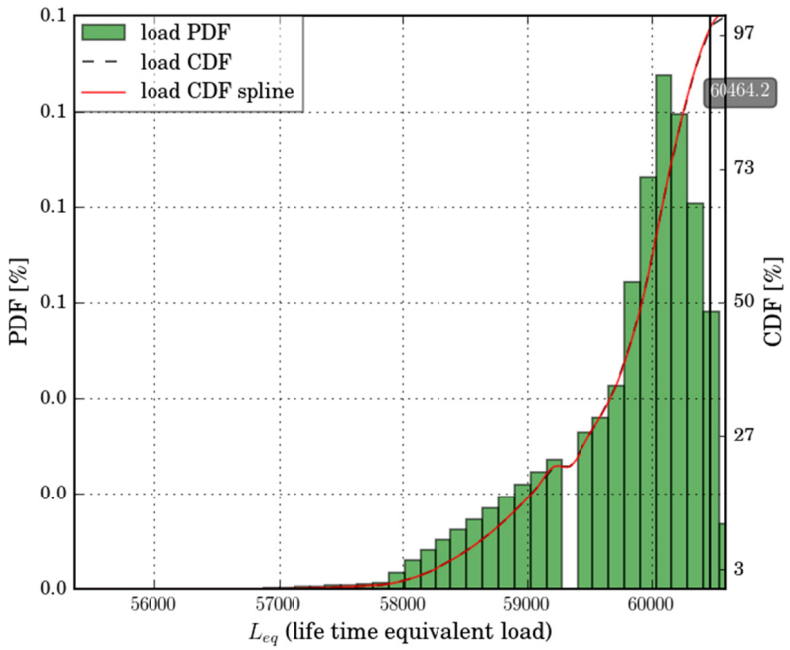

Figure 5.12: Load response pdf and cdf for the tower bottom tilt moment.

Disregarding the shear/veer correlation, the sought *design shear exponent*, α_d, is a function of the mean wind speed U, the turbulence field $\boldsymbol{u}$, the component load response l_i and the requested confidence level cl: $\alpha_d = \alpha_d(U, \boldsymbol{u}, l_i, cl)$. In the present formulation, we have already simplified the design shear exponent as $\alpha_d = \alpha_d(U, \langle l_i \rangle, cl | \boldsymbol{u})$, where $\langle \bullet \rangle$ is the ensample

averaging operator. Adopting a 98% confidence level, the design shear exponent, α_d, is described by a hyperplane defined by *cl* = 0.98. For the investigated load types the discrete representation of this hyperplane is summarized in Table 5.3.

Table 5.3: Design shear exponents as based on the Østerild marginal shear distribution.

Wind speed [m/s]	α_d *(flap)*	α_d *(edge)*	α_d *(tower bottom tilt)*	α_d *(tower bottom side)*	α_d *(tower top tilt)*	α_d *(tower top side)*
4	-0.154	0.325	0.332	-0.205	-0.202	-0.124
6	0.520	0.615	0.043	0.275	0.776	0.544
8	0.069	0.403	0.410	0.174	0.333	-0.067
10	-0.045	0.372	0.370	0.015	-0.279	0.366
12	0.323	0.391	0.577	0.273	0.312	0.384
14	-0.194	0.376	0.265	0.573	0.182	0.370
16	0.187	0.353	0.524	-0.229	-0.256	0.352
18	0.367	0.365	0.361	-0.013	0.862	0.370
20	0.417	0.430	0.494	0.380	0.143	0.435
22	0.262	0.331	0.209	0.151	0.598	0.346
24	0.148	0.355	0.254	0.126	0.233	0.348
26	-0.282	0.323	0.365	0.205	0.204	0.357

5.6 Veer results

Analogue with the shear, the focus in the present Section is on the *marginal veer distributions.* Consequently, the results to follow are conditioned on conventional shear (i.e. α = 0.2). Same considerations on interpolation and derivatives for the shear case apply for the veer case, and examples on (seed-averaged) response curves and their derivatives are shown in Figures 5.13-5.15 for mean wind speed equal to 12m/s and associated with the Østerild marginal veer distribution.

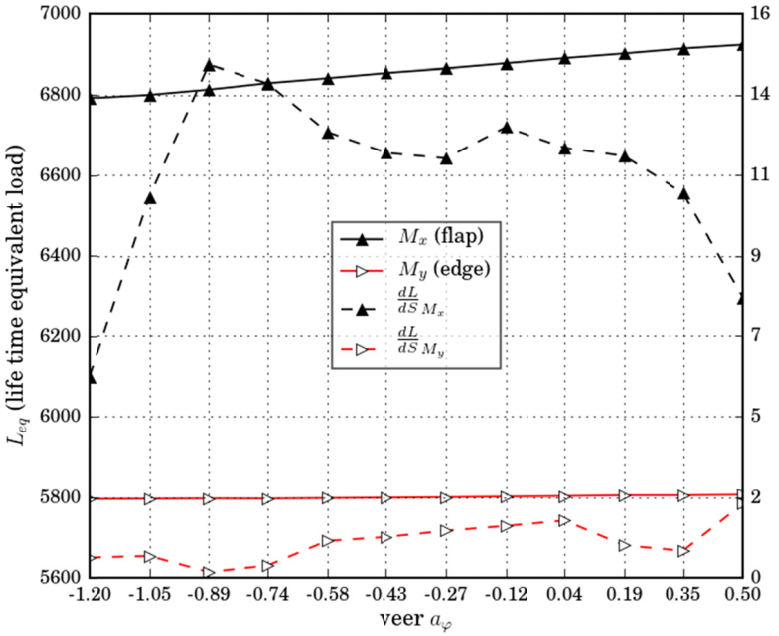

Figure 5.13: Load response function and its derivative for the blade root moments (flap and edge) as function of the veer parameter a_φ.

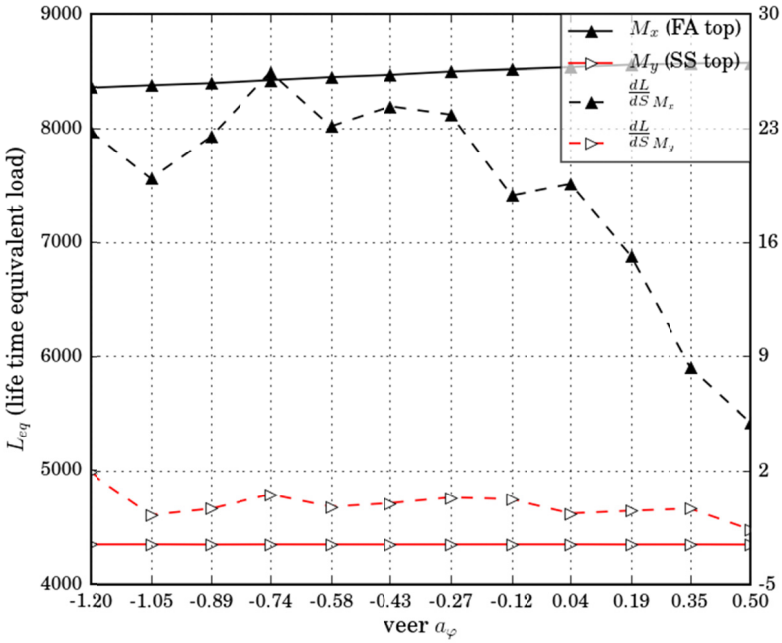

Figure 5.14: Load response function and its derivative for the tower top moments (tilt and sideways) as function of the veer parameter a_φ. In the plot tilt is abbreviated as FA, and tilt is abbreviated as SS.

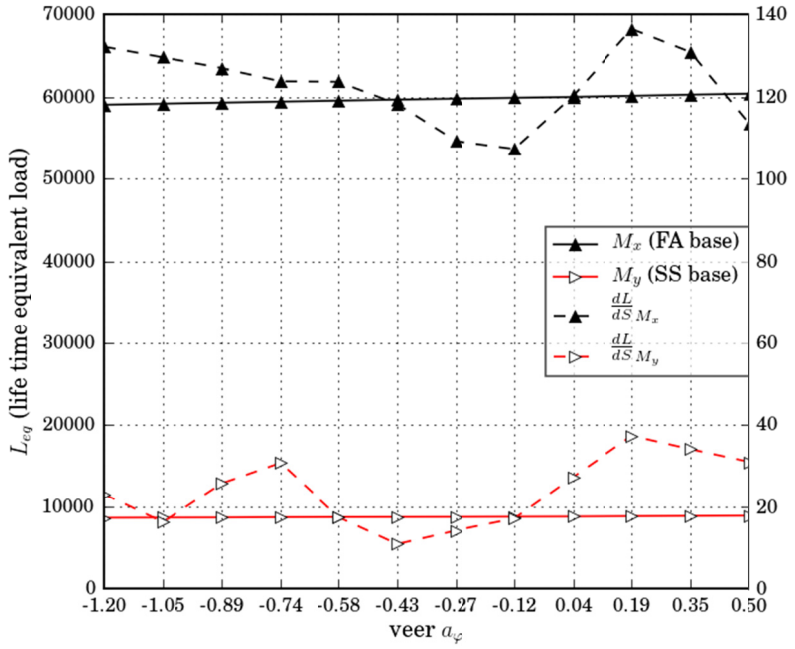

Figure 5.15: Load response function and its derivative for the tower bottom moments (tilt and sideways) as function of the veer parameter a_φ. In the plot tilt is abbreviated as FA, and tilt is abbreviated as SS.

The corresponding fatigue load pdf's and cdf's are shown in Figures 5.16-5.21.

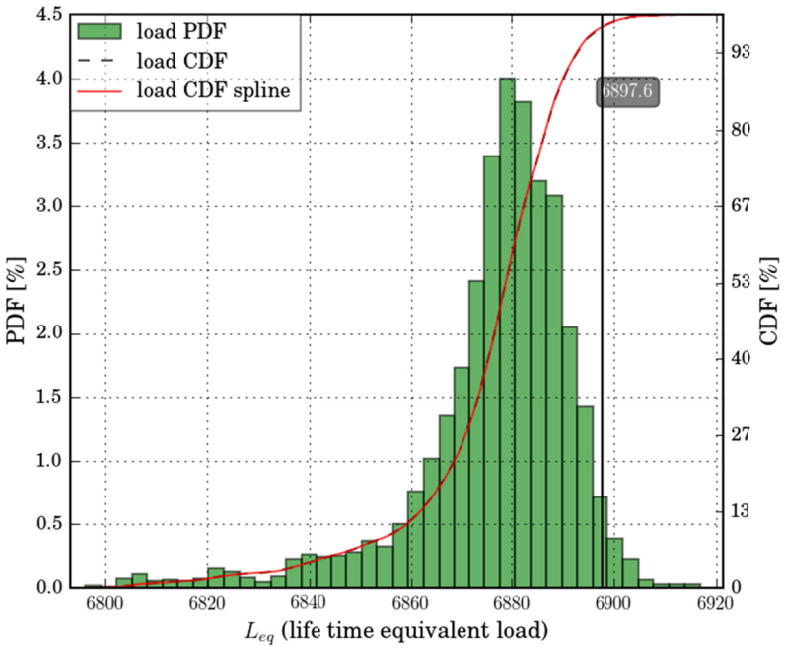

Figure 5.16: Load response pdf and cdf for the blade root flap moment.

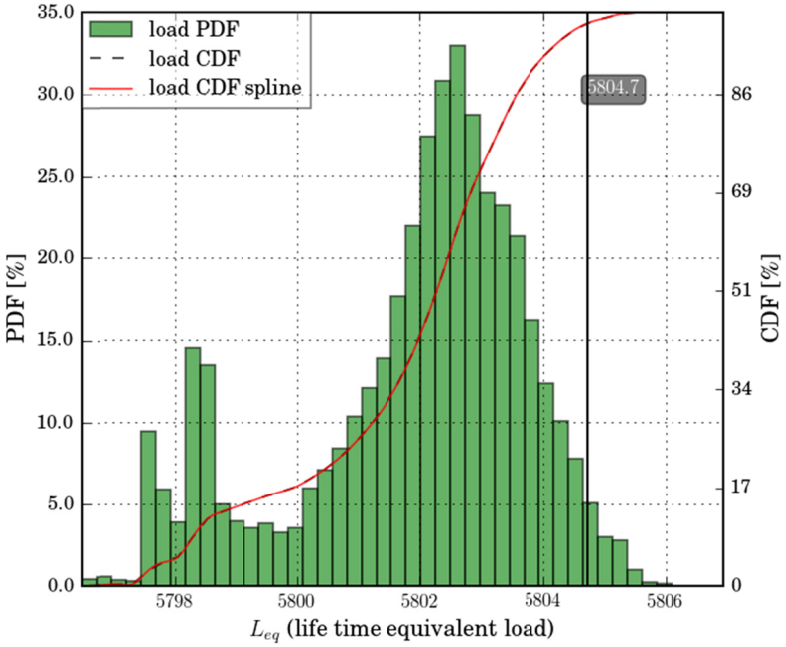

Figure 5.17: Load response pdf and cdf for the blade root edgewise moment.

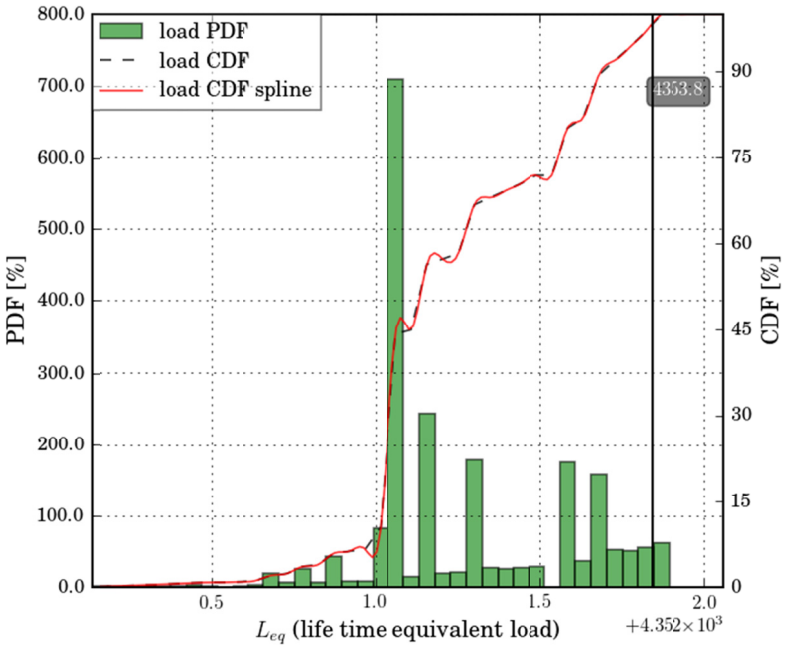

Figure 5.18: Load response pdf and cdf for the tower top sideways moment.

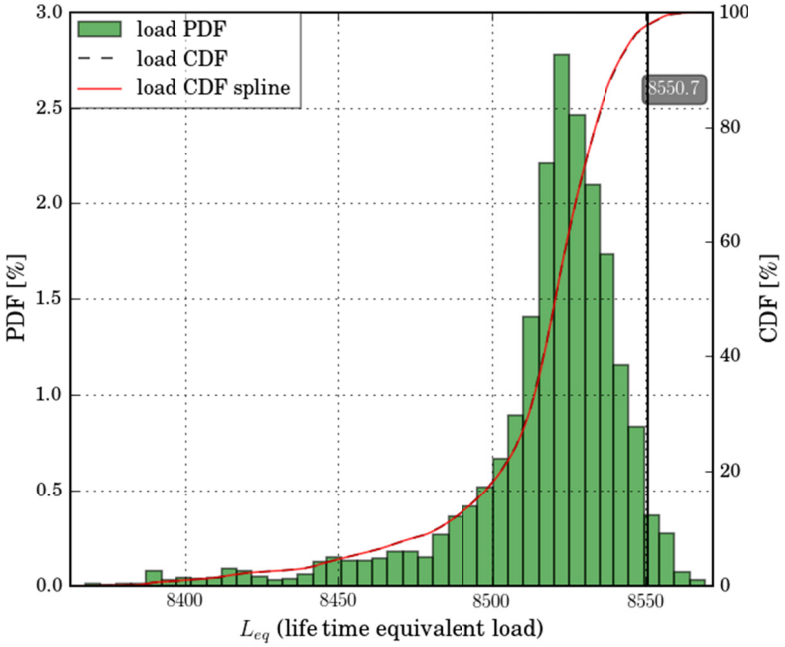

Figure 5.19: Load response pdf and cdf for the tower top tilt moment.

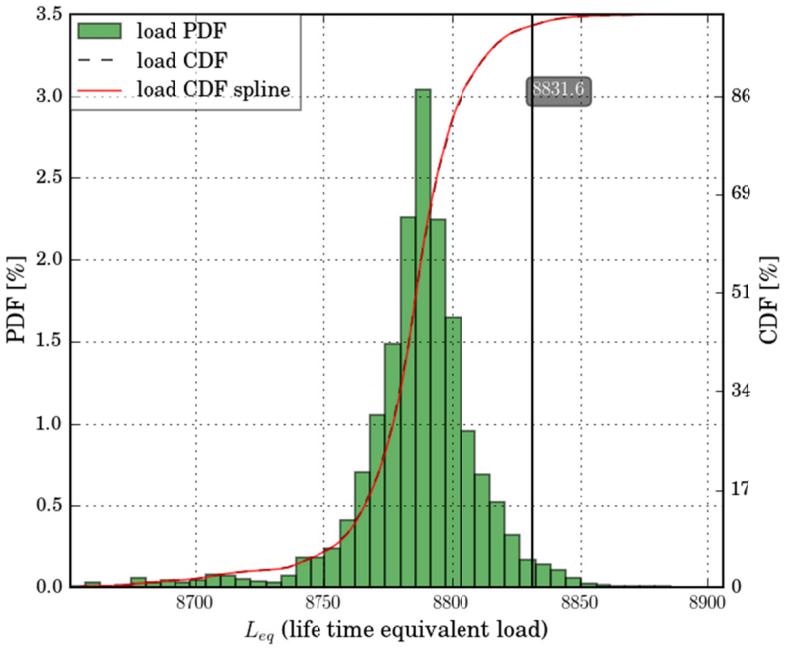

Figure 5.20: Load response pdf and cdf for the tower bottom sideways moment.

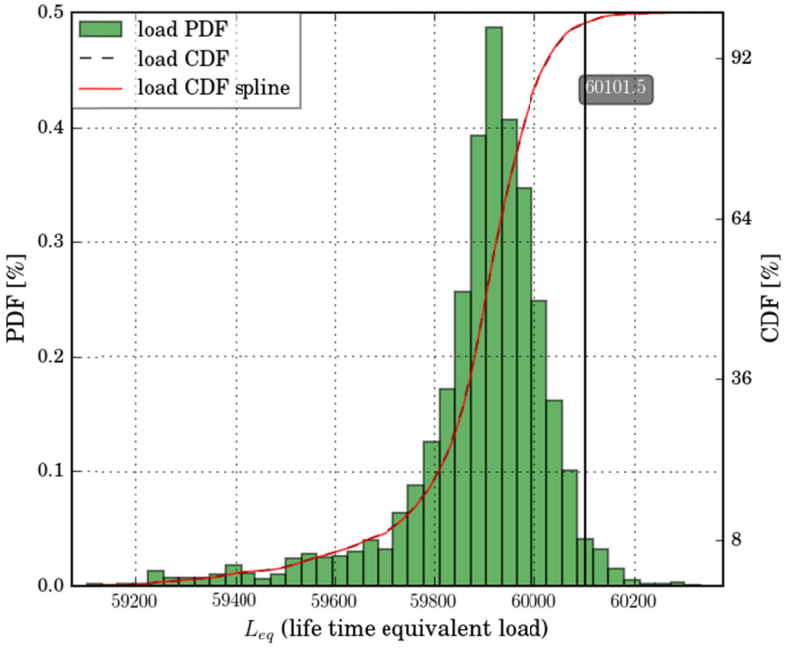

Figure 5.21: Load response pdf and cdf for the tower bottom tilt moment.

Adopting a 98% confidence level, the design veer parameter, $a_{\varphi d}$, for the investigated load types are summarized in Table 5.4.

Table 5.4: Design veer parameters as based on the Østerild marginal shear distribution.

Wind speed [m/s]	$a_{\varphi d}$ *(flap)*	$a_{\varphi d}$ *(edge)*	$a_{\varphi d}$ *(tower bottom tilt)*	$a_{\varphi d}$ *(tower bottom side)*	$a_{\varphi d}$ *(tower top tilt)*	$a_{\varphi d}$ *(tower top side)*
4	0.381	0.447	0.375	0.310	0.387	-0.650
6	0.384	-0.682	0.388	0.392	-0.054	-0.507
8	0.120	-1.080	0.284	-1.124	0.380	-0.526
10	0.228	-0.932	0.201	-0.975	0.464	-0.674
12	0.124	0.111	0.137	0.144	0.122	-0.176
14	0.085	0.088	0.088	-0.582	0.076	0.044
16	0.025	0.030	0.017	-0.206	0.024	0.009
18	0.057	0.060	0.058	-0.008	0.053	0.059
20	0.034	0.035	0.029	0.034	0.030	0.030
22	-	-0.871	0.131	0.223	0.069	-

	0.006					0.521
24	-0.016	-0.018	-0.012	0.094	-0.013	-0.027
26	-0.040	-0.048	-0.048	-0.040	-0.041	-0.042

5.7 Synthesis and recommendations

The basic design philosophy behind the IEC code, is to specify parameters characterizing the turbine

inflow conditions, which assures the structural integrity of a wind turbine structure up to the 98% quantile in *all* relevant load response pdf's. The determination of such input parameters is not a trivial problem - in fact it is not possible without approximations involving some engineering judgements. This is illustrated in Figure 5.22 showing the shear load response functions associated with a mean wind speed of 4m/s.

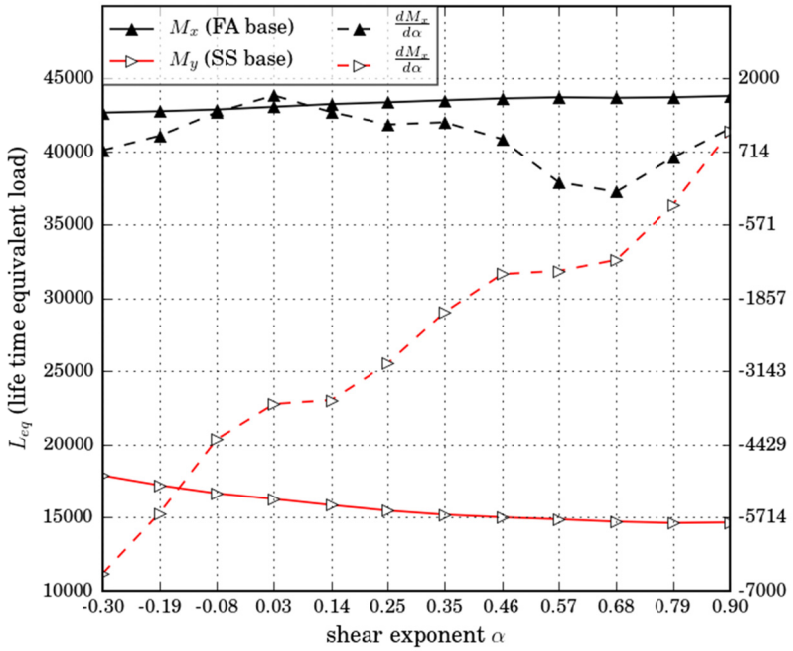

Figure 5.22: Load response function and its derivative for the tower bottom moments (tilt and sideways) as function of the shear exponent. In the plot tilt is abbreviated as FA, and tilt is abbreviated as SS.

Referring to Table 3 the shear exponent corresponding to the 98% quantile for the tower bottom tilt moment is 0.332, whereas the shear exponent corresponding to the 98% quantile for the tower bottom sideways moment is -0.205. In the present case, where both response curves are monotonic but with different sign of the gradient, it is not possible to define a design shear value matching the 98% quantile requirement for both sensors, and it is not even possible to take a conservative approach and define a design shear value assuring a probability of failure less than 2% for both sensors. This issue is further complicated when involving load sensors

associated with different turbine main components. Consequently, a full probabilistic analysis of the turbine structural integrity is in principle required.

A complete probabilistic analysis is not compatible with the IEC code philosophy, and therefore some engineering judgements are required to derive the requested code design specifications. First it is noted, that when a given turbine structural component has a *x*-*y* symmetric cross section (as e.g. the tower), then the sensor experiencing the highest load level (in the above example the M_x sensor) is the one dictating the design load values. Secondly, it is observed that, at least for the high end loading of the blade component, both blade flap and blade edgewise loading increase (in general) with increasing values of the investigated load parameters, thus allowing for a conservative design parameter definition for the blade loading. However, still mutual incompatibilities between components (i.e. blade and tower) exists regarding definition of overall turbine specific design values as e.g. resulting from some tower bottom response curves having their optimum at shear exponents of the order of 0.1, whereas the blade response curves takes their minimum values in this regime.

Based on the above considerations, the component/sensor specific design values for the shear and veer parameters given in Tables 5.3 and 5.4, respectively, are condensed into the recommendations given in Table 5.5, which is considered a possible balance between the individual sensor design values.

Table 5.5: Recommended Joint design shear and veer parameters for the Østerild site.

Wind speed [m/s]	Design shear (α)	Design veer ($a_{\varphi d}$)
4	0.332	0.447
6	0.615	0.392
8	0.410	0.380
10	0.372	0.464
12	0.577	0.144
14	0.376	0.088
16	0.524	0.030
18	0.367	0.060
20	0.494	0.035
22	0.331	0.223
24	0.355	0.094
26	0.365	-0.040

5.8 Conclusion

A computational efficient and versatile ”Monte Carlo” type of simulation is derived and used in combination with representative marginal distributions of shear and veer wind field characteristics to determine *design* shear/veer inflow fields as based on a 98% confidence level. This is achieved using numerically determined mapping functions based on the state-of-the-art aeroelastic code HAWC2 and taking advantage of a ”chasing back” feature associated with the proposed Monte Carlo technique. The suggested approach further leads to a straight forward

decomposition of input marginal distributions on the one side and requested transformations, formulated in terms of aeroelastic computations and suitable/arbitrary post processing of the results of such, on the other side, which is computationally economic when a suite of input pdf's is to be analyzed (e.g. pdf's from a variety of sites).

6. Formulation of New Load case setups and their impact on certification envelope

6.1 Probabilistic wind shear model (DLC1.1-1.2)

The probabilistic wind shear model discussed in Section 3.1 of this report is to be used in a future version of the IEC61400-1 standard for simulations under normal operating conditions (DLC1.1 – 1.2), for low-turbulence sites, IEC class C. Based on the findings from the study published in Dimitrov et al. 2014-1, the expected impact on the certification envelope is the following:

- Almost no impact on support structure loads
- Slightly reduced blade fatigue loads
- Slightly increased blade deflection towards the tower

6.2 Statistical extrapolation (DLC1.1)

A parametric study on the performance of different techniques for statistical extrapolation was carried out, comparing the 1-month recurrence extreme load values extrapolated from a few time series to the observed 1-month extreme load based on 30,000 simulations with 10-minute duration. The study involved a total of almost 80,000 individual extrapolations and aimed at determining the methods which are best suited for extrapolation of three different types of wind turbine loads: shaft torsion, blade root flapwise moment, and tower base side-to-side moment. The study resulted in a journal paper submission [27], and has the following conclusions:

- It is possible to obtain sufficiently good extrapolations with a number of extrapolation methods, however some methods such as the ACER method require larger amounts of data than what is currently practical for wind turbine design load assessment.
- 3-parameter distributions such as the 3-parameter Weibull or quadratic Gumbel [28] yield best results
- The convergence criterion defined in IEC61400-1, ed.3 (2010 amendment) seems to be too relaxed
- The Peaks-Over-Threshold method (POT) can potentially yield good results, however in comparison with the Global Maxima (GM) method it requires significantly more advanced analysis which can introduce additional uncertainties

Based on the results and experiences gained in this work, the method which is found most practical while sufficiently accurate for design purposes is the Global Maxima method combined with a 3-parameter extreme-value distribution such as Weibull or quadratic Gumbel, provided that a sufficiently large number of time series are used for extrapolation, e.g., at least 15 to 18 time series per wind speed.

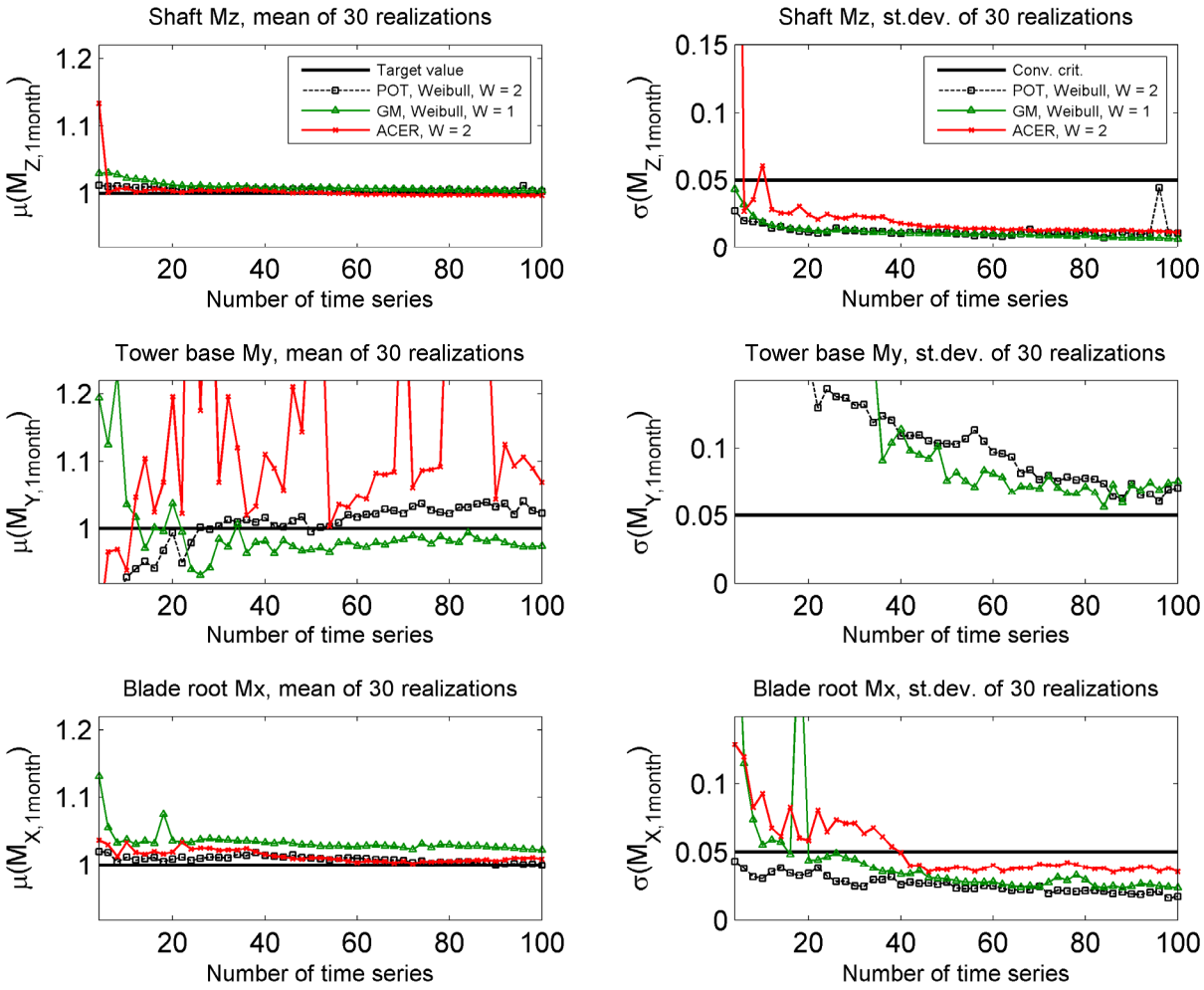

Figure 6.1: Statistics for the extrapolated 1-month extreme loads based on 30 samples for a selection of extrapolation methods. Left: mean of 30 extrapolations compared to the target value of 1; Right: standard deviation of 30 extrapolations compared to a convergence criterion of c.o.v. = 0.05. W = 2 means weighted least-squares fit based on confidence interval width, W = 1 means non-weighted fit. On the y-axis: μ denotes mean values, σ denotes standard deviation

6.3 Normal turbulence and extreme turbulence models

The studies discussed in section 3.3 of this report concluded that the parameters of the spectral models for turbulence have an influence on both fatigue and extreme loads. As an example, load simulations for load cases DLC1.1, 1.3, 3.1, 3.2, 4.1 and 4.2 (IEC 61400-1 ed.3 class 1A) are carried out on the NREL 5MW reference turbine. The extreme design loads for each load cases are then estimated using the procedures and safety factors recommended in IEC 61400-

- DLC 1.1: Statistical extrapolation to 50-year load, weighted by wind speed with the Rayleigh distribution, and multiplied with a safety factor of 1.25;
- DLC 1.3: Extreme turbulence model (ETM) with 50-year turbulence, the design load is calculated as the maximum from all simulations, multiplied by a factor of 1.35.

- DLC 3.2: Start-up combined with either Extreme Operating Gust (EOG) or Extreme Turbulence Model (ETM). The design loads are calculated as the average of all the maxima at the worst-case wind speed, multiplied by a safety factor of 1.35;
- DLC 4.2: Start-up combined with either Extreme Operating Gust (EOG) or Extreme Turbulence Model (ETM). The design loads are calculated as the average of all the maxima at the worst-case wind speed, multiplied by a safety factor of 1.35

Figures 6.2 to 6.6 illustrate the expected effect of changing turbulence models on the extreme loads on different turbine components. The main observations are that:

1) Using modified Mann model parameters which match the turbulence spectra to observations over flat terrain can result in slightly reduced extreme design loads on blades and yaw bearing, and slightly increased tower-base extreme design loads
2) Using an extreme turbulence model instead of extreme operating gust in DLC 3.2 and 4.2 (an approach which is currently considered for inclusion in IEC 61400-1, ed.4) will lead to increased design loads for a number of components, an effect especially noticeable on blade edgewise moments (Fig. 6.3) and tower base side-to-side moment (Fig. 6.6).

Damage-equivalent fatigue loads are calculated for DLC1.1, 3.1 and 3.2, and the effect of turbulence modelling on fatigue life is shown on figures 6.7 to 6.11. For the fatigue loads, the conclusion is that using modified Mann model parameters can result in a small decrease of fatigue design loads for some components, while other components are unaffected.

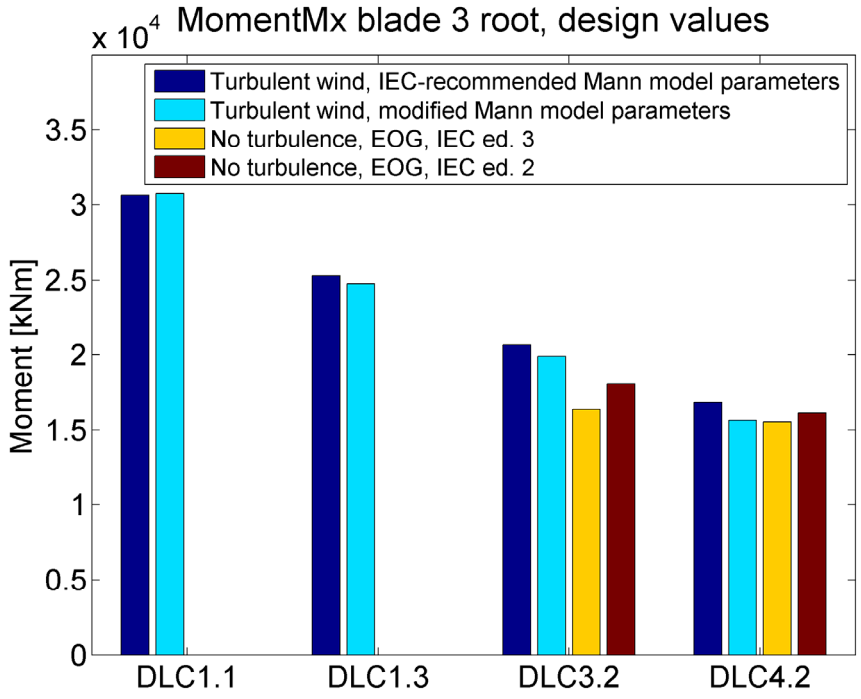

Figure 6.2: Effect of different wind modelling approaches on design values for blade root out-of-plane (flapwise) moment

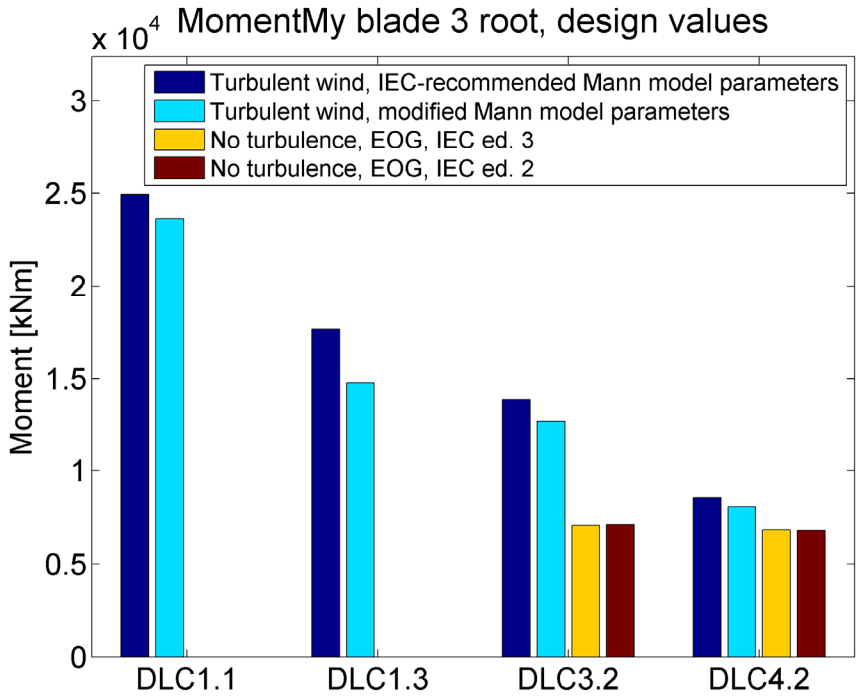

Figure 6.3: Effect of different wind modelling approaches on design values for blade root in-plane (edgewise) moment

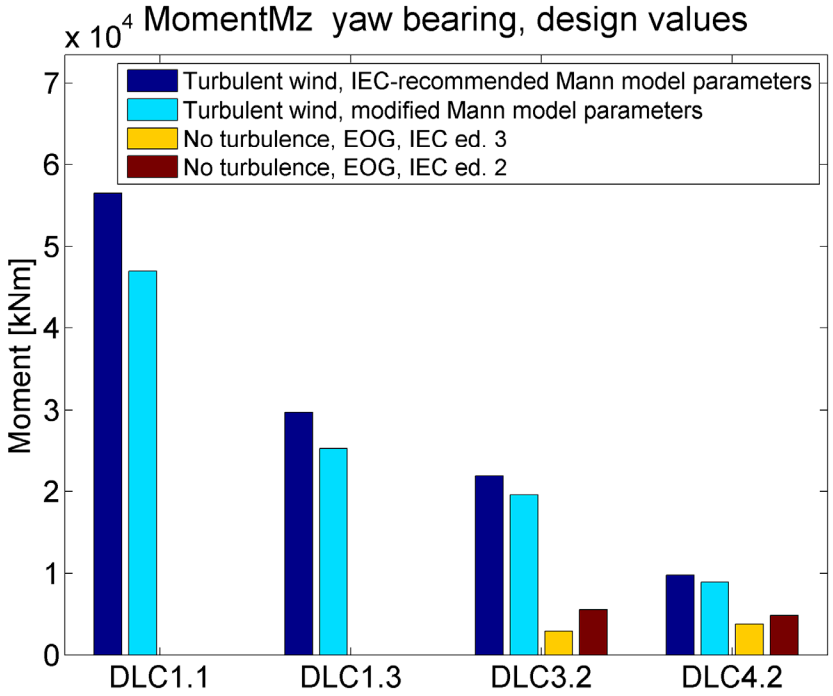

Figure 6.4: Effect of different wind modelling approaches on design values for yaw moment

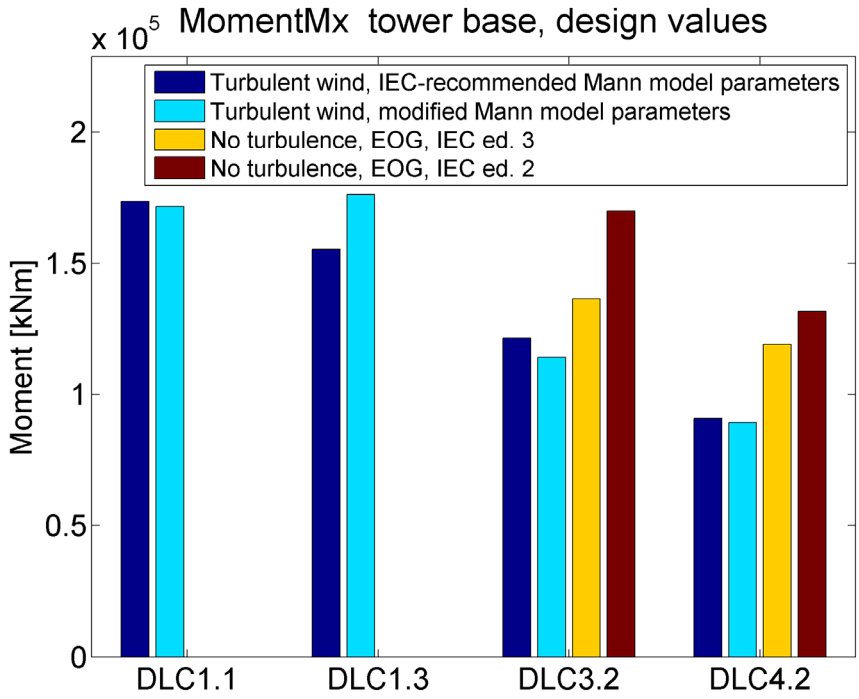

Figure 6.5: Effect of different wind modelling approaches on design values for tower base for-aft moment

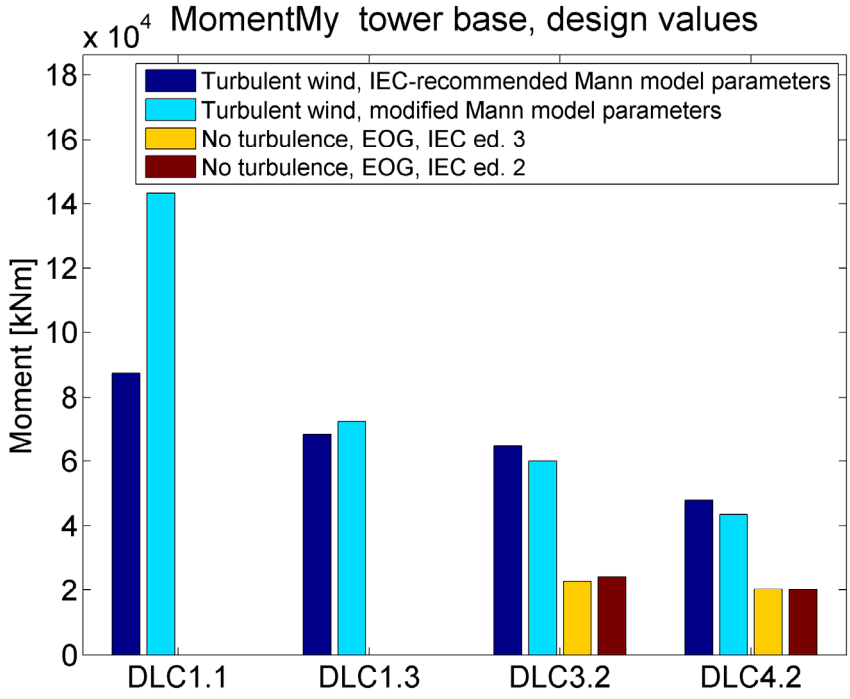

Figure 6.6: Effect of different wind modelling approaches on design values for tower base side-to-side moment

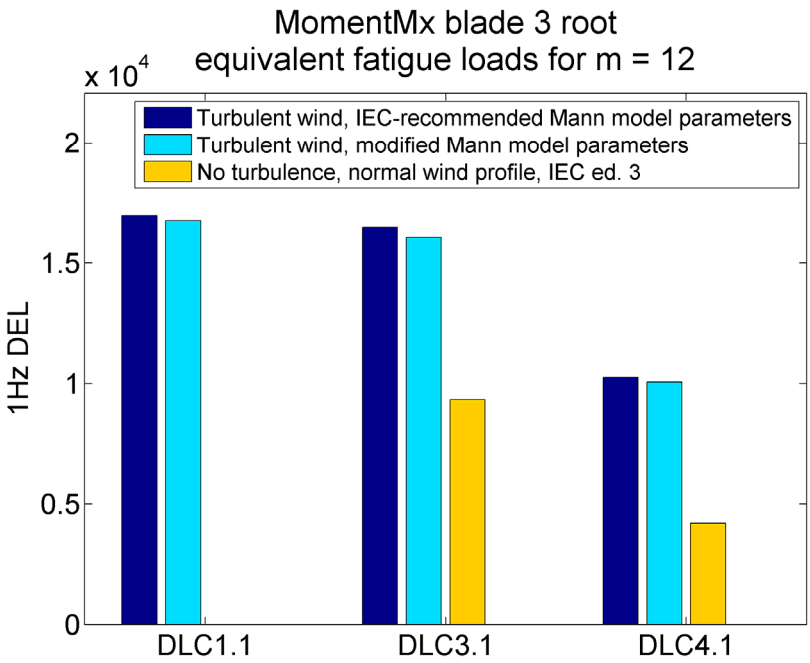

Figure 6.7: Effect of different wind modelling approaches on design values for blade root out-of-plane (flapwise) damage-equivalent fatigue moment

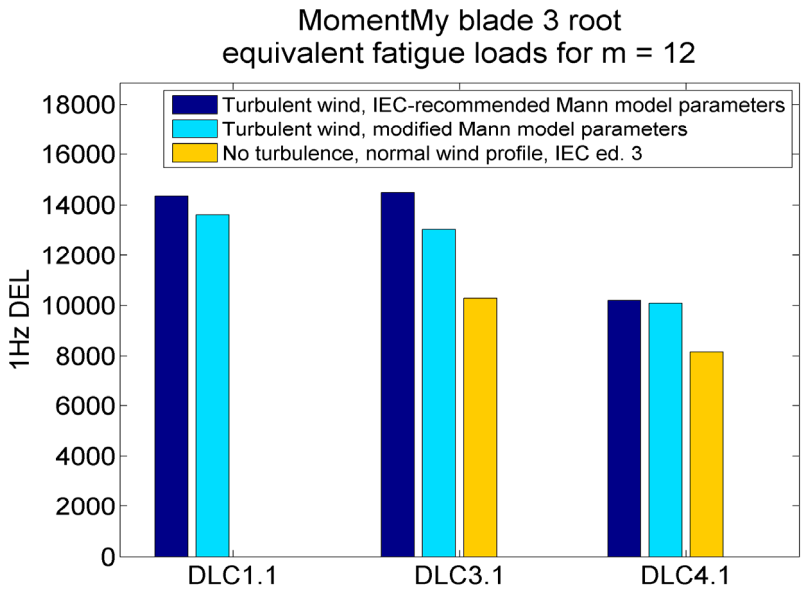

Figure 6.8: Effect of different wind modelling approaches on design values for blade root in-plane (edgewise) damage-equivalent fatigue moment

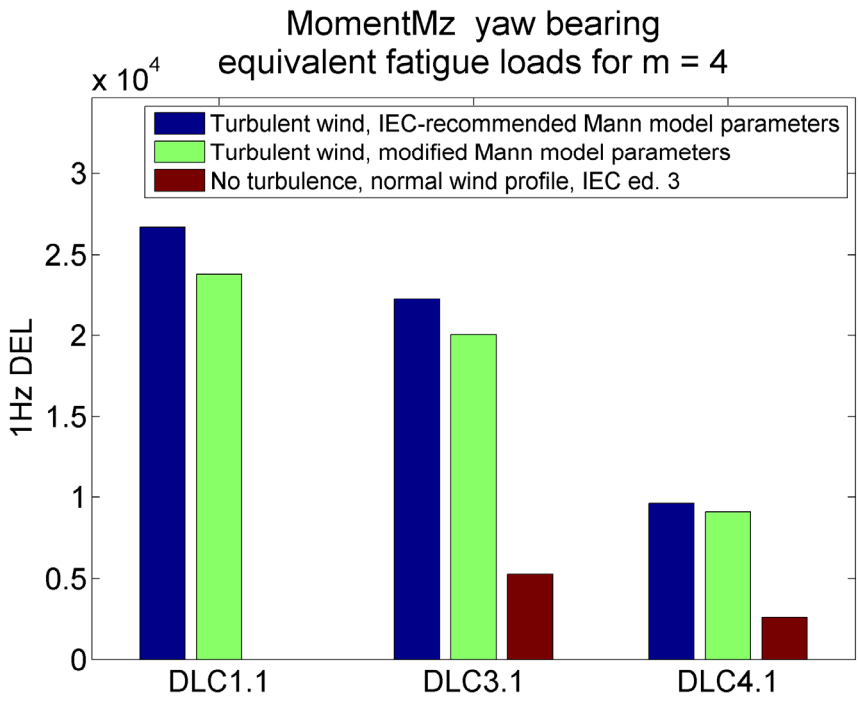

Figure 6.9: Effect of different wind modelling approaches on yaw bearing damage-equivalent fatigue moment

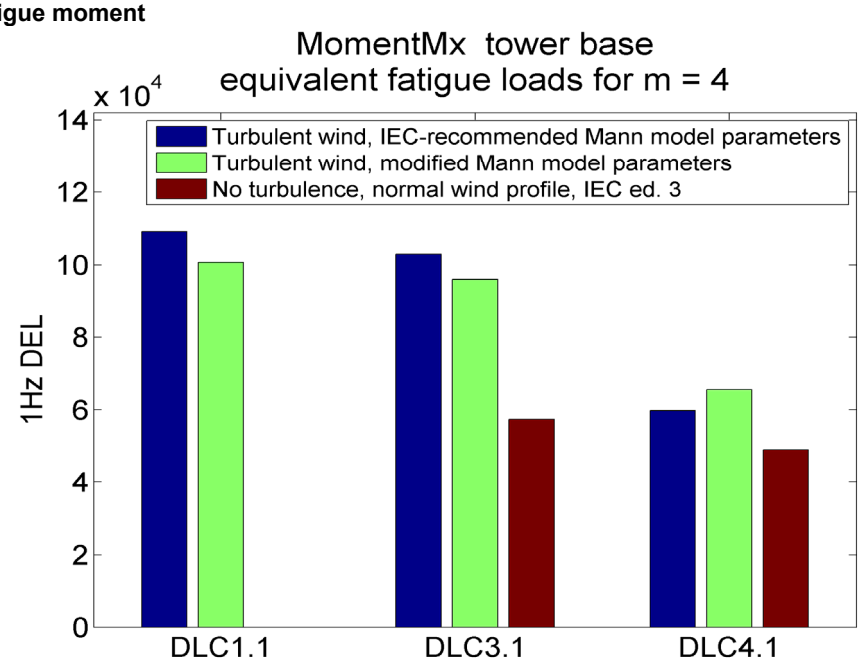

Figure 6.10: Effect of different wind modelling approaches on design values for tower base for-aft damage-equivalent fatigue moment

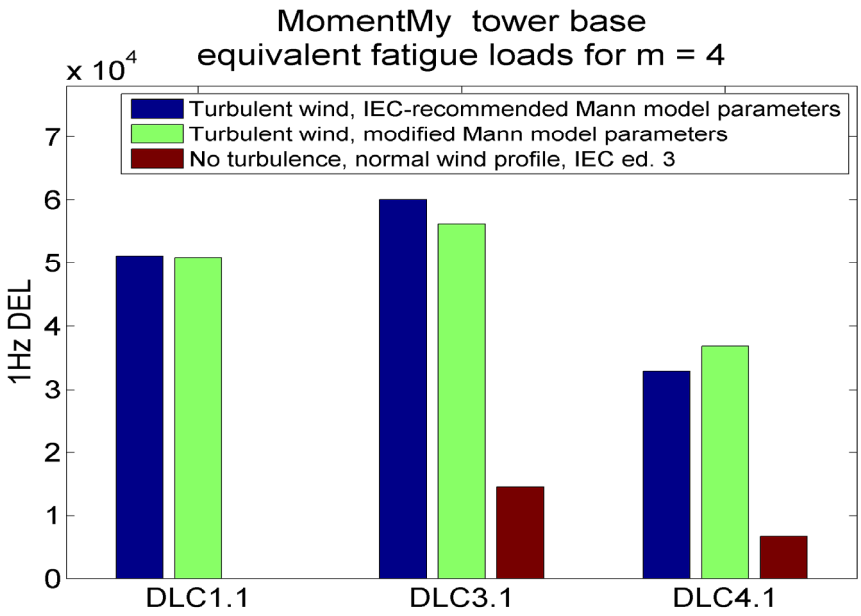

Figure 6.11: Effect of different wind modelling approaches on design values for tower base side-to-side damage-equivalent fatigue moment

7. Evaluation of Partial Safety Factors for Design

The objective of this chapter is to describe the background for the material partial safety factors recommended in CD IEC 61400-1 ed. 4 and to illustrate the applications to tall wind turbines with large rotors. A detailed description can be found in Sørensen & Toft [29]. Both extreme loads and fatigue loads are considered.

In section 7.1 the required reliability level for design of wind turbine structural components is discussed and a target reliability level is derived. In section 7.2 three basic models for calculating the design value of the load bearing capacity is presented. Next, reliability-based calibration of material partial safety factors is described in the following cases: DLC 1.1 and 6.1 with extreme load; fatigue of welded steel details; component / consequence class partial safety factor γ_c. Sørensen & Toft [29] also describes calibration of safety factors related to DLC 2.1 and 2.2 with extreme load and faults. Section 7.3 describes how the uncertainty level for the loads influences the load partial safety factors. Finally section 7.4 describes illustrative examples for tall wind turbines with large rotors.

7.1 Target reliability level for design of wind turbine structural components

The probability of failure of a structural component is generally linked to a limit state equation modelling the failure event and stochastic variables modelling the uncertain parameters. The reliability is often expressed by the reliability index β which is related to the probability of failure, P_F as shown in the Table 7.1.

Table 7.1. Relationship between reliability index, β and probability of failure, P_F.

P_F	10^{-2}	10^{-3}	10^{-4}	10^{-5}	10^{-6}	10^{-7}
β	2.3	3.1	3.7	4.3	4.7	5.2

The target reliability level can be given in terms of a maximum annual probability of failures (i.e. reference time equal to 1 year) or a maximum lifetime probability of failure (i.e. for wind turbines a reference time equal to 20 – 25 years). For civil and structural engineering standards / codes of practice where failure can imply risk of loss of human lives target reliabilities are generally given based on annual probabilities. The optimal reliability level can be found by considering representative cost-benefit based optimization problems where the life-cycle expected cost of energy is minimized with appropriate constraints related to acceptable risks of loss of human lives, e.g. based on LQI (Life Quality Index) principles.

Examples of reliability levels required (implicitly) in some relevant standards / codes (for normal consequence / reliability class) are:

- Building codes (in Europe): Eurocode EN1990 [30]:
  - Extreme load: annual: $P_F = 10^{-6}$ (β = 4.7) or lifetime (50 years): $P_F = 10^{-4}$ (β = 3.8)

  - Fatigue: design life (50 years): P_F = 0.06 – 10^{-4} (β = 1.5 - 3.8) depending on possibility for inspections and criticality
- Fixed steel offshore structures, see e.g. ISO 19902 [31]:
  - manned:

    annual $P_F \sim 3\ 10^{-5}$ or β = 4.0
  - For structures that are unmanned or evacuated in severe storms and where other consequences of failure are not very significant: annual $P_F \sim 5\ 10^{-4}$ or β = 3.3
- JCSS (Joint Committee on Structural Safety) recommends reliability requirements based on annual failure probabilities for structural systems for ultimate limit states, see Table 7.2. These are based on optimization procedures and on the assumption that for almost all engineering facilities the only reasonable reconstruction policy is systematic rebuilding or repair.

Table 7.2. Target annual reliability index and probability of failure according to JCSS (2002).

Relative costs of safety measures	Consequences of failure		
	Minor / Some	Moderate	Large
High cost of safety measures	$\beta^t = 3.1, P_F = 10^{-3}$	$\beta^t = 3.3, P_F = 5 \cdot 10^{-4}$	$\beta^t = 3.7, P_F = 10^{-4}$
Moderate cost of safety measures	$\beta^t = 3.7, P_F = 10^{-4}$	$\beta^t = 4.2, P_F = 10^{-5}$	$\beta^t = 4.4, P_F = 5 \cdot 10^{-6}$
Low cost of safety measures	$\beta^t = 4.2, P_F = 10^{-5}$	$\beta^t = 4.4, P_F = 5 \cdot 10^{-6}$	$\beta^t = 4.7, P_F = 10^{-6}$

It should be noted that the β-values (and the corresponding failure probabilities) are formal / notional numbers, intended primarily as a tool for developing consistent design rules, rather than giving a description of the structural failure frequency. E.g. the effect of human errors is not included.

For wind turbines the risk of loss of human lives in case of failure of a structural element is generally very small. Further, it can be assumed that wind turbines are systematically reconstructed in case of collapse or end of lifetime. In that case also target reliabilities based on annual probabilities should be used, see JCSS [32]. The optimal reliability level can be found by considering representative cost-benefit based optimization problems where the life-cycle expected cost of energy is minimized.

It is assumed that for wind turbines:

- A systematic reconstruction policy is used (a new wind turbine is erected in case of failure or expiry of lifetime).
- Consequences of a failure are only economic (no fatalities and no pollution).
- Cost of energy is important which implies that the relative cost of safety measures can be considered large (material cost savings are important).
- Wind turbines are designed to a certain wind turbine class, i.e. not all wind turbines are 'designed to the limit'.

Based on these considerations the target reliability level corresponding to a minimum annual probability of failure is recommended to be:

$$P_f = 5 \cdot 10^{-4}$$

corresponding to an annual reliability index equal to 3.3. This reliability level corresponds to minor / moderate consequences of failure and moderate / high cost of safety measure. It is noted that this reliability level corresponds to the reliability level for offshore structures that are unmanned or evacuated in severe storms and where other consequences of failure are not very significant.

7.2 Calibration of partial safety factors

A reliability based calibration of the material partial safety factors have been performed for selected, important design load cases (DLC):

- Design Load Case 1.1
- Design Load Case 2.1 and 2.2
- Design Load Case 6.1
- Design Load Cases with Fatigue

Further, a reliability-based assessment of modification factors for different safety classes has been performed.

The resistance / load bearing capacity of structural elements are assumed to follow the same three models as in the Eurocodes, EN 1990 (2002) and in ISO 2394 [33]:

- Model 1: first, partial safety factors accounting for uncertainties of the strength and stiffness parameters are used to obtain design values of strength and stiffness parameters and the design value of the resistance model is determined. Next, this value is divided by a partial safety factor accounting for model uncertainty to obtain the design value of the load bearing capacity.
- Model 2: first, the value of the resistance model is calculated using characteristic values of the strength and stiffness parameters. Next, this value is divided by a partial safety factor accounting for the total uncertainty of the resistance model (model uncertainty and uncertainty of strength and stiffness parameters) to obtain the design value of the load bearing capacity.
- Model 3: the characteristic value of the load bearing capacity is obtained e.g. based on tests and this value is divided by a partial safety factor accounting for the uncertainty of the load bearing capacity to obtain the design value of the load bearing capacity.

A generic limit state equation is formulated with representative uncertainties for strength parameters and model uncertainties. Further, the model also accounts for bias (hidden safety) in the calculation models for the load bearing capacity, see Sørensen & Toft (2014) for details.

7.2.1 DLC 1.1 and 6.1 with extreme load

This section describes the calibration of material partial safety factors for DLC 1.1 (wind turbine in operation) and 6.1 (wind turbine parked) with extreme loads.

The calibrations are performed assuming that there is

- no bias (hidden safety) in calculation of load effects
- no bias (hidden safety) in calculation of load bearing capacities
- no scale effects, time duration effects, etc.

These effects are accounted for afterwards.

The following generic limit state equation for the extreme load effect in operation (DLC 1.1) or standstill (DLC 6.1) is used (without permanent loads)

$$g = z\,\delta\,R - X_{dyn} X_{\exp} X_{aero} X_{str} L \tag{7.1}$$

where

z	design parameter, e.g. cross-sectional area
δ	model uncertainty load bearing capacity model
R	uncertainty in dominating strength parameter
X_{dyn}	uncertainty related to modeling of the dynamic response, including uncertainty in damping ratios and eigenfrequencies
X_{exp}	uncertainty related to the modeling of the exposure (site assessment) - such as the terrain roughness and the landscape topography
X_{aero}	uncertainty in assessment of lift and drag coefficients and additionally utilization of BEM, dynamic stall models, etc.
X_{str}	uncertainty related to the computation of the load-effects given external load
L	uncertainty related to the extreme load-effect due to wind loads

The ‘representative’ stochastic model in Table 7.3 is used for modelling the uncertainties.

Table 7.3. Stochastic models for physical, model and statistical uncertainties in DLC 1.1 and 6.1.

Variable	Distribution	Mean	COV	Quantile	Comment
R	Lognormal	-	V_R	5%	Strength
δ	Lognormal	-	V_δ	Mean	Model uncertainty
L – DLC 1.1	Weibull	-	0.15	0.98	Annual maximum load effect obtained by load extrapolation
L – DLC 6.1	Gumbel	-	0.2	0.98	Annual maximum wind pressure – European wind conditions
X_{dyn}	Lognormal	1.00	0.05	Mean	
X_{exp}	Lognormal	1.00	0.15	Mean	
X_{aero}	Gumbel	1.00	0.10	Mean	
X_{str}	Lognormal	1.00	0.03	Mean	

The corresponding design equation is written:

$$\frac{z\,R_k}{\gamma_R} - \gamma_f L_k \geq 0 \qquad (7.2)$$

where

R_k characteristic value of load bearing capacity

L_k characteristic value of variable load

γ_M partial safety factor for load bearing capacity

γ_f partial safety factor for load effect

A load partial safety factor equal to γ_f =1.35 is used, and the material partial safety factors are calibrated such that the reliability level becomes equal to the target reliability level specified above. Based on the calibrated partial safety factors the following values are included in the draft CD IEC 61400-1 ed. 4 (2014) standard where the total material partial safety factor generally is written as $\gamma_M = \frac{\gamma_m \gamma_\delta}{b}$ where γ_m depends on the uncertainty of the material strength parameters, γ_δ depends on the model uncertainty and *b* is a possible bias:

γ_m = 1.0, i.e. independent on the uncertainty of the material parameters.

Table 7.4. Material partial safety factor for model uncertainty.

Coefficient of variation for model uncertainty for resistance model	0 %	5 %	10 %	15 %	20 %
γ_δ	1.15	1.20	1.25	1.35	1.45

Examples are given in section 7.4 on material safety factors derived on the basis of the above calibration. Generally, the safety factors for design of structural elements are of the same level as those obtained from IEC 61400-1 ed. 3 (2005), see also comments in section 7.4.

7.2.2 Fatigue of welded details in steel structures

This section considers calibration of partial safety factors for welded details in steel structures. Basically a linear SN-curves is considered with the SN relation written:

$$N = K\left(\Delta\sigma\right)^{-m} \qquad -(7.3)$$

where N is the number of stress cycles to failure with constant stress ranges $\Delta\sigma$. K and m are dependent on the fatigue critical detail. In the reliability-based calibrations also bi-linear SN-curves are used.

The probability of failure in year *t* given survival up to year *t* is estimated with a limit state equation based on SN-curves, Miner's rule for linear accumulation of fatigue damage and by introducing stochastic variables accounting for uncertainties in fatigue loading and strength. The

stochastic models shown in Table 7.5 are considered as representative for a fatigue sensitive welded steel detail. It is assumed that the design lifetime is T_L = 25 year.

For deterministic design partial safety factors are introduced:

- γ_f : a fatigue load partial safety factor multiplied to the fatigue stress ranges obtained by e.g. Rainflow counting.
- γ_m : a fatigue strength partial safety factor. The design value of the fatigue strength is obtained by dividing the characteristic fatigue strength by γ_m.

Table 7.5. Stochastic model.

Variable	Distribution	Expected value	Standard deviation / Coefficient Of Variation	Comment
Δ	N	1	COV_Δ = 0.30	Model uncertainty Miner's rule
X_{Wind}	LN	1	COV_{Wind}	Model uncertainty wind load
X_{SCF}	LN	1	COV_{SCF}	Model uncertainty stress concentration factor
m_1	D	3		Slope SN curve
$\log K_1$	N	determined from $\Delta\sigma_D$	$\sigma_{\log K_1}$ = 0.2	Parameter SN curve
m_2	D	5		Slope SN curve
$\log K_2$	N	determined from $\Delta\sigma_D$	$\sigma_{\log K_2}$ = 0.2	Parameter SN curve
$\Delta\sigma_F$	D	71 MPa		Fatigue strength
$\log K_1$ and $\log K_2$ are fully correlated				

The required product of the partial safety factors $\gamma_f\gamma_m$ is obtained by reliability-based calibration using the stochastic model in Table 7.5. The results which are included in the draft CD IEC 61400-1 ed. 4 (2014) standard are: γ_m = 1.25

Table 7.6. Recommended partial safety factor for fatigue stress ranges, γ_f .

Coefficient of variation, COV_{load}	0-5 %	5-10 %	10-15 %	15-20 %	20-25 %	25-30 %
γ_f	0.85	0.90	0.95	1.00	1.10	1.20

Typically the coefficient of variation, COV_{load} will be 15-20% implying $\gamma_f\gamma_m$ =1.25 which is at the same level as in IEC 61400-1 ed. 3 (2005).

7.2.3 Reliability analysis of influence of component class partial safety factor γ_c

This section describes reliability based investigations related to the consequence of failure factor γ_C which is introduced to distinguish between:

- Component class 1: used for "fail-safe" structural components whose failure does not result in the failure of a major part of a wind turbine, for example replaceable bearings with monitoring. Component class 1 is considered to correspond to low consequence of failure.
- Component class 2: used for "non fail-safe" structural components whose failures may lead to the failure of a major part of a wind turbine. Component class 2 is considered to correspond to middle consequence of failure.
- Component class 3: used for “non fail-safe” mechanical components that link actuators and brakes to main structural components for the purpose of implementing non-redundant wind turbine protection functions. Component class 3 is considered to correspond to high consequence of failure.

A reliability-based calibration shows that the following consequence of failure factor γ_C multiplied to the load partial safety factor can be used with the following values for different consequence / component classes:

Component class 1 - low consequence:	γ_C =0.9
Component class 2 - middle consequence:	γ_C =1.0
Component class 3 - high consequence:	γ_C =1.2

corresponding to a difference in probability of failure equal to a factor 10 between ‘low’ and ‘middle’ and between ‘middle’ and ‘high’.

Compared to the corresponding factors in IEC 61400-1 ed. 3 (2005) γ_C for component class 3 has been decreased from 1.3 to 1.2.

7.3 Modification of partial safety factors when ‘better’ models/information are available

In the tables below are given some general examples of sources of uncertainties concerning loads, which are dependent on the “quality” of the models or information available, see also Sørensen & Toft (2014). The “quality” of the model/information would affect the definition of the stochastic variables (mainly the COV) and, hence, the safety factor can be re-calibrated as described above.

For uncertainty modelling of wind, as an example, two additional columns are included, showing a Worst case and a Best case scenario. The worst scenario implies larger uncertainties, so the corresponding stochastic variables would have a larger COV, leading to larger safety factors. The best scenario implies less uncertainties, so the corresponding stochastic variables would have a smaller COV (assuming same distribution), leading to smaller safety factors. Of course, in practice, there could be intermediate scenarios.

Table 7.7 Uncertainty related to modelling of wind.

Uncertainty sources	**Worst scenario**	**Best scenario**
Intra-annual variations	Data not covering all	Data from all seasons and

(seasonal variations) and inter-annual variations, directional variations	seasons and directions	directions and along several years
Quality of anemometers	Non Calibrated, standard cup anemometer	Calibrated 1st class or sonic anemometers
Quality of met mast mounting	Anemos at mid height, with bad mounting	Anemos at the top, with good mounting
Number of measurements at met mast	Less than 1 year	Several years
MCP	No MCP applied	MCP with more than 30 years at reference mast
Horizontal extrapolation	Curves lines more than 20m. Unkown Roughness Complex terrain	Curves lines less than 10m. Low Roughness Flat terrain
Vertical extrapolation	Simple exponential model. Measurements below hub height.	Measurements at several heights within rotor size
Wind field and turbulence model	Use a basic standard wind model (Kaimal, Mann)	Detailed characterization of spectra and coherence, based on measurements
Wake models	Effective turbulence model	DWM or CFD analysis
Determination of Long-term wind speeds	EWS2 method ($V_{ref}=5\cdot V_{ave}$)	Extrapolation based on several years of measurements

Table 7.8 Uncertainty related to modelling of aerodynamics.

Uncertainty sources	Worst scenario	Best scenario
Blade geometric properties (roughness, airfoil shape)	Poor manufacturing quality control	Very good manufacturing quality control
Aerodynamic coefficients	Based on simple fluid dynamics formulation	Based on measurements at different Re and several aoa.
Rotor aerodynamic models	Simple BEM model	Complete CFD

Table 7.10 Uncertainty related to modelling of structural dynamics.

Uncertainty sources	Worst scenario	Best scenario
Structural properties (masses, stiffness's, frequencies…)	Data estimated from design. Poor manufacturing quality control	Real data measured. Very good manufacturing quality control
Structural models (degrees of freedom, coupling of modes…)	Modal synthesis with simple beam models, few dof	Complete 3D FEM

Table 7.11 Uncertainty related to modelling of wind turbine actuation systems.

Uncertainty sources	Worst scenario	Best scenario
Control parameters	Predefined parameters, from simulation environment	Parameters as in field
Control algorithms	Simplified algorithms, similar to PLC (but not the same)	Algorithms exactly as in field
Actuation systems models	1st order system	Complete validated system model
Actuation systems properties	Estimated from design	Measured on real equipment

Table 7.11 Uncertainty related to modelling of fatigue.

Uncertainty sources	Worst scenario	Best scenario
Number and chronology of events (Cycle history)	Consider estimated number of events and chronology	Consider actual number of events and chronology
Simplified equivalent damage loads (e.g.- Miner's rule)	Consider only Damage Equivalent Load, using Miner's Rule	Consider full time series for damage evaluation

Table 7.12 Uncertainty related to modelling of extreme load response.

Uncertainty sources	Worst scenario	Best scenario
Probability of load cases	Probability of wind, turbine response (e.g.- alignment, azimuth) and eventual failures	Use actual data about recurrence of events
Load response distribution	Load response estimated from characteristic load and some assumptions (extrapolation model)	Actual distribution obtained from complete 50 year simulation

Above and in Sørensen & Toft [29], the calibration of partial safety factors for fatigue is described. The fatigue load partial safety factor is dependent on the uncertainty of the fatigue stresses which is assumed to have two contributions:

- Uncertainty related to estimation of the fatigue stress given the fatigue load – modelled by a stochastic variable X_{wind} with coefficient of variation COV_{Wind}
- Uncertainty related to the fatigue load – modelled by a stochastic variable X_{SCF} with coefficient of variation COV_{SCF}

The total coefficient of variation of the fatigue load becomes $COV_{load} = \sqrt{COV_{Wind}^2 + COV_{SCF}^2}$.

The uncertainties related to wind load assessment, X_{wind} in relation to fatigue can be divided in:

- modeling of the exposure (site assessment) – incl. assessment of terrain roughness, landscape topography, annual mean wind speed, turbulence intensity, density, shear and veer
- modeling of the dynamic response, including uncertainty in damping ratios and eigenfrequencies
- assessment of lift and drag coefficients and additionally utilization of BEM, dynamic stall models, etc.

Table 7.13 shows examples of how to model the uncertainty related to X_{wind} . The contribution of the different sources of uncertainties to the total X_{wind} could be evaluated with sensitivity analysis. X_{wind} could then be defined as a response surface dependent on several stochastic variables, each of them accounting for a specific effect described in Table 7.13. In Sørensen & Toft (2014) examples are shown how to model the uncertainty related to X_{SCF} .

Table 7.13. Examples of the total coefficient of variation for fatigue load COV_{Wind} .

COV_{Wind}	Uncertainty is assessment of fatigue wind load
0.10-0.15	*Site assessment:* • More than 2 years of climatic data, corrected with MCP techniques. • Wind measurements above and below wind turbine hub height. • Flat terrain with low roughness *Dynamic response:* • Structural dynamic effects through modal analysis, with at least 4 modes considered for blade and tower. • Mass and stiffness properties defined with FEM and validated with real scale specimens. • Eigenvalues and damping validated with real scale tests. *Aerodynamic coefficients:* • Airfoil data experimentally validated in wind tunnel at different Re numbers • Airfoil data including 3D effects • Attached flow in all operating regimes • BEM, including Dynamic stall and Tip and hub loss included • Dynamic wake inflow model • Quality control of shape of manufactured blades
0.15-0.20	*Site assessment:* • Minimum 1 year of climatic data.

	• Wind measurements at hub height and below. • Non-complex site with medium roughness. *Dynamic response:* • Structural dynamic effects through modal analysis, with 2 modes considered for blade and tower. • Mass and stiffness properties defined with FEM but not validated with real scale specimens. • Eigenvalues and damping not validated with real scale tests. *Aerodynamic coefficients:* • Airfoil data based on CFD, but not measured in wind tunnel. • 3D effects not included in airfoil data • Attached flow in all operating regimes • BEM, but not including dynamic stall effects nor tip and hub losses • Static wake inflow model
0.20-0.25	*Site assessment:* • Less than 1 year of data, not corrected with MCP techniques Wind measurements below hub height. • Complex terrain. *Dynamic response:* • Structural dynamic effects not considered *Aerodynamic coefficients:* • Airfoil data based on similar airfoils or for a single Re number. • 3D effects not included in airfoil data • Stall flow in relevant operating regimes • BEM, but not including dynamic stall effects nor tip and hub losses • No model for wake effects • Dirt and erosion on blades

7.4 Examples for tall wind turbines with large rotors

Design values of loads and resistances are obtained using characteristic values and partial safety factors according to IEC 61400-1. Characteristic values are generally defined as 5% quantiles for resistances and loads with 50 year return period.

In the following examples it is shown how to derive the material partial safety factors for specific applications based on Table 7.4.

For structural steel components with yielding failure criteria the yield strength coefficient of variation is typically V_R =0.05, the model uncertainty coefficient of variation is typically V_δ =0.05, and the bias b =1.1 for ductile failure with extra load bearing capacity. This implies $\gamma_R \approx$ 1.20 and taking into account the bias the resulting partial safety factor becomes γ_M = 1.20 / 1.1 ~ 1.1.

For structural steel components where the buckling failure criteria is design driving, the yield strength coefficient of variation is typically V_R =0.05, the model uncertainty coefficient of

variation is typically V_δ =0.13, and the bias is b = 1 / 0.85. This implies $\gamma_R \approx 1.31$ and taking into account the bias the resulting partial safety factor becomes γ_M = 1.31 * 0.85 ~ 1.1.

For structural concrete components with failure criteria dominated by the concrete compression strength the coefficient of variation is typically V_R =0.10, the coefficient of variation for the model uncertainty V_δ =0.05, and there is no bias, b =1.0. This implies $\gamma_R \approx 1.20$. In Eurocode 2 for design of concrete structures it is taken into account that test specimens are not taken from the structure and therefore a conversion factor 1.15 is introduced, see Sedlacek et al. [30] implying γ_M = 1.20 * 1.15 ~ 1.4.

For structural concrete components with failure criteria dominated by the reinforcement strength the coefficient of variation is typically V_R =0.05, the coefficient of variation of the model uncertainty is V_δ =0.05, and there is no bias, b =1.0. This implies $\gamma_R \approx 1.20$ and the resulting partial safety factor becomes γ_M = 1.2.

To illustrate the importance of the uncertainty level of the load in extreme design load cases, a reduction factor that can be multiplied to the load partial safety factor, γ_f is determined using the same assumptions as in section 7.2. It is assumed that the coefficient of variation of the material strength is V_R =0.10 and the stochastic model in Table 7.3 is used as base case. The results are shown in Table 7.14.

Table 7.14. Reduction factor on load partial safety factor, γ_f.

	V_δ =0.00	0.05	0.10	0.15	0.20
Base case	1.00	1.00	1.00	1.00	1.00
COV (L)=0.20 (0.15)	0.98	0.97	0.98	0.98	0.97
COV (X_{dyn})=0.03 (0.05)	0.99	0.99	0.99	0.99	0.99
COV (X_{exp})=0.10 (0.15)	0.93	0.93	0.93	0.94	0.94
COV (X_{aero})=0.05 (0.10)	0.93	0.93	0.93	0.94	0.94
COV (X_{str})=0.00 (0.03)	0.99	0.99	0.99	1.00	0.99

It is seen that

- decreasing the uncertainty on the load effect, L results in a slightly reduced γ_f. This change is mainly because the characteristic value also changes when the COV changes.
- decreasing the COV on X_{dyn} (dynamic response) from 0.05 to 0.03 results in a very small reduction of γ_f.
- decreasing the COV on X_{exp} (site assessment) from 0.15 to 0.10 results in a reduction of γ_f of the order 6-7%
- decreasing the COV on X_{aero} (aerodynamics) from 0.10 to 0.05 results in a reduction of γ_f of the order 6-7%
- decreasing the COV on X_{str} (structural analysis) from 0.03 to 0.00 results in almost no reduction of γ_f

This clearly illustrates the importance of careful assessment of the wind load parameters for the partial safety factors and thus the resulting design. Especially the uncertainty related to site assessment and aerodynamic parameters are seen to be very important.

The importance of the uncertainty level of the load in fatigue design load cases is considered in section 7.2.

Finally, it is noted that the partial safety factors obtained as described above and implemented in the draft CD IEC 61400-1 ed. 4 (2014) generally only result in slight changes in the design values compared to the values obtained by the IEC 61400-1 ed. 3 (2005) standard. The main advantage of the new research and development performed as basis for the derivation of the partial safety factors is that a reliability-based approach has been used which opens up for application of probabilistic design of large wind turbines. One of the advantages is also that if more information and e.g. less uncertainty of some parameters are documented, then this information can be applied to obtain more cost-effective wind turbine components.

8. Impact of partial safety factors on Extreme Loads

8.1 Objectives

- Identify all sources of aerodynamic lift and drag uncertainty
- Build a stochastic model to quantify the lift and drag uncertainty
- Assess the effect of the net aerodynamic uncertainty on the prediction of extreme loads and structural reliability of large wind turbines using the First Order Reliability Method.
- Assess the effect of the loads safety factors in extreme operating conditions

8.2 Detailed Sources of Aerodynamic uncertainty

The main sources of uncertainty affecting variations in airfoil aerodynamic lift and drag are depicted in Fig 8.1 from left to right as: 1)Variations among wind tunnel measurements, 2) 3D rotational correction, 3) Surface roughness, 4)Geometric distortions of the blade during manufacturing and handling, Geometric distortions of the blade under loading, 5) Effect of Reynolds number (Re) and 6) Extending airfoil data to post stall:

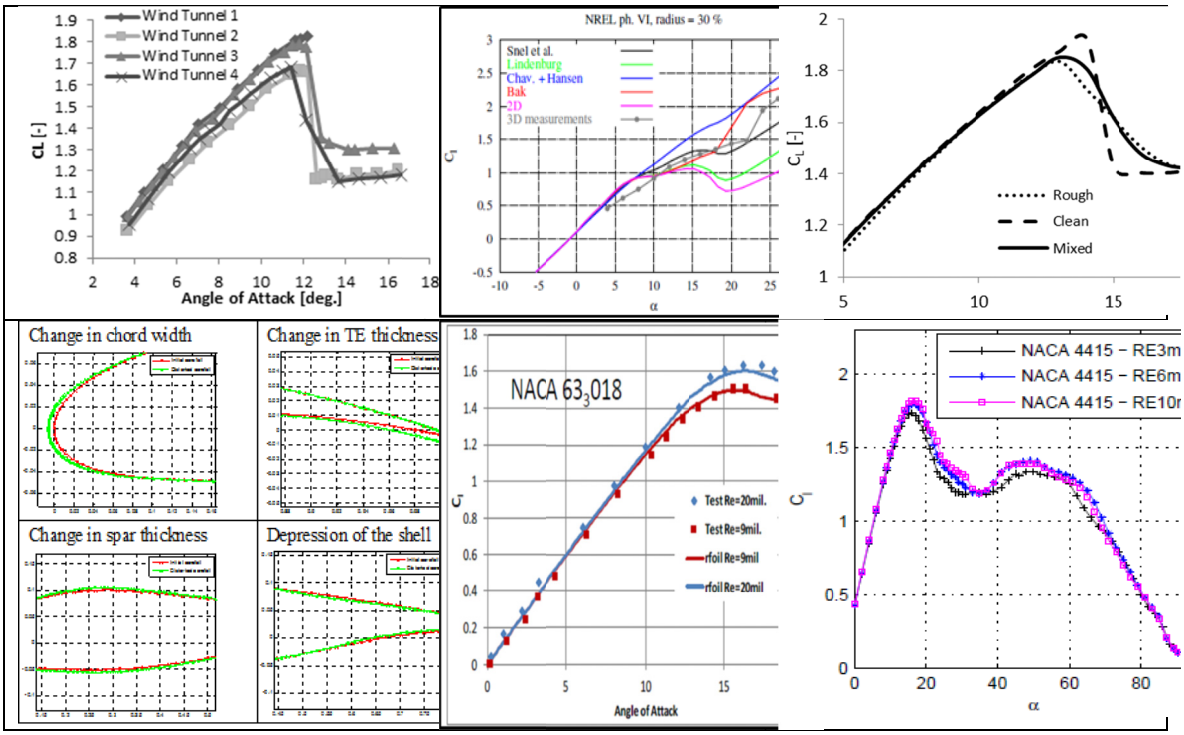

Figure 8.1: Sources of Uncertainty in Airfoil Charcatercstics

8.3 Stochastic model to describe airfoil characteristics

The first step is to parametrize the lift and drag coefficient curves: the parameters have a physical meaning, each parameter is a random variable and for each random variables propose a probability distribution.

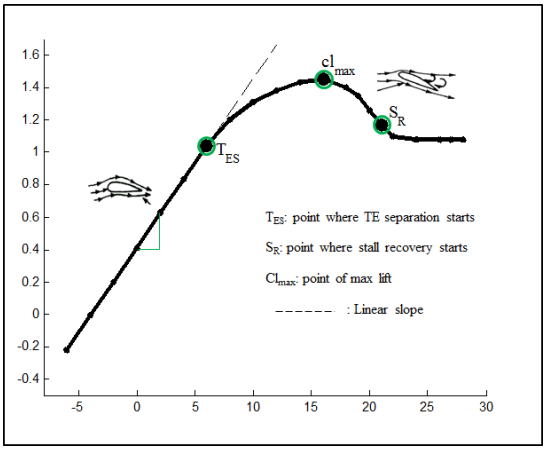

Figure 8.2: Parameters of the lift coefficient.

The next step is to define the stochastic model for coefficeint of lift as as $C_L X_{CL}$ where X_{CL} is random variable for the aerodynamic uncertainties defined above. X are defined for each of the parameters in Table 8.1.

Table 8.1 Stochastic variables and correlation matrix.

Variable	Distribution	Expected value	COV	Correlation Matrix					
				$X_{CL,max}$	$X_{CL,SR}$	$X_{CL,TES}$	$X_{AoA,max}$	$X_{AoA,SR}$	$X_{AoA,TES}$
$X_{dCL}d\alpha$	N (truncated)	1	0.033						
$X_{CD,90}$	N (truncated)	1	0.10						
$X_{CL,max}$	N (truncated)	1	0.12	1					
$X_{CL,SR}$	N (truncated)	1	0.08	0.9	1				
$X_{CL,TES}$	N (truncated)	1	0.13	0.9	0.9	1			
$X_{AoA,max}$	N (truncated)	1	0.08	0.6	0.5	0.6	1		
$X_{AoA,SR}$	N (truncated)	1	0.15	0.4	0.4	0.5	0.6	1	
$X_{AoA,TES}$	N (truncated)	1	0.10	0.5	0.5	0.6	0.5	0.8	1

The stochastic model can thus be used to generate synthetic lift and drag curves as shown below.

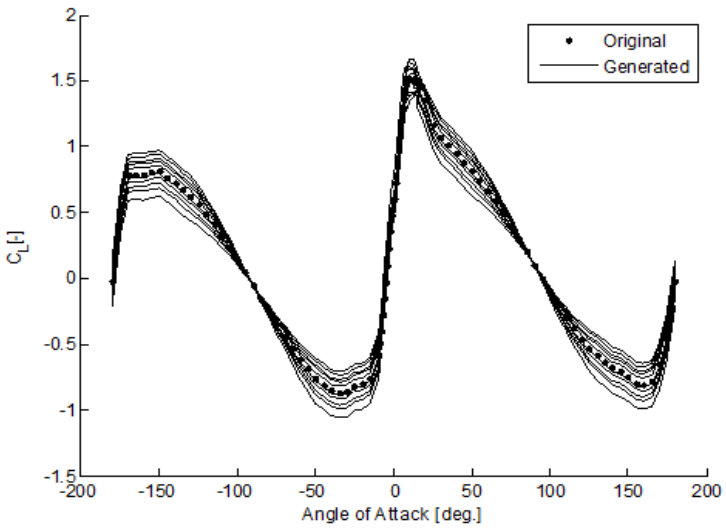

Figure 8.3: Parameters of the lift coefficient.

8.3 Effect on Structural reliability and safety factors in extreme turbulence operating conditions

The effect of the airfoil aerodynamic uncertainty in normal production in extreme turbulence on large multi-megawatt turbine with nominal power$\geq 5MW$ and rotor diameter $\geq 130m$) was verified. The aero-servo-elastic simulations were done using the FAST software [35].

The obtained results of the effect of aerodynamic uncertainty on extreme loads on various components of the wind turbine are shown in Table 8.2, and the details of which are presented in Ref.[36].

Table 8.2: Most likely COV of uncertainty related to airfoil data for various load components. The COV correspond to correlated airfoil data in DLC1.3ETM.

Load Component	**Most likely COV**
RootMyb1	7%
RootMxb1	2%
Spn4MLyb1	11%
Spn4MLxb1	5%
LSSTipMzs	12%
TwrBsMyt	7%

In the first application we use a cost and reliability based optimization scheme to optimize the geometry of a tower (tower bottom diameter D and sheet thickness).

Table 8.3 Optimal design of a tower in stand-still loading with a target probability of failure of 5x10-4 as a function of the COV of airfoil aerodynamic uncertainty.

Target p_f	COV X_{aero}	D [m]	t [mm]
$5 \cdot 10^{-4}$	0.20	5.65	15.9
$5 \cdot 10^{-4}$	0.10	5.40	15.1
$5 \cdot 10^{-4}$	0.04	5.33	14.9
$5 \cdot 10^{-4}$	0.02	5.33	14.9

Using an ultimate limit state formulation for blade failure in FORM, the load safety factor for a blade is calibrated for a target reliability index level of $\beta = 3.09 (p_f = 10^{-3})$

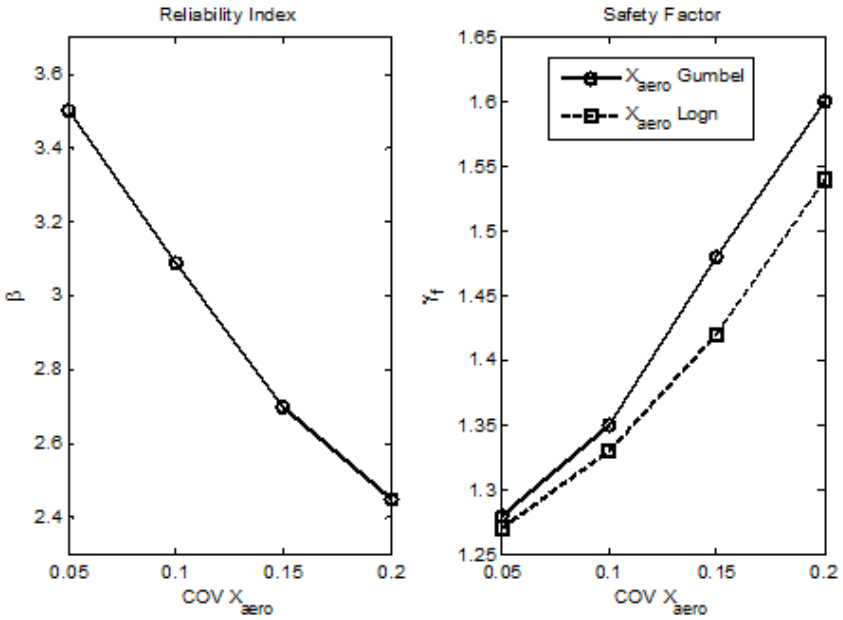

Figure 8.3: Variation of reliability index with aerodynamic COV for fixed safety factors $\gamma_m = 1.25$ and $\gamma_f = 1.35$. Variation of the load safety factors as a function of COV when Xaero is assumed Gumbel distributed and Lognormal distributed and reliability index set to 3.09.

9. Influence of the load control system on wind turbine 1 structural reliability in power production in extreme 2 turbulence

9.1 Motivation

Advanced load alleviation control features not only reduce the extreme load level but also modify the extreme load distribution and its tail. Both a reduction in the extreme load level and its distribution has a direct effect on structural reliability and safety factors.

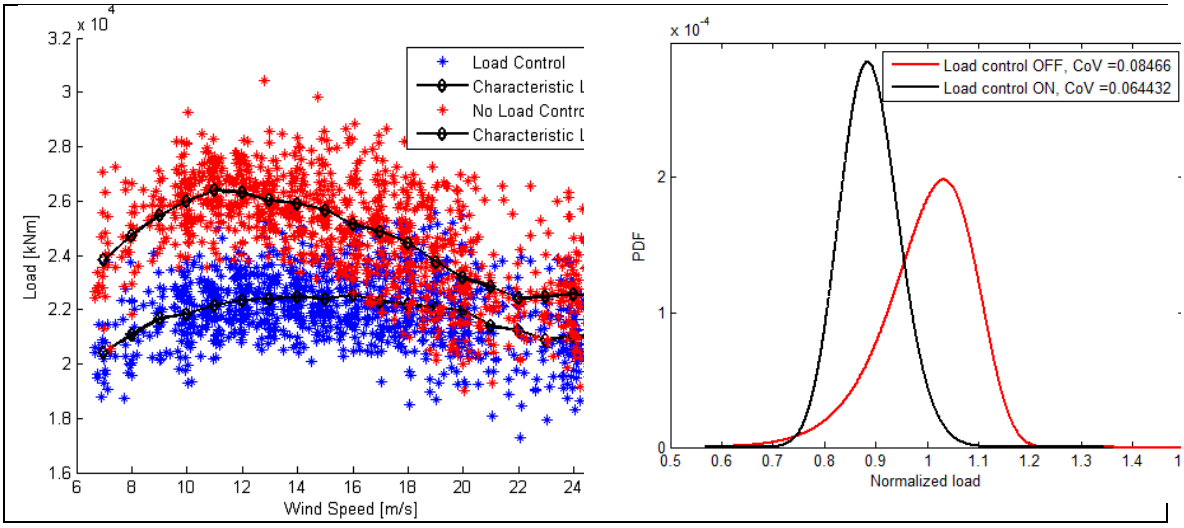

Figure 9.1: Advanced load alleviation control features not only reduce the extreme load level but also modify the extreme load distribution and its tail.

9.2 Research questions

How does the structural reliability of the wind turbine change if the extreme turbulence model is uncertain? In the presence of such uncertainty how does the structural reliability change with/without advanced load alleviation control features? Can wind turbine designers leverage the load limiting effects of the advanced load alleviation control features to optimize the loads safety factors?

9.3 Objectives

- Identify how advanced load control system reduce the uncertainty in the external inflow and turbulence on the extreme loading.
- In the presence of extreme turbulence inflow uncertainty calculate the structural reliability of wind turbine under the influence of various load control features.

- optimize the loads safety factors in extreme operating conditions under the influence of advanced load control features .

9.4 Probabilistic framework

The aero-servo-elastic simulations were done in FAST on large multi-megawatt turbine with nominal power≥ $5MW$ and rotor diameter $\geq 130m$). Three configurations of the control system are considered in the aero-servo-elastic simulations:

A basic control system ensures that the wind turbine runs at optimal collective pitch and tip speed below rated wind speed and constant rotor speed (RPM) above rated wind speed. No features for structural load alleviation are included.

In addition to the above functionalities, a cyclic pitch control and a static rotor thrust limiter control are included.

In addition to the above functionalities, individual pitch control and condition based thrust limiter are included.

The complexity and load reduction performance of the controller increases from configuration 1 to configuration 3. All controllers are based on a standard PI formulation. These configurations are applicable to a pitch regulated variable speed wind turbine.

In order to analyse the structural reliability in the presence of uncertainties in the turbulence model, it is necessary to derive the probability distribution of the load with a yearly reference period. This distribution is derived through the long term extrapolated probability distribution. The long term probability distribution for the maximum 10-minute load effect l conditional on mean wind speed v and turbulence σ_1 is modelled as follows:

$$F_{shortterm}(l|T_{10min}, v, \sigma_1) = F_{local}(T_{10min}, v, \sigma_1)^{n(\sigma_1, v)} \tag{9.1}$$

$$F_{longterm}(l|T_{10min}) = \int_{V_{in}}^{V_{out}} \int_0^{\infty} F_{shortterm}(l|T_{10min}, v, \sigma_1) f_{\sigma_1|V}(\sigma_1|v) f_V(v) \mathrm{d}\sigma_1 \mathrm{d}V \tag{9.2}$$

where $n(\sigma_1, V) = 1$ is the expected number of uncorrelated maxima in 10 minutes extracted from each 10 min simulation. F_{local} is the local (or short term) probability distribution for the load process which is chosen to be a 3-parameter Weibull distribution function [37]. The long-term probability of exceedance is then computed by integrating all of the short-term loads distributions with the joint PDF of wind speed and turbulence. The annual maximum probability distribution is finally derived as follows.

$$F_{longterm}(l|T_{1year}) = F_{longterm}(l|T_{10min})^N \tag{9.3}$$

where N is the number of 10min periods in one year $(= 365 \cdot 24 \cdot 60min/10min)$. The annual maximum distributions for the load effect are plotted in figures 9.2-9.3 for the blade root flapwise bending moment and tower bottom fore-aft bending moment respectively. Figure 9.3 shows the goodness of fit of the 3-Parameter Weibull distribution. The plots indicate that the resulting long term distributions with/without load alleviation control features differ significantly.

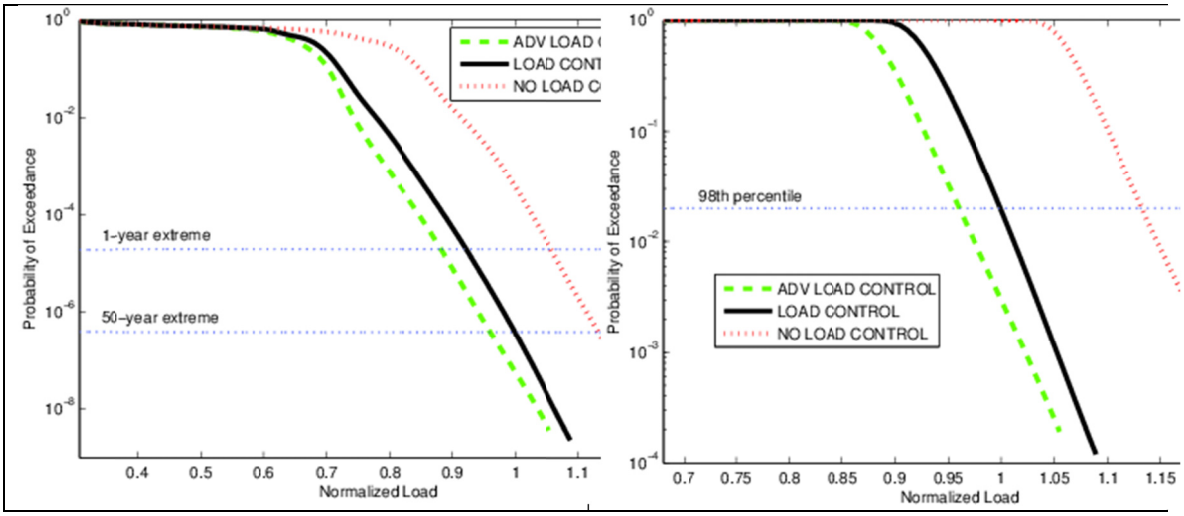

Figure 9.2: exceedance probability using a10min reference period and a 1 year reference period

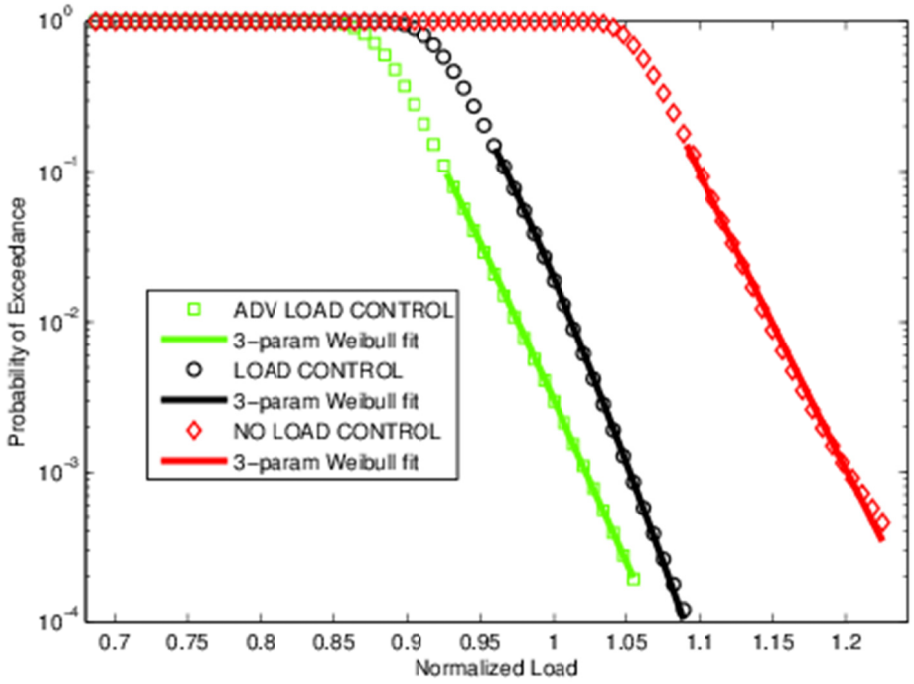

Figure 9.3: 3-parameter Weibull distribution fit.

The corresponding PDFs of the extrapolated distributions shown in Fig. 9.2 and 9.3 are depicted in Fig 9.4, wherein it can be seen that the control methods not only shift the variation of load, but also the mean extreme load.

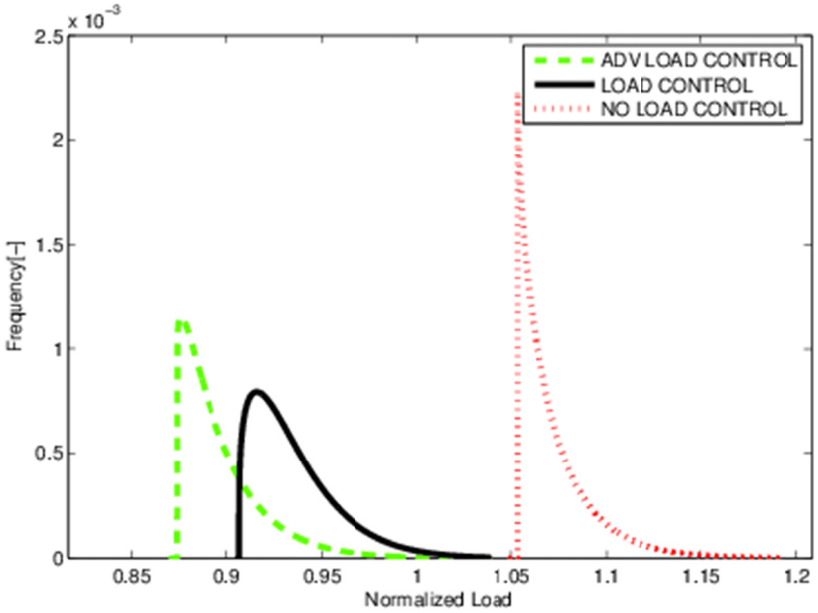

Figure 9.4: PDF (1 year reference period).

Figure 9.4 : Long term exceedance probability for the blade root flapwise bending moment for (a) 10-min reference period and (b) 1-year reference period. (c) 3-parameter Weibull distribution fit to the annual maximum probability distribution and (d) the corresponding density function for the blade root flapwise bending moment.

9.5 Structural reliability in extreme turbulence

For the structural reliability analysis an ultimate Limit State Function (LSF) is defined in order to include the load and resistance uncertainties: LSFLimit State FunctionSRFStress Reserve Factor

$$g = zM_{cr}X_R - L_{ULT}(\sigma_1, v)X_{dyn}X_{st}X_{ext}X_{sim}X_{exp}X_{aero}X_{str} \tag{9.4}$$

and the corresponding design equation is:

$$G = SRF\,\frac{M_{cr,c}(z)}{\gamma_m} - \gamma_l L_{ULT,c}(\sigma_1, v) \tag{9.5}$$

where $X_{y,ss}$ is the yield strength model uncertainty, $X_{E,ss}$ is the Young's modulus model uncertainty, $F_{y,ss}$ is the yield strength for structural steel, E is the Young's modulus and X_{cr} is the critical load capacity. The design variables $z = \{D, t\}$ are the tower bottom diameter and the structural steel sheet thickness. The tower bottom diameter and thickness of the reference turbine are specified to $6.27m$ and $0.041m$, respectively. For the blade $zM_{cr}X_R$ will not be further expanded.

$L_{ULT}(t, v)$ is the extreme load ($L_{ULT,c}$ is the characteristic value) as defined in terms of the turbulence and wind speed. Additional stochastic variables are defined as multiplicative factors to the resistance and load to take into account the model and statistical sources of uncertainties. X_{dyn} accounts for model uncertainty due to the modelling of the wind turbine dynamic response. X_{st} accounts for the statistical uncertainty of wind climate assessment. X_{ext} is associated with the extrapolated load model. X_{sim} accounts for statistical uncertainties caused by the limited number of loads simulations. X_{exp} accounts for the model uncertainties related to

modelling the terrain and roughness. X_{aero} accounts for the model uncertainties related to the assessment of aerodynamic lift and drag coefficients. Finally the uncertainties related to the computation of the stresses on components from the loads is considered through X_{str}. Uncertainties related the control parameters are not directly included here. The stochastic variables of the LSF are described in Appendix 1. The structural reliability is assessed by solving the LSF using FORM. The outcome is defined by the reliability index β. The reliability results are presented for five uncertainty scenarios:

1) A reference scenario where the turbulence model is as defined in [38] with an $I_{ref} = 0.14$ and mean wind speed of $10m/s$.
2) Scenario which is similar to scenario 1 except the turbulence is assumed to follow an extreme value distribution instead of the lognormal distribution. The objective here is to study the effect on structural reliability if the turbulence were not log-normally distributed.
3) The next scenario is similar to scenario 1 except the mean wind speed is set to $11m/s$ instead of $10m/s$ and follows a Rayleigh distribution. The objective here is to study the effect on structural reliability if the mean wind speed is higher than the reference design.
4) In this scenario the turbulence is assumed to follow a lognormal distribution with $I_{ref} = 0.16$ instead of 0.14 and the mean wind speed is set to $10m/s$ and follows a Rayleigh distribution. The objective here is to study the effect on structural reliability if I_{ref} is higher than the reference design.
5) In this scenario the turbulence model is redefined where $\mu_{(\sigma_1|V)} = I_{ref}(v-1)$ and $\sigma_{\sigma_1|V} = I_{ref}(0.089v + 2)$ with $I_{ref} = 0.14$ [6]. Turbulence is still assumed to follow a lognormal distribution. The mean wind speed is set to $10m/s$ and follows a Rayleigh distribution. The turbulence model is derived based on 6-years of wind measurements from Høvsøre. The objective here is to study the effect on structural reliability if the definition of the turbulence model (including mean and standard deviation of turbulence) are modified compared to the reference design.

The structural reliability of the blade (blade root extreme flapwise bending moment) and tower (tower bottom extreme fore-aft bending moment) are assessed for each of the five scenarios for the three control system configurations. An acceptable reliability index is $\beta \geq 3.3$ corresponding to an annual probability of failure $p_f \leq 5 \cdot 10^{-4}$. The results are shown in tables 9.1 and 9.2 for the blade and tower respectively. Further details of the methods are found in Ref.[39].

Table 9.1: Annual structural reliability index of the blade (blade root extreme flapwise bending moment).

Uncertainty Scenario	**Control Configuration 1: No structural load alleviation features, simple controller**	**Control Configuration 2: with structural load alleviation features (Reference)**	**Control Configuration 3: with advanced structural load alleviation features**
1	2.77	3.42	3.62

2	2.76	3.34	3.52
3	2.87	3.50	3.66
4	2.58	3.15	3.37
5	1.70	2.35	3.02

Table 9.2 Annual structural reliability index of the tower (tower bottom extreme fore-aft bending moment).The tower bottom diameter and thickness are $6.27m$ and $0.041m$, respectively.

Uncertainty Scenario	**Control Configuration 1: No structural load alleviation features, simple controller**	**Control Configuration 2: with structural load alleviation features (Reference)**	**Control Configuration 3: with advanced structural load alleviation features**
1	2.30	3.38	4.18
2	2.28	3.29	4.13
3	2.32	3.45	4.20
4	2.17	3.16	4.00
5	1.50	2.45	3.42

How to interpret the structural reliability results? The reference control design performance in extreme turbulence operation delivers acceptable structural reliability with $\beta \geq 3.3$ (configuration 2 in tables 2-3). Uncertainty in Iref seems to have the largest impact on structural reliability (scenario 4 in tables 9.1-9.2). The structural reliability in all scenarios drops significantly when no load alleviation features are included in the control system (configuration 1). This is not unexpected as the load alleviation features are an integral part of the reference turbine structural load calculations in configuration 2. This indicates that when a turbine design relies heavily on control features to achieve structural load reductions (lighter turbine design), control architecture and failure modes analysis should be studied very closely beyond the load cases recommended in the IEC61400-1 due to the severe drop in reliability.

Does the control system complexity and performance affect the structural reliability when the extreme turbulence model is uncertain? Advanced load control features which are able to adapt their parameters settings to external inflow conditions (configuration 3 in tables 9.1-9.2) show a satisfactory performance in improving the structural reliability as showcased, for instance, in scenario 4 corresponding to a large increase in the turbulence compared to the design turbulence; for the blade the reliability index increases from 3.33 to 3.60 and from to 4.53 for the tower. This indicates that large uncertainty in the extreme turbulence model can be significantly lowered through the use of advanced load control features. However, the cost and complexity of the control system increases which warrants additional failure modes analysis of the controller and its architecture and probably additional maintenance provisions. Inadvertently this leads to the logical next step of an integrated design and optimization

approach of the wind turbine control system and structural reliability from a cost-benefit point of view.

Effect of structural load control on AEP Increased structural reliability is achieved with increased complexity of the load alleviation features of the control system. The next logical step is to verify the impact of the load control on the Annual Energy Production (AEP) of the wind turbine. Generally, load reduction is achieved by reducing the aerodynamic thrust on the rotor. Power C_P and C_T thrust coefficient are related through the axial induction factor a (2D actuator disk: $C_P = 4a(1-a)^2$ and $C_T = 4a(1-a)$). Hence any reduction in thrust is accompanied with a reduction in power and vice-versa. Figure 9.5 shows a comparison of the power curves when no load control features are included, when load control features are included and when advanced load control features are included (configurations 1-3). In the case where the load control features are included (configuration 2) a 3.1% loss in AEP is incurred relative to configuration 1. However this value drops to 1.8% AEP loss when advanced load reduction features are included (configuration 3). Generally the AEP loss is accepted in light of the overall cost of energy achieved. The AEP are calculated for an average wind speed of $10m/s$ and turbulence intensity of 10%.

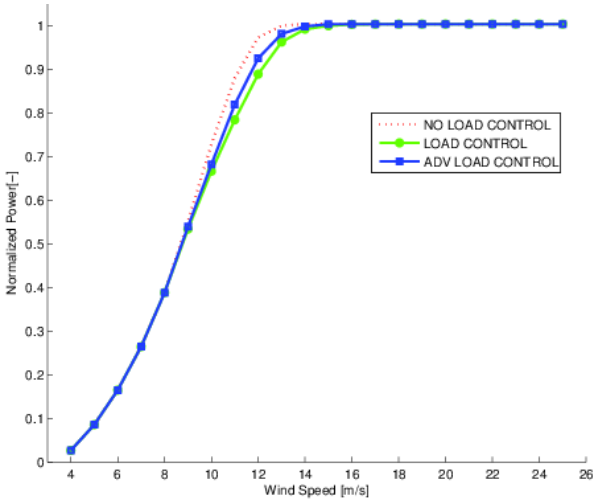

Figure 9.5: Power curves (normalized by rated power) when (1) no structural load control features are included, when (2) structural load control features are included and when (3) advanced structural load control features are included.

The above discrete uncertainty scenarios give an intuitive and clear understanding of the effect of uncertainty in the mean wind speed or the turbulence or turbulence distribution or the definition of the extreme turbulence model on the structural reliability. One can easily generalize the above discrete uncertainty scenarios and assume inter-annual variations in the mean wind speed and the turbulence intensity or any other environmental variables (for example $V_{avg} \sim LN(10m/s, COV = 0.05)$, $\sigma_1 \sim LN(0.14m/s, COV = 0.05)$, $k \sim LN(2, COV = 0.05)$, etc.) and generate a surrogate model of the maximum annual loads which can then be used in the reliability analysis (for instance using Kriging and/or Polynomial Chaos

9.5 Cost and reliability based optimizations in the presence of load alleviation control system

It can be argued that the acceptable reliability level of a wind turbine can be chosen based on a cost optimization with an objective function that includes the benefits (i.e.money made on selling energy production) and the investment cost (money spent on research and development, design, testing, manufacturing and installation) and the failure cost (removal and replacement of failed component) in case of failure. The objective is thus to maximize the benefits relative to the incurred costs:

$$W = B - [C_I + C_F] \tag{9.6}$$

In the above, B are the benefits such as the annual energy production of a wind turbine, C_I are the initial investments costs including the costs of research, development, manufacturing and installation, C_F are the costs of failure and replacement in case of failure of components.

In case where one wind turbine is considered and assuming systematic rebuild in case of failure, Equation 9.6 becomes:

$$W = \frac{B}{rC_0} - \left[\frac{C_I}{C_0} + \left(\frac{C_I}{C_0} + \frac{C_F}{C_0}\right)\frac{p_f}{r+p_f}\right] \tag{9.7}$$

The cost and reliability based optimization formulation is thus cast as follows:

$$\begin{aligned} \underset{z,\gamma}{\text{maximize}} \quad & W(z,\gamma) \\ \text{subjectto} \quad & z^l \le z \le z^u, \\ & p_f \le p_f^{max}, \\ & \gamma^l \le \gamma \le \gamma^u, \\ & G = SRF\frac{M_{cr,c}(z)}{\gamma_m} - \gamma_l L_{ULT,c} = 0 \end{aligned} \tag{9.8}$$

In the above equation, the control system is not taken into account. In order to take the control system into account, Equation 9.7 is modified to:

$$W = \left[\frac{B}{rC_0} - \nu_{\overline{CTR}}\frac{B}{rC_0}\right] - \left[\left(\frac{C_I}{C_0} + \frac{C_{cs}}{C_0}\right) + \left(\frac{C_I}{C_0} + \frac{C_F}{C_0}\right)\left(\frac{p_f+\nu_{\overline{CTR}}}{r+p_f+\nu_{\overline{CTR}}}\right)\right] \tag{9.9}$$

The above expression is intuitive; the benefits B decrease with increased control system failure, the initial investment costs C_I increase with additional control system cost C_{cs} and sophistication of the load alleviation features (advanced load alleviation control features might require additional research and development, additional sensors, algorithms, larger requirements for computing power, additional quality control, etc.), and finally the discounted lifetime failure and replacement costs increases with increasing probability of failure of the control system (here the control system and structure are assumed to be in series). The cost and reliability based optimization formulation is thus cast as follows:

$$\begin{aligned} \underset{z,\gamma,\nu_{\overline{CTR}}}{\text{maximize}} \quad & W(z,\gamma,\nu_{\overline{CTR}}) \\ \text{subjectto} \quad & z^l \le z \le z^u, \\ & \gamma^l \le \gamma \le \gamma^u, \\ & p_f + \nu_{\overline{CTR}} \le p_f^{max}, \\ & G = SRF\frac{M_{cr,c}(z)}{\gamma_m} - \gamma_l L_{ULT,c} = 0 \end{aligned} \tag{9.10}$$

where G is the design equation corresponding to the limit state function, $M_{cr,c}$ is the characteristic yield bending strength, $L_{ULT,c}$ is the characteristic ultimate load (i.e. bending

moment), γ_m is the material safety factor, γ_l is the load safety factor, z is the set of design variables (for instance the tower bottom diameter D and sheet thickness t) which depends on the geometry and stiffness of the component and SRF is the Stress Reserve Factor. If the component has not been designed to the limit, the SRF will be larger than 1, reflecting the extra safety margin. The structural probability of failure p_f is derived when solving the LSF in FORM, and $\nu_{\overline{CTR}}$ is the annual failure rate of the load alleviation features in the control system. The superscripts l and u denote lower and upper bounds respectively. The computed safety factors reflect the possible savings resulting from the cost optimal reliability level computed in the optimization problem cast in Equation. Finally, r is the real rate of interest.

The initial investment costs are:

$$\frac{C_I}{C_0} = \frac{2}{3} + \frac{1}{3}\frac{Dt - t^2}{D_0 t_0 - t_0^2} \tag{9.11}$$

The annual benefits are set to:

$$\frac{B}{C_0} = \frac{1}{8} \tag{9.12}$$

and the failure and replacement costs:

$$\frac{C_F}{C_0} = \frac{1}{36} \tag{9.13}$$

Finally the cost related to the marginal improvements in the control system is inversely proportional to the probability of failure of the control system:

$$\frac{C_s}{C_0} = 0.001\frac{1}{P(\overline{CTR})} \tag{9.14}$$

Application 1: Upscaling of existing wind turbine geometry

A wind turbine designed with the reference controller (configuration 2) is to be upscaled while keeping the hub-drivetrain-nacelle structure-yaw systems as little modified as possible. Upscaling involves modifying rated power, IEC design climate conditions, the rotor size, rotor speed, etc. or a combination thereof. The design specifies that the tower and foundation are to be maintained unchanged. The reference tower, designed using control configuration 2, has $D_o = 6.27m$ and $t_o = 0.041m$, corresponding to an annual reliability index of 3.38 (annual $p_f = 3.56 \cdot 10^{-4}$).

The "upscaling" is mostly made possible by integrating advanced load alleviation control features. The objective is thus to investigate how much could the extreme loads on the tower bottom/foundation be increased while maintaining an acceptable target probability of failure of $p_f^{max} = 5 \cdot 10^{-4}$.

This is done by shifting the extreme load distribution derived with load controller configuration 3 as much as possible (corresponding to higher characteristic extreme load level) until the probability of failure of the tower derived in FORM does not exceed p_f^{max} under the constraint that the design equation satisfies $G = SRF\frac{M_{cr,c}(z)}{\gamma_m} - \gamma_l L_{ULT,c} \geq 0$.

Maintaining the tower and foundation geometry with the same load, material safety factors ($\gamma_l = 1.35$, $\gamma_m = 1.25$ respectively), we are able to lower the extreme load level by 21%. The advanced load alleviation features in the control system made it possible to reduce the load, but knowing the full probability distribution of the load, addition load cases are possible to assess the probability of failure of the tower. Hence together with the load safety factor we are

able to translate the increase in load level into a probability of failure. A designer can now translate the 21% increase in extreme design load level into larger rotor diameter, higher rated output power, higher operating IEC design climate conditions or a combination thereof.

Application 2: cost and reliability optimization of tower bottom geometry and safety factors. No constraints on tower geometry.

The reference tower, designed using control configuration 2, has $D_o = 6.27m$ and $t_o = 0.041m$, corresponding to a reliability index of 3.38 ($p_f = 3.56 \cdot 10^{-4}$). The tower base is designed to the limit with a load safety factor and material safety factors of 1.35 and 1.25 respectively. It is clear that the probability of failure for this reference tower design is indeed lower than the target of $5 \cdot 10^{-4}$. The normalized direct cost for the reference tower is by definition $C_I C_0 = 1.0$ (Equation 11) and the benefit-cost equation $W = 1.08$ for a real rate of interest $r = 0.06$. We will apply the cost and reliability optimization described above (equation 10) with $p_f^{max} = 5 \cdot 10^{-4}$ in order to derive a cost optimal tower geometry and safety factors. The optimization is done using the Matlab function $fmincon$. The cost and reliability optimization of the tower base is done without any constraints on tower stiffness or frequency. Table 3 shows the results assuming the tower is designed with control configuration 2 (basic reference controller) and control configuration 3 where advanced load alleviation control features are used.

Table 9.3: Cost and reliability based optimization of tower base geometry and loads safety factor when stiffness and frequency constraints are not included.

Control Configuration	**D**	**t**	γ_l	γ_m	β	p_f	W	$C_I C_0$
Control Configuration 2: with structural load alleviation features (Reference)	8.80	0.026	1.33	1.25	3.3	$5 \cdot 10^{-4}$	1.11	0.96
Control Configuration 3: with advanced structural load alleviation features	8.32	0.024	1.36	1.25	3.3	$5 \cdot 10^{-4}$	1.15	0.93

The control system failure rate is not included in this optimization. The material safety factor is set to a constant $\gamma_m = 1.25$. The target probability of failure is set to $p_f^{max} = 5 \cdot 10^{-4}$. The cost optimal turbine, with control configuration 2, has $D = 8.80m$, $t = 0.026m$, a loads safety factor $\gamma_l = 1.33$ and a corresponding cost optimal probability of failure of $p_f = 5 \cdot 10^{-4}$. The materials safety factor is set to a constant $\gamma_m = 1.25$. The normalized direct cost $C_I C_0 = 0.96$ and the benefit-cost equation $W = 1.11$. The drop in safety factor from 1.35 to 1.33 is largely attributed to the drop in probability of failure from $p_f = 3.56 \cdot 10^{-4}$ to the cost optimal probability of failure $p_f = 5.0 \cdot 10^{-4}$.

The cost optimal turbine, with control configuration 3 (advanced load alleviation control features), has $D = 8.32m$, $t = 0.024m$, a loads safety factor $\gamma_l = 1.36$ and a corresponding cost optimal probability of failure $p_f = 5 \cdot 10^{-4}$. The materials safety factor is set to a constant $\gamma_m = 1.25$. The normalized direct cost $C_I C_0 = 0.93$ and the benefit-cost equation $W = 1.15$. The drop in the $C_I C_0$ from 0.96 to 0.93 (a drop of 3.2%) and the increase in benefits from 1.11 to 1.15 (an increase of 3.6%)is largely attributed to the drop in the extreme load level due to the introduction of the advanced load alleviation control features.

Repeating the above optimization, setting the target probability of failure to $p_f^{max} = 1 \cdot 10^{-3}$ and optimizing for the load safety factor while keeping the material safety factor constant ($\gamma_m = 1.25$) the results are shown in Table 0. A tangible reduction in safety factor is achieved because of the lower target probability of failure ($p_f = 5 \cdot 10^{-4}$ versus $p_f = 1.0 \cdot 10^{-4}$). However we observe that the benefits W and the direct costs $C_I C_0$ are unchanged compared to previously. This is typical behaviour of cost and reliability based structural optimization problems where the optimal benefit-cost may be flat. This is an interesting result since we are able to lower the structural probability of failure for no or marginal change in benefits and costs.

Table 4: Cost and reliability based optimization of tower base geometry and loads safety factor when no stiffness and frequency constraints are included.

Control Configuration	**D**	**t**	γ_l	γ_m	β	p_f	W	$C_I C_0$
Control Configuration 2: with structural load alleviation features (Reference)	7.88	0.029	1.30	1.25	3.21	$6.6 \cdot 10^{-4}$	1.11	0.96
Control Configuration 3: with advanced structural load alleviation features	7.72	0.026	1.33	1.25	3.2	$6.9 \cdot 10^{-4}$	1.15	0.92

The control system failure rate is not included in this optimization. The material safety factor is set to a constant $\gamma_m = 1.25$. The target probability of failure is set to $p_f^{max} = 1 \cdot 10^{-3}$. In Table 9.4, the cost optimal probability of failure is $p_f = 6.9 \cdot 10^{-4} (\leq 1.0 \cdot 10^{-3})$, yielding a loads safety factor $\gamma_l = 1.33$ for control configuration 3. Now if instead of a constraining the probability of failure to be $\leq 1.0 \cdot 10^{-3}$, we force the probability of failure to be equal to $1.0 \cdot 10^{-3}$. We find that the corresponding loads safety factor drops to $\gamma_l = 1.30$ with marginal change in the benefit-cost function $W = 1.14$ while the initial investment cost remains unchanged $C_I C_0 = 0.92$. This is typical behaviour of cost and reliability based structural optimization problems where the optimal benefit-cost is rather flat.

The advanced load alleviation control features in control configuration 3 result in a lower extreme characteristic load level and tighter spread (i.e. lower COV) compared to control configuration 2 . However, In the above we see that this does not translate into lower load safety factor as one would expect. That could be due to several reasons: The low COV of the extreme load distribution in control configuration 3 results in the characteristic load level (98 percentile) being very close to the mean of the distribution (i.e. tight extreme load distribution). Hence a larger safety factor is required to reach the design load level. The low COV of the extreme load distribution in control configuration 3 means that model uncertainties in the limit state function (Equation 4) start to dominate the reliability analysis in FORM. Hence, any reduction in the load safety factor would require a reduction in model uncertainties. The tail of the extreme load distribution in control configuration 3 is very difficult to determine due to the limiting effects of the advanced load control features on the peak loads. A poorly determined distribution tail would inevitably result in a highly sensitive reliability analysis and hence safety factors.

Application 3: cost and reliability optimization of tower bottom geometry and safety factors. Constrained tower stiffness.

We now repeat the above cost and reliability based optimization but we impose constraints on the tower stiffness and frequency. This is done by constraining the plastic section modulus[1] of the cost optimal tower to be equal to that of the reference tower. The target probability of failure is set to $p_f^{max} = 5 \cdot 10^{-4}$ and the material safety factor is kept constant ($\gamma_m = 1.25$). The results are shown in Table 9.5. The optimal safety factors, reliability index, benefits W and direct cost $C_I C_0$ are pretty much the the same compared to the non-stiffness constrained optimization presented in the Application 2 above.

Table 9.5 Cost and reliability based optimization of tower base geometry and loads safety factor when section modulus constraints are included. The control system failure rate is not included in this optimization. The target probability of failure is set to $p_f^{max} = 5 \cdot 10^{-4}$.

Control Configuration	**D**	**t**	γ_l	γ_m	β	p_f	W	$C_I C_0$
Control Configuration 2: with structural load alleviation features (Reference)	6.50	0.038	1.32	1.25	3.3	$5.0 \cdot 10^{-4}$	1.09	0.99
Control Configuration 3: with advanced structural load alleviation features	7.90	0.026	1.36	1.25	3.3	$5.0 \cdot 10^{-4}$	1.15	0.93

[1] $\frac{1}{6}(D^3 - (D-2t)^3)$

Repeating the above stiffness constraint optimization, setting the target probability of failure to $p_f^{max} = 1 \cdot 10^{-3}$ and optimizing for the load safety factor while keeping the material safety factor constant ($\gamma_m = 1.25$) the results are shown in Table 9.6. The control system failure rate is not included in this optimization. The material safety factor is set to a constant $\gamma_m = 1.25$. The target probability of failure is set to $p_f^{max} = 1 \cdot 10^{-3}$.

Table 9.6 Cost and reliability based optimization of tower base geometry and loads safety factor whenstiffness and frequency constraints are included.

Control Configuration	**D**	**t**	$\boldsymbol{\gamma_l}$	$\boldsymbol{\gamma_m}$	$\boldsymbol{\beta}$	$\boldsymbol{p_f}$	$\boldsymbol{W}$	$\boldsymbol{C_I C_0}$
Control Configuration 2: with structural load alleviation features (Reference)	6.93	0.033	1.27	1.25	3.09	$1.0 \cdot 10^{-3}$	1.10	0.97
Control Configuration 3: with advanced structural load alleviation features	8.04	0.025	1.33	1.25	3.18	$7.3 \cdot 10^{-4}$	1.15	0.92

In Table 9.6, the cost optimal probability of failure is $p_f = 7.3 \cdot 10^{-4} (\leq 1.0 \cdot 10^{-3})$, yielding a loads safety factor $\gamma_l = 1.33$ for control configuration 3. Now if instead of a constraining the probability of failure to be $\leq 1.0 \cdot 10^{-3}$, we force the probability of failure to be equal to $1.0 \cdot 10^{-3}$. We find that the corresponding loads safety factor drops to $\gamma_l = 1.31$ with marginal change in the benefit-cost function $W = 1.14$ while the initial investment cost remains unchanged $C_I C_0 = 0.92$. As in the previous example, this is typical behaviour of cost and reliability based structural optimization problems where the optimal benefit-cost is rather flat.

Thus it can be concluded [39] that tangible reduction in the load safety factor can be achieved when advanced load alleviation control features are used, but the magnitude of reduction will depend not only on the constraints put in place during the optimization and on the target probability of failure but also on the shape of the long term probability density function of the extreme loads.

Application 4: cost and reliability optimization of tower bottom geometry and safety factors. The controller cost C_{cs} and controller failure rate $\nu_{\overline{CTR}}$ are INCLUDED:

Here the control system cost and failure probability are included in this optimization. The target probability of failure is set to $\left(\lambda P_F + \nu_{\overline{CTR}}\right)^{max} = 5 \cdot 10^{-4}$.

Table 9.7 Cost and reliability based optimization of tower base geometry and loads safety factor when section modulus constraints are included.

Control Configuration	**D**	**t**	γ_l	γ_m	β	p_f	$\nu_{\overline{CTR}}$	W	$C_I C_0$
Control Configuration 2: with structural load alleviation features (Reference)	5.6	0.052	1.41	1.25	3.3	$1.5 \cdot 10^{-4}$	$3.5 \cdot 10^{-4}$	0.88	1.18
Control Configuration 3: with advanced structural load alleviation features	6.31	0.040	1.63	1.25	3.3	$1.5 \cdot 10^{-5}$	$4.9 \cdot 10^{-4}$	0.97	1.10

The optimum structural probability of failure in control configuration 3 is a decade lower compared to the structural probability of failure in control configuration 2. The probability of failure of the control system dominates the overall probability of failure, especially in the case of control configuration 3 where advanced load alleviation features are included. This means that decreasing the probability of failure of the control system (increase its reliability) would have a larger impact than improving the reliability of the structure.

The difference in the loads safety factor between the two control configurations is significantly larger than the difference between the loads safety factors presented in Table 9.7. This is due to the inclusion of the probability of failure of the control system which dominates the overall failure of the structure-control system.

The difference in the benefits-cost function W between the two control configurations is 5% in Table 9.6 while it increases to 10% in Table 9.7 when the probability of the failure of the control system is included in the optimization.

10.0 Utilization of project results - Recommendations Submitted to the IEC Standards a) IEC 61400-1 Ed.4 and b) IEC 61400-3 Ed. 2

The following recommendations were presented to the IEC TC88 MT01 committee in the meetings held between 2012-2014. The recommendations also apply to offshore wind turbines and are therefore also applicable to the TC88 WG03 committee.

- The Mann turbulence model parameters described in Annex B of the IEC 61400-1 Ed.3 2005 are based on the wind conditions described in section 6 and conforming to the Kaimal turbulence spectrum. This results in a Mann shear distrortion parameter (Γ) of 3.9, which is not consistent with most site specific wind measurements seen. At least for site specific analysis, the shear distortion (anisotropy) parameter γ, dissipation factor, $\alpha\epsilon^{\frac{2}{3}}$, and the length scale, l should be determined based on high frequency site specific measurements of the wind spectra $\boldsymbol{F_u(kl)}$, $\boldsymbol{F_v(kl)}$, $\boldsymbol{F_w(kl)}$ and $\boldsymbol{F_{uw}(kl)}$ at one fixed point. The Mann model turbulent wind field needs to be then generated based on the three model parameters derived from the one point measured spectra. Load analysis with DLC 1.1, 1.3 show that the numerical value of the Mann model parameters affect the design loads given the same mean wind speed and turbulence intensity. Further the proposed amendments in the IEC 61400-1 Ed. 4 CD allow the use of extreme turbulence in DLC 3.2, 4.2 and here also the numerical value of the Mann model parameters can greatly affect the extreme load magnitude.
- The shear exponent presently stated in the standards is a constant of 0.2 for onshore and 0.14 for offshore for the purposes of design load computations in normal wind conditions. It is seen that the wind shear exponent is seldom a constant value. It is proposed that the wind shear exponent is modelled as conditional on the turbulence with the 90% quantile of turbulence used to obtain the corresponding distribution of wind shear exponent with mean wind speed. As simplification for moderate turbulence flat terrain conditions, the shear exponent can be modelled as $\alpha(V_{hub}) = 0.088(Ln(V_{hub}) - 1), V_{hub} \geq 3m/s$
- It was determined through 9+years of high frequency measurements at the Høvsøre test site in Denmark, that the extreme turbulence model in the IEC 61400-1 standard is non-conservative as the 50-year extreme as predicted by the standard was found to be routinely exceeded in the de-trended wind measurements. The extreme turbulence model was therefore suggested to be modified whereby the variation of turbulence corresponds to the value $Var(\sigma_1|V_{hub}) = (I_{ref}*(0.089* V_{hub} + 2))^2$, which turns out to be similar to what was originally proposed in the Ed.2 of the standard. The expected value of turbulence may be correspondingly decreased so that the 90% quantile for normal turbulence is unchanged, or $E(\sigma_1|V_{hub}) = I_{ref}*(0.64* V_{hub} + 3)$
- Wind time series measurements must be linearly de-trended before computing its standard deviation to ascertain the correct turbulence intensity.
- Even though turbulence in the small scales is non-Gaussian and even at larger scales may be non-Gaussian due to various reasons, the modelling of turbulence using Gaussian models is seen not to affect the design extreme or design fatigue loads with the corresponding loads within 10% of each other in magnitude at all mean wind speeds. Therefore there is no necessity to use non-Gaussian approaches to model turbulence for design loads computation.
- A reliability based calibration of partial safety factors has been proposed that requires an assessment of the sources of uncertainty and their corresponding coefficient of variation. Compared to the corresponding factor in IEC 61400-1 ed. 3 (2005), the partial safety factor for component class 3 has been decreased from 1.3 to 1.2. The coefficient of variation for aerodynamic uncertainty was validated to be less than 10% for the purposes of extreme load computation. It was also determined that some of the partial safety factors for loads can be reduced if advanced load reducing controls are utilized in the wind turbine operation.

11 Project conclusion and perspective

The main findings of the project have been summarized in the previous section as recommendations to the IEC standards. The project has demonstrated the need for measured wind time series on sites with wind turbines in order to calibrate turbulence models. The project has further demonstrated the impact of wind models over large rotors on the turbine design loads and partial safety factors. A large number of papers have been published or in the process of being published as given in the References.

Further software for the generation of wind turbulence time series consistent with wind conditions over large rotors has been developed and which can be commerically used as appropriate by wind turbine manufacturers and certification bodies.

Future efforts should investigate cost effective wind turbulence measurement techniques which can be used in different regions of the world onshore and offshore, as well as in complex terrain.

Appendix 1 A step-by-step description of optimization of safety factors

This is a general account on how to determine and optimize safety factors (not calibration).

$$g = z \cdot R - L \tag{A1.1}$$

The design equation corresponding to the limit state function (Equation A1.2) is:

$$G = z \cdot \frac{R_c}{\gamma_m} - L_c\gamma_l \tag{A1.2}$$

where z is some design variable such as diameter, thickness, surface area, etc. R is the resistance of the structure and L is the loading. Analysis by FORM leads to determination of z in order to meet a target structural reliability level β corresponding to a probability of failure p_f. At the limit state surface, the design equation can be set to zero:

$$z \cdot \frac{R_c}{\gamma_m} - L_c\gamma_l = 0 \tag{A1.3}$$

Given a value for z, the safety factors read:

$$\gamma_m \cdot \gamma_l = z \cdot \frac{R_c}{L_c} \tag{A1.4}$$

now, given one random variable for resistance, one random variable for load and one failure mode for the structure (i.e. one LSF), then the safety factor can be derived as:

$$\gamma_m = \frac{R_c}{R^*} \tag{A1.5}$$

$$\gamma_l = \frac{L^*}{L_c} \tag{A1.6}$$

where L^* and R^* are the deisgn point of the load and Resistance respectively as computed in FORM. However, in case of multiple design variables, multiple load and resistance random variables for the structure, then the process is more involved and iterative:

Initial guess of γ_l and γ_m
Solve for the design variable z s.t. $G(X_c, z, \gamma) = 0$
$z \rightarrow$ FORM/SORM/Monte Carlo
- Compute reliability index β

Is $\beta \geq \beta^{target}$?
- if yes, then exit

Make new guess of γ_l and γ_m
Repeat steps $b - f$

Note that this is an optimization of the safety factor on one structure and one design variable. Further calibration of the safety factors ensures a more or less uniform reliability index across all sets of structures considered in the design; In case of multiple failure modes and/or multiple structures, the above optimization process is repeated for every structure and failure mode. The deviation of the reliability index for each of the structures and the overall desired (target) reliability index is minimized such that:

$$err = \sum_{i=1}^{N} \omega_i(\beta_i - \beta^{target})^2 \tag{A1.7}$$

where ω_i are weighting factors indicating the relative importance of the various structures and failure modes. The difference between the reliability index for each of the structures β_i and the desired (target) reliability index β^{target} reaches an error threshold err. Hence the chosen safety factors result in a more or less uniform reliability accross all N structures and failure modes when multiple design variables are considered.

The above procedure can be further augmented to take into account the cost of the designed structure in addition to the reliability as follows:

Initial guess of γ_l and γ_m

Solve for the design variable z as follows:

$$\begin{aligned} \underset{z}{\text{maximize}} \quad & W(z,\gamma) = B - C - D \\ \text{s.t.} \quad & G(X_c, z, \gamma) = 0 \\ & z^l \leq z \leq z^u \end{aligned}$$

$z \rightarrow$ FORM/SORM/Monte Carlo

- Compute reliability index β

Is $\beta \geq \beta^{target}$?

- if yes, then exit

Make new guess of γ_l and γ_m

Repeat steps $b - f$

In the above, B are the benefits such as the annual energy production of a wind turbine, C are the costs of research, development, manufacturing and installation, and D are the costs of failure and replacement. Stress reserve factors (SRF) can be introduced on the resistance (strength) side of the design equation for G. A wind turbine, unlike civil engineering structures, is active under the influence of a control system. Hence, the design variable z can include control variables in addition to structural/geometric/mechanical properties.

References (Project generated publications in bold)

[1]. IEC 61400-1 (2005) Wind turbines – Part 1: Design requirements. 3rd edition.

[2]. International Electrotechnical Commission. IEC 61400-3 Wind turbines - Part 3: Design

requirements for offshore eind turbines. International Electrotechnical Commission, 2009.

[3]. Kelly M, Larsen G, Dimitrov N, Natarajan A. (2014) Probabilistic Meteorological Characterization for Turbine Loads. Journal of Physics: Conference Series 2014; 524: 012076. doi: 10.1088/1742-6596/524/1/012076

[4]. JW Verkaik, AAM Holtslag (2007), Wind profiles, momentum fluxes and roughness lengths at Cabauw revisited, Boundary-layer meteorology, 122(3), 701-719.

[5]. Dimitrov, N., Natarajan, A., Kelly, M. (2014) Model of wind shear conditional on turbulence and its impact on wind turbine loads, Wind Energy Journal, DOI: 10.1002/we.1797

[6]. Dimitrov, N., Natarajan, A., Mann, J. (2014) Effects of normal and extreme turbulence spectral parameters on wind turbine loads, submitted to Renewable Energy Journal. Nov. 2015

[7]. Dimitrov, N. (2014) Comparative analysis of methods for modelling the short-term probability distribution of extreme wind turbine loads, Wind Energy Journal, Published online 2015

[8]. S. Ott and J. Mann. An experimental test of Corrsin's conjecture and some related ideas, New. Journal of Phys., 7:142, 2005.

[9]. Michael Wilczek, Anton Daitche, and Rudolf Friedrich. On the velocity distribution in homogeneous isotropic turbulence: correlations and deviations from gaussianity, Journal of Fluid Mechanics, 676:191–217, 2011.

[10]. M. Shinozuka and C.-M. Jan. Digital simulation of random processes and its applications. Journal of Sound and Vibration, 25(1):111–128, 1972.

[11]. Masanobu Shinozuka and George Deodatis. Simulation of multi-dimensional Gaussian

stochastic fields by spectral representation. Appl. Mech. Rev., 49(1):29–53, January 1996.

[12]. J. C. Kaimal and J. J. Finnigan. Atmospheric Boundary Layer Flows. Oxford University Press, 304 pp, 1994.

[13]. Paul S. Veers. Three-dimensional wind simulation. Technical Report SAND88–0152, Sandia National Laboratories, 1988.

[14]. Jakob Mann. The spatial structure of neutral atmospheric surface-layer turbulence. J.

Fluid Mech., 273:141–168, 1994.

[15]. G Gulitski, M Kholmyansky, W Kinzelbach, B Luthi, A Tsinober, and S Yorish. Velocity and temperature derivatives in high-Reynolds-number turbulent flows in the atmospheric surface layer. Part 1. Facilities, methods and some general results. Journal of Fluid Mechanics, 589:57–82, 2007.

[16]. Chin-Hoh Moeng. A large-eddy-simulation model for the study of planetary boundary layer turbulence. Journal of the Atmospheric Sciences, 41(13):2052–2062, 1984.

[17]. Chin-Hoh Moeng and Richard Rotunno. Vertical-velocity skewness in the buoyancy driven boundary layer. Journal of the Atmospheric Sciences, 47(9):1149–1162, 1990.

[18]. Kuangmin Gong and Xinzhong Chen. Influence of non-Gaussian wind characteristics on wind turbine extreme response. Engineering Structures, 59:727–744, 2014

[19]. M. Nielsen, G. C. Larsen, J. Mann, S. Ott, Kurt S. Hansen, and Bo Juul Pedersen. Wind simulation for extreme and fatigue loads. Technical Report Risø–R–1437(EN), Risø National Laboratory, 2004.

[20]. M Nielsen, Gunner Chr Larsen, and KS Hansen. Simulation of inhomogeneous, non-stationary and non-gaussian turbulent winds. In Journal of Physics: Conference Series, volume 75, page 012060. IOP Publishing, 2007.

[21]. Tanja Mücke, David Kleinhans, and Joachim Peinke. Atmospheric turbulence and its influence on the alternating loads on wind turbines. Wind Energy, 14(2):301–316, 2011.

[22]. P. P. Sullivan and E. G. Patton. The effect of mesh resolution on convective boundary layer statistics and structures generated by large-eddy simulation. J. Atmos. Sci., 68:2395–2415, 2011.

[23]. Papoulis A.. Probability, Random Variables, and Stochastic Processes. McGraw-Hill Kogakusha, Ltd., 1965.

[24]. Larsen, T.J. and Hansen, A.M. (2007). How to HAWC2, the Users Manual, Risø-R-1597(EN), Risø National Laboratory - Technical University of Denmark.

[25]. Jonkman J, Butterfield S, Musial W, Scott G. Definition of a 5-MW reference wind turbine for offshore system development. *Technical Report NREL/TP-500-38060*, National Renewable Energy Laboratory (NREL), Golden, CO,USA, 2009.

[26]. Larsen, G.C. and Hansen, K.S. (2014). De-trending of wind speed variance based on first-order and second-order statistical moments only. Wind Energy, Vol. 17, No. 12, p. 1905-1924.

[27]. Dimitrov, N.K., "Multivariate Joint Probability Model for Estimating Extreme Load Combinations With Long Return Periods", Submitted to the International conference on Applications of Statistics and Probability in Civil Engineering (ICASP), July 2015.

[28]. Natarajan, A. and Holley, W. E., Statistical Extreme Loads Extrapolation with Quadratic Distortions for Wind Turbines, ASME Journal of Solar Energy Engineering, Vol. 130, 031017, Aug 2008.

[29]. Sørensen, J.D. and H.S. Toft (2014) Safety Factors – IEC 61400-1 ed. 4 - background document. DTU Wind Energy-E-Report-0066(EN).

[30]. EN 1990 (2002) Basis of structural design. *CEN*.

[31]. ISO 19902 (2007) Petroleum and natural gas industries - Fixed steel offshore structures.

[32]. ISO 2394 (2015) General principles on reliability for structures.

[33]. JCSS (2002) Joint Committee on Structural Safety (JCSS). Probabilistic Model Code. http://www.jcss.ethz.ch/.

[34]. Sedlacek, Brozzetti, Hanswille, Lizner & Canisius (1996) Relationship between Eurocode 1 and the "material" oriented Eurocodes. IABSE Colloquium: Basis of Design and Actions on Structures. Delft.

[35]. Jonkman J. M., Buhl M. L., "FAST User's Guide", NREL/EL-500-29798. Golden, Colorado: National Renewable Energy Laboratory, 2005.

[36]. Abdallah I, Natarajan A, Sørensen JD. Impact of uncertainty in airfoil characteristics on wind turbine extreme loads. Renewable Energy. 2015;75, 283-300.

[37]. Moriarty P. J., Holley W. E., and Butterfield S., "Effect of Turbulence Variation on Extreme Loads Prediction for Wind Turbines", Proceedings of the ASME Wind Energy Symposium, AIAA, Reno, NV, 2002, pp. 278–287.

[38]. De las Heras E.G., Gutiérrez R., Azagra1 E. Dalsgaard J., "Assessment of wind turbine for site specific conditions using probabilistic methods", EWEA 2013 conference, 4-7th February 2013, Vienna

[39]. Abdallah, I, Natarajan, A. and Sørensen, J. D., "Influence of the control system on wind turbine reliability in extreme turbulence", Journal of Physics: Conference Series (Online), Vol. 524, No. 1, 012069, 2014.

[40]. Berg J, Natarajan A, Mann J and Patton EG. Gaussian vs non-Gaussian turbulence: impact on wind turbine loads. Wind Energy journal, published online 2016

Acknowledgments

The work presented herein is a part of the Danish Energy Technology Development and Demonstration (EUDP) project titled, “Demonstration of a basis for tall wind turbine design”, Project no 64011 -0352. The financial support is greatly appreciated.

DTU Vindenergi er et institut under Danmarks Tekniske Universitet med en unik integration af forskning, uddannelse, innovation og offentlige/private konsulentopgaver inden for vindenergi. Vores aktiviteter bidrager til nye muligheder og teknologier inden for udnyttelse af vindenergi, både globalt og nationalt. Forskningen har fokus på specifikke tekniske og videnskabelige områder, der er centrale for udvikling, innovation og brug af vindenergi, og som danner grundlaget for højt kvalificerede uddannelser på universitetet.

Vi har mere end 240 ansatte og heraf er ca. 60 ph.d. studerende. Forskningen tager udgangspunkt i ni forskningsprogrammer, der er organiseret i tre hovedgrupper: vindenergisystemer, vindmølleteknologi og grundlag for vindenergi.

Danmarks Tekniske Universitet
DTU Vindenergi
Nils Koppels Allé
Bygning 403
2800 Kgs. Lyngby
Telefon 45 25 25 25

info@vindenergi.dtu.dk
www.vindenergi.dtu.dk